Characterization of the Rifampin ADP-ribosyl transferase Enzyme

Characterization of the Rifampin ADP-ribosyl transferase Enzyme

By

Jennifer D. Baysarowich, B.Sc.

A Thesis

Submitted to the School of Graduate Studies

In partial Fulfilment of the Requirements

For the Degree

Master of Science

McMaster University

MASTER OF SCIENCE (2006) McMaster University

(Biochemistry) Hamilton, Ontario

TITLE: Characterization of the Rifampin ADP-ribosyl transferase Enzyme

AUTHOR: Jennifer D. Baysarowich, B. Sc. (McMaster University)

SUPERVISOR: Professor G.D. Wright

NUMBER OF PAGES: x, 98

Abstract

The ansamycin antibiotics are unique antibacterial agents that inhibit bacterial DNA-dependent RNA polymerase II. Clinical use of this class of antibiotics has primarily been focused on the treatment of tuberculosis using the semi-synthetic rifamycin derivative, rifampin. As drug resistance among different classes of antibiotics continues to rise, there is increased interest in new applications of rifamycins for diseases other than tuberculosis. Clinical resistance to rifampin has largely been the result of point mutations in the target, RpoB, however chromosomal and transposon mediated enzyme-associated resistance is well documented. As rifamycin antibiotic use becomes more widespread, enzymatic resistance will inevitably become more prevalent. Here we describe the characterization of one of the principle enzymes associated with rifampin inactivation, the rifampin ADP-ribosyl transferase enzyme (ARR). Two chromosomally encoded ARR enzymes from *Mycobacterium smegmatis*, and *Streptomyces coelicolor*, and the Tn-encoded ARR-2, widely distributed in Gram negative pathogens, were overexpressed and characterized. These enzymes exhibit comparable, substrate specific steady state kinetic features, and substrate-induced conformational changes that suggest ARR enzymes may demonstrate a preferred order of substrate binding. To gain further insight into the interaction between ARR enzymes and rifampin and NAD^+, the three-dimensional crystal structure of ARR from *M. smegmatis* was solved in complex with rifampin. Based on the three-dimensional structure of ARRm, an S_N1 type reaction has been predicted for rifampin ADP-ribosyl transferase enzymes. This is the first detailed examination of these novel antibiotic-modifying enzymes, relevant to their increased use in the clinic.

Acknowledgements

First and foremost I would like to thank my supervisor Dr. Gerry Wright for giving me the opportunity to be a part of his lab and to work on this project. His support, encouragement, and enthusiasm for science allowed me to learn and grow so much. I have great admiration and respect for him. I would also like to thank Dr. Murray Junop for his help with protein crystallization. I had a great time working with him and learned so much about crystallography.

Thank you also to the members of my committee, Dr. Paul Berti and Dr. Giuseppe Melacini for their help and guidance with this project. I would also like to give special thanks to Raquel Epand for her help with CD spectroscopy and ITC techniques and to Rahul Das for his help with NMR.

Thank you to all Wright lab members both past and present for encouragement, understanding, and for making this experience such a great one. Very special thanks to Kalinka for being such a great friend and for constantly supporting me throughout my career in the lab, and to Laura Rossi for allowing me to elect you as my mentor when I first arrived in the lab.

Finally I would like to thank my family and friends for always being there for me. Their understanding and support helped me achieve success and become the person I am today.

List of Figures

List of Tables

1.0 Introduction

1.1 Antibiotic Resistance

Antibiotic resistance has been recognized as an obstacle in the treatment of infectious disease as early as the 1940's [1]. Over the years, the frequency of resistance in bacteria has risen with the increasing use of antibacterials prompting the emergence of a variety of multidrug resistant (MDR) bacteria [1]. A major problem in the field of infectious disease is that of MDR *Mycobacterium tuberculosis*. Tuberculosis is the leading cause of death by infectious disease in the world, causing two to three million deaths per year, and its re-emergence since the 1980's has been greatly enhanced by co-infection with the human immunodeficiency virus (HIV) [1, 2].

Resistance by target modification is a well documented mechanism of antibiotic resistance, however the transfer of resistance genes among different bacteria via mobile genetic elements, such as bacteriophages, plasmids, and transposons, has no doubt assisted in the rapid increase in drug resistant bacteria [1]. Integrons carrying multiple resistance gene cassettes in tandem are isolated from patients in hospital settings and contribute to the spread of MDR bacteria [3-5]. Resistance genes spread via mobile genetic elements, both in nature and the clinic. These genes often encode enzymes responsible for a variety of resistance mechanisms including enzymatic modification or degradation of the drug, or antibiotic efflux pumps used for transport of the drug out of the cell [3-5]. This growing assortment of naturally occurring resistance determinants forms the antibiotic resistome [6]. As the use of antibiotics in treatment of infectious disease continues it can only be expected that enzyme-mediated resistance will also become more prevalent.

1.2 The Rifamycins

1.2.1 Discovery and General Properties of Rifamycins

Rifamycins belong to the ansamycin class of antibiotics, characterized by the presence of an aromatic naphthalene ring system, bridged by an aliphatic chain (ansa = handle in Latin) [7-9]. Also included in this class of antibiotics are the very closely related tolypomycins, isolated from *Amycolatopsis tolypomycina*, as well as the streptovaricins (Figure 1-1) [8, 9].

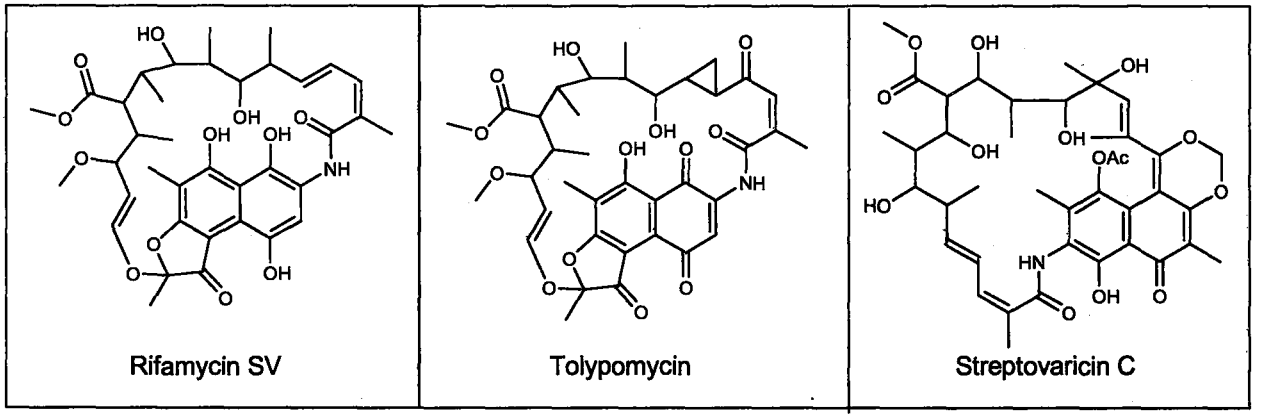

Figure 1-1. Structures of the ansamycin class of antibiotics. Rifmaycins, tolypomycins, and the streptovaricins belong to the ansamycin class of antibiotics, characterized by an ansa chain bridging a naphthalene ring system.

Rifamycins are produced by an Actinomycete, originally classified as *Streptomyces mediterranea*, later reclassified as *Nocardia mediterranea*, and again more recently reclassified as *Amycolatopsis mediterranei* [7, 8]. These antibiotics were first isolated in Lepetit Research Laboratories in Milan in 1959 by Sensi and co-workers as a complex mixture of at least five components; A, B, C, D, and E [7, 8]. Rifamycins are the first class of antibiotics with the unique ability to selectively inhibit bacterial DNA-dependent RNA polymerase (RNAP), making them potent bactericidal agents [2, 7, 9, 10]. They are broad-spectrum antibiotics, active against a variety of Gram-positive bacteria and mycobacteria as well as against some Gram-negative bacteria [9-11]. Rifamycin B was the most stable of the components produced and could easily

be isolated, therefore it was chosen for development as an antibiotic (14). The structure of rifamycin B was solved by Prelog et al. [8, 12] (Figure 1-2). Rifamycin B can be easily converted to rifamycin SV (Figure 1-2) through a series of conversion reactions including oxidation, hydrolysis, and reduction [8]. Rifamycin SV is clinically more potent against infection and therefore a better candidate for drug development; rifamycin SV was the first clinically used rifamycin introduced for treatment of infections with Gram-positive bacteria in the early 1960's [7, 8].

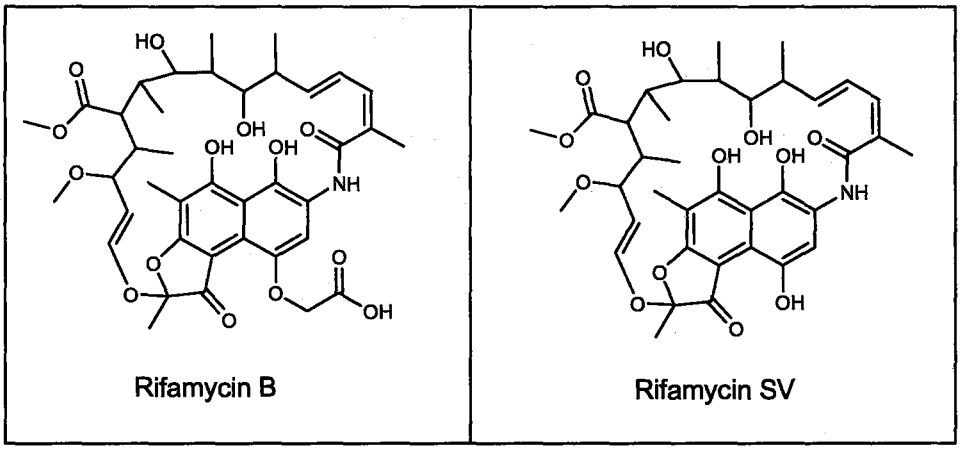

Figure 1-2. Rifamycin B and Rifamycin SV. Rifamycin B, produced by fermentation, has little antibacterial activity. Rifamycin SV, a clinically potent antibacterial, can be accumulated from Rifamycin B by a process of oxidation, hydrolysis, and reduction reactions.

1.2.2 Semisynthetic Rifamycin Derivatives and their Clinical Relevance

From rifamycin SV, semisynthetic derivatives are produced that are used clinically around the world, including rifampin, rifabutin, rifapentine, rifamixin, and more recently benzoxazinorifamycin, rifalazil (also known as KRM-1648) (Figure 1-3) [8, 9, 13]. One of the first semisynthetic rifamycins introduced for clinical use, rifampin, has been used world wide for the treatment of a number of infections caused by *Mycobacteria, Rhodococcus, Nocardia* and *Grodona* [8, 9, 14, 15]. Currently its use is focused solely on treatment of tuberculosis infections. The high frequency with which resistance to rifampin is acquired in *M. tuberculosis*

[11, 16] has led to the exploration of new rifamycins, rifabutin, rifapentine and rifalazil, as candidates for tuberculosis multidrug regimens [13, 17-19]. Although mutations leading to rifampin resistance in *M. tuberculosis* have also been shown to cause rifapentine resistance, rifalazil remains active against isolates with characterized rifampin resistant mutations both in vitro and on intracellular tubercle bacilli [18, 20]. Rifalazil also retains activity against MDR tuberculosis [18].

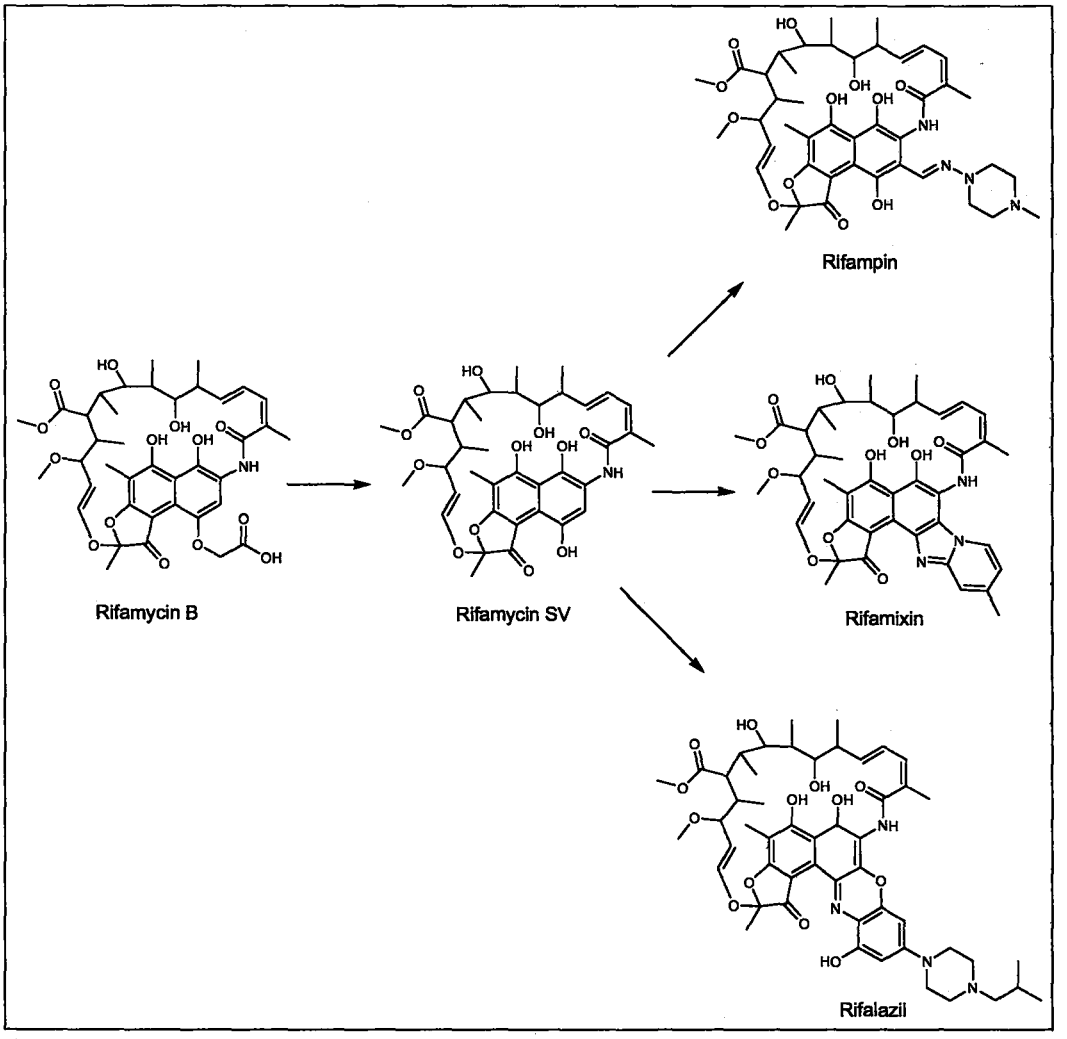

Figure 1-3. Semisynthetic rifamycins of clinical importance. Rifamycin B is converted to Rifamycin SV, the first clinically employed rifamycin, from which a number of clinically more potent antibacterials are synthesized. These semisynthetic rifamycins include rifampin (used in treatment of tuberculosis infections), rifamixin (recently approved for treatment of travelers' diarrhea), and rifalazil (currently in phase II trials for treatment of tuberculosis and candidate therapy for infections with different species of *Chlamydia*).

The increase in drug resistance in other classes of antibiotics is prompting new rifamycin derivatives to become attractive candidates for a number of other infections as well. Rifalazil has been shown to demonstrate potent activity against infections of *Chlamydia pneumoniae* and *Chlamydia trachomatis*, exhibiting low MIC values against rifampin sensitive and resistant strains [7, 13, 21-23], however resistance to rifalazil has already been documented [7, 21]. Activity of rifalazil and novel rifamycin KRM-1657 has also been examined against Gram negative *Helicobacter pylori*, and shown to have MIC values lower than those of rifampin and amoxicillin (Figure 1-4) [24]. Over 700 benzoxazinorifamycins have been screened for activity against rifampin sensitive and resistant isolates of *Staphylococcus aureus* [13, 25]. In vitro and in vivo studies identified a number of novel rifamycins with considerable activity against rifampin resistant *S. aureus*, indicating these compounds could be useful as monotherapeutic agents [13, 25].

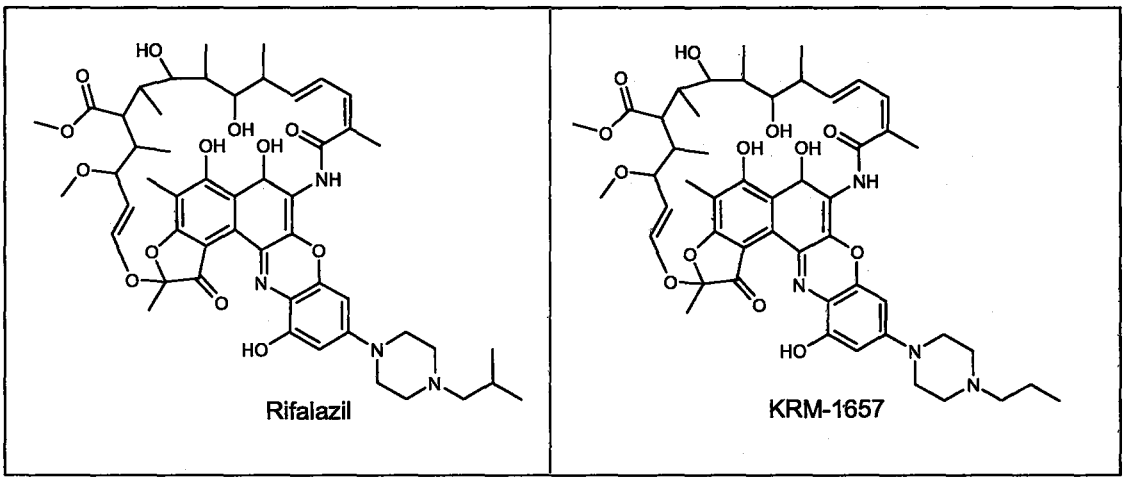

Figure 1-4. Benzorifamycins rifalazil and KRM-1657. Novel rifamycins derivatives screened for activity against Gram negative pathogens.

Another rifamycin derivative, rifamixin, was approved for use in treatment of travelers' diarrhea by the Food and Drug Administration in May 2004 [2, 26]. Use of rifamixin as treatment for hepatic encephalopathy and diverticular diseases of the colon have also been explored [26].

The unique ability of rifamycins to inhibit transcription initiation through tight binding of prokaryotic DNA-dependent RNAP makes this class of antibiotics especially attractive for clinical development [8, 27].

1.3 Rifampin

1.3.1 Rifampin Mechanism of Action

The potent activity of rifampin comes from its unique ability to inhibit transcription initiation through binding of RNAP [8, 27]. Prokaryotic DNA-dependent RNAP is a multisubunit enzyme with a conserved $\alpha_2\beta\beta'$ catalytic core composition [28, 29]. The binding site for rifampin on RNAP is formed primarily by the β subunit [7, 28, 29], although the presence of the β' subunit is required for the formation of a high affinity binding site [29].

The crystal structure of the *Thermus aquaticus* (*Taq*) core RNAP in complex with rifampin was solved in 2001, allowing for a more precise determination of the rifampin binding site [28]. The *Taq* RNAP sequence has 91% identity to the RNAP sequences of *Escherichia coli* and *M. tuberculosis* thus is useful for studying the general binding interactions between rifampin and RNAP in detail [28]. Original mapping of the rifampin binding site was carried out by examination of common rifampin resistant mutations [29]. The rifampin binding site lies in a pocket of the β subunit deep within the main DNA/RNA channel surrounded by sites known for rifampin resistant mutations [28, 30]. In this binding pocket rifampin makes direct contact with 12 residues of the β subunit, through a series of hydrogen bonds and van der Waals interactions that promote the tight binding of rifampin to RNAP [28]. The naphthol ring of rifampin and the methyl group at C7 make van der Waals contacts with a cluster of hydrophobic residues lining one wall of the binding pocket, L391, L413, G414, and I452 (Figure 1-5) [28]. Residue Q390

makes van der Waals contacts with C28 and C29 of rifampin, forming one of the ends of the binding pocket (Figure 1-5); the top of the binding pocket is formed by D396, which makes van der Waals contacts with C18, C21, and C31 of rifampin (Figure 1-5) [28]. Other residues making direct contacts with rifampin include Q393, R406, R409, S411, and E445 as well as the backbone of F394, and are involved in hydrogen bonding interactions (Figure 1-5) [28].

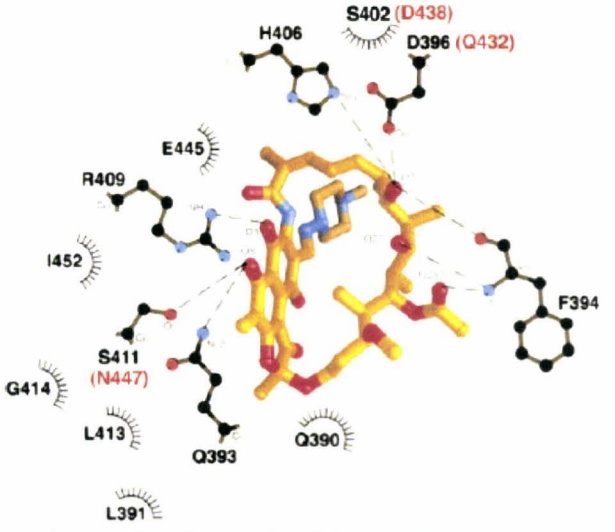

Figure 1-5. Detailed interactions of Rifampin with *Taq*RNAP β subunit. Residues forming Hydrogen bonds are shown in ball-and-stick representation, with hydrogen bonds depicted as dashed lines, residues forming van der Waals are also shown. Carbon atoms of the protein are shown in black, carbon atoms of rifampin are shown in orange. Reprinted from *Cell*, 104. Campbell, E. A., Korzheva, N., Mustaev, A., Murakami, K., Nair, S., Goldfarb, A., and Darst, S. A. Structural mechanism of rifampicin inhibition of bacterial RNA polymerase. 901-912, 2001, with permission from Elsevier.

Binding of rifampin to the RNAP-promoter complex inhibits transcription initiation [27, 28, 31-33]. Two mechanisms of inhibition have been proposed. The mechanism first proposed by McClure and Cech in 1978 describes a simple steric block of the elongating RNA transcript by the presence of rifampin [27]. The binding site for rifampin on RNAP is located only 15 Å from the transcriptional start site of the initiating nucleotide, and only 12 Å from the active site Mg^{2+} of RNAP, suggesting that rifampin may act as a cork in the channel leading the RNA

transcript out of the active site [28, 32]. This mechanism suggests that rifampin-bound RNAP is able to bind the initiating 5' nucleotide and the incoming 3' nucleotide, allowing formation of the first phosphodiester bond [27, 28, 32]. A 2-fold increase in the apparent K_m for the initiating 5' nucleotide is observed for RNAP in the presence of rifampin; no effects are observed for the binding of the incoming 3' nucleotide or formation of the first bond [27]. The binding of rifampin to the β subunit of RNAP inhibits transcription initiation by preventing synthesis of the second or third phosphodiester bond when transcription is initiated by either a nucleoside triphosphate, or a nucleoside di- or monophosphate respectively [27]. The presence of rifampin blocks the path of the elongating RNA transcript at the 5' end once it has become two to three nucleotides long; movement of the 5' nucleotide into the -2 position causes a steric clash with the bound rifampin molecule, and nucleotides further upstream severely clash with rifampin [27, 28, 32]. Rifampin does not interfere with substrate binding or with the catalytic activity or intrinsic translocation of RNAP, but simply blocks the elongation of the RNA chain at the 5' end [27, 28]. Once RNAP has synthesized a long RNA transcript and entered the elongation phase, rifampin has no effect [27].

A second proposed mechanism of transcription inhibition is through allosteric destabilization of the binding of short RNA transcripts to RNAP [31, 33]. The crystal structure of *Thermus thermophilus* RNAP (*tt*RNAP) solved in complex with rifamycin derivatives rifapentine and rifabutin showed significant differences in contacts between rifampin, rifapentine, and rifabutin with RNAP (Figure 1-6) [28, 33]. The tail of rifabutin makes contacts with the σ subunit of RNAP, unlike what is observed for rifapentine or for the *Taq*RNAP-rifampin complex [28, 33]. While rifampin and rifapentine have been shown to block the formation of the second or third phosphdiester bond, rifabutin blocks the formation of the first

bond, even though its tail is located farther from the active site and growing RNA transcript [28, 33]. Data from the *tt*RNAP-rifapentine and rifabutin complexes suggests the steric mechanism alone is insufficient for inhibition, but that binding of rifamycins to RNAP induces an allosteric signal that is transmitted to the active site to disfavor binding of the catalytic Mg^{2+} ion [33]. This is believed to slow the reaction resulting in dissociation of the short RNA/ DNA hybrid [33]. Based on the crystal data two allosteric pathways have been proposed: a σ pathway inhibiting formation of the first phosphodiester bond, and a β pathway inhibiting the second or third phosphodiester bond formation [33]. Detailed studies on the interaction of rifalazil and RNAP have yet to be examined.

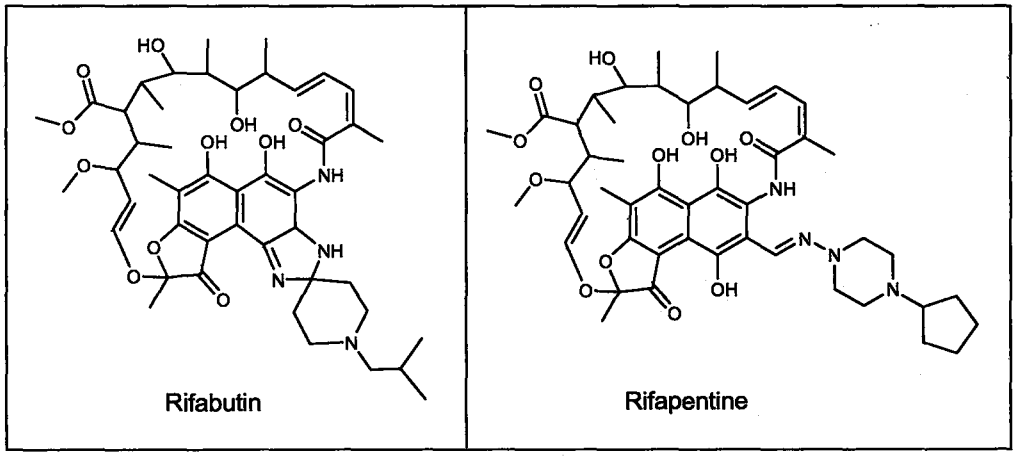

Figure 1-6. Semisynthetic rifamycin derivatives. The structure of *Thermus thermophilus* RNAP was solved in complex with rifabutin and rifapentine to study the mechanism of action of rifamycins.

Modifications to the rifampin binding site on the β subunit or to the antibiotic itself that prevent binding to RNAP will therefore confer resistance to the drug.

1.3.2 Mechanisms of Rifampin Resistance

The frequency of rifampin resistance in naturally occurring cells is approximately 10^{-6} to 10^{-9} [11, 16]. *Mycobacterium smegmatis* is naturally resistant to rifampin but has none of the common mutations conferring rifampin resistance in otherwise sensitive *M. tuberculosis* and *Mycobacterium leprae*, despite the highly conserved sequence in mutation prone regions of the *rpoB* gene [34]. This suggests an alternate mechanism of resistance must exist for *M. smegmatis*. Examination of inactivated products of rifampin from a collection of organisms has identified a variety of mechanisms in which rifampin is covalently modified preventing binding to its target RNAP [28, 35-41]. These rifampin resistant determinants collectively make up a naturally occurring rifampin resistome.

1.3.2.1 Point Mutations in RNA Polymerase

The primary mechanism of rifampin resistance in clinical isolates of *M. tuberculosis* and *M. leprae* is through missense mutations in the *rpoB* gene, causing decreased binding of rifampin to RNAP [3, 14, 42]. This type of resistance often results from point mutations leading to the substitution of a small amino acid, with larger, bulkier residues, or addition or removal of a proline residue [28]. These substitutions occur in the area around the rifampin binding pocket and likely affect the local folding of the protein thus preventing the binding of rifampin [28]. Regions of the *rpoB* gene with a tendency for mutations conferring rifampin resistance show high levels of sequence conservation among prokaryotes, a likely explanation for their broad spectrum activity [28]. Mapping of the *E. coli rpoB* identified four small regions existing in the N-terminal half of the protein where 95% of resistance mutations are found [7]. Mutations within these regions of the *rpoB* gene generally occur in three distinct clusters that are typically

numbered according to the *E. coli* sequence: rif cluster I, amino acids 505 to 532, rif cluster II, amino acids 560 to 572, and rif cluster III, a single mutation at amino acid 687; as well as an N-terminal region consisting of amino acids 143-148; [7, 11, 14, 42]. Rif cluster I is located in the active center of RNAP at the site of rifampin binding [28, 43]. In *E. coli*, the majority of the mutations map to rif cluster I and II, while in other species mutations conferring rifampin resistance map primarily to rif cluster I [7, 11, 14]. Between *E. coli* and *M. tuberculosis* there are 23 positions at which single amino acids mutations may occur resulting in rifampin resistance, 17 of these residues are found in rif cluster I and of these, 10 residues are close enough to make direct contacts with rifampin [28]. Figure 1-7 illustrates common mutations found in the rif cluster I region of *E. coli, M. tuberculosis*, and *M. leprae*. The wide variety of *rpoB* mutations leads to different levels of resistance, as well as to different levels of RNAP activity showing a range of impaired growth patterns [44].

E. coli	505- FFGSSQLSQFMDQNNPLSE I THKRRI SALGPGG-537
M. tuberculosis	424- FFGTSQLSQFMDQNNPLSGLTHKRRLSALGPGG-456
M. leprae	399-FFGTSQLSQFMDQNNPLSGLTHKRRLSALGPGG-431

Figure 1-7. Alignment of rif cluster I from *E. coli, M. tuberculosis*, and *M. leprae*. Residues where point mutations occur are shown in red; residues that are substituted with high frequency in clinical strains of *M. tuberculosis* are shown in blue. D435 is substituted at a frequency of 9 %, H445 is substituted at a frequency of 36 %, and S450 is substituted at a frequency of 41 % [14, 28].

1.3.2.2 Phosphorylation and Glycosylation

Although the majority of rifampin resistance in clinical isolates of *M. tuberculosis* results from mutations in the *rpoB* gene, resistance via enzyme-mediated inactivation of rifampin has been documented in a number of other bacteria [27, 35, 39-41, 45]. These enzymes covalently modify the antibiotic preventing target binding [46]. Enzymatic inactivation of rifampin is species specific, and has been observed in species of *Nocardia, Mycobacteria, Bacillus, Rhodococcus, Gordona,* and *Tsukamurella.* These mechanisms of inactivation include *O*-phosphorylation, *O*-ribosylation, and *O*-glycosylation [28, 35-41]. Covalent modifications of rifampin occur at either the 21- or 23-OH position of the ansa chain (Figure 1-8). These free hydroxyl groups are necessary for the antibacterial activity of rifampin [41].

Phosphorylation of antibiotics occurs by antibiotic kinases, enzymes that catalyze the transfer of a phosphate from ATP to a substrate- the target antibiotic [46]. Inactivation of rifampin by phosphorylation was first reported in *Nocardia otitidiscaviarum* at the 21-OH position (Figure 1-8) [41]. Inactivation products, RIP-3 and RIP-4, from nineteen strains were monitored by thin-layer chromatography and analyzed by ^{1}H and ^{13}C NMR [41]. NMR spectra were used to determine the structures of the inactivated products to be 21-(*O*-phosphoryl)rifampin and 3-formyl-21-(*O*-phosphoryl)-rifamycin SV respectively [37, 41]. Inactivation of rifampin by phosphorylation is also observed in a number of species of *Bacillus* and *Rhodococcus rhodochrous* [36, 39]. Rifampin phosphotransferase enzymes have yet to be characterized.

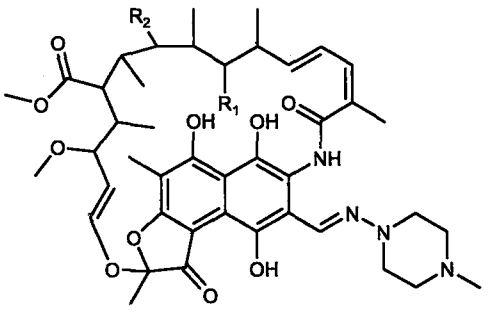

21-(*O*-phosphoryl)rifampin R_1=OPO_3H_2

23-[*O*-(β-D-glucopyranosyl)]rifampin R_2=β-D-glucose

Figure 1-8. Structure of phosphorylated and glycosylated rifampin. Phosphorylation and glycosylation of rifampin occur at the 21-OH (R_1) and 23-OH (R_2) positions of the ansa bridge respectively. Modifications to these positions, which make necessary contacts with the β subunit of RNAP, prevent binding of rifampin to its target thereby conferring resistance to rifampin.

Glycosylation, a less common method of enzymatic inactivation [46], was first reported in the species *Nocardia brasiliensis*, at the 23-OH position of rifampin (Figure 1-8) producing inactivated products RIP-1 and RIP-2 [37, 40]. Structures of glycosylated compounds were confirmed by NMR to be 3-formyl-23-(*O*-[β-D-glucopyranosyl])rifamycin SV and 23-(*O*-[β-D-glucopyranosyl])rifampin respectively [37, 40]. RIP-1 and RIP-2 were isolated and antimicrobial activity against other susceptible Gram-positive bacteria was determined to be >50 μg/ml, indicating that rifampin had been inactivated by glycosylation of the 23-OH position [41]. Rifampin glycosyltransferase enzymes have also yet to be characterized.

Comparison of RIP-1, RIP-2, RIP-3, and RIP-4 by thin-layer chromatography using chloroform and methanol as the developing solvent showed Rf values for RIP-1 and RIP-2 of 0.70 and 0.55 respectively; Rf values for RIP-3 and RIP-4 were 0.12 and 0.31 respectively [41]. MIC values for inactivated rifampin against *S. aureus*, *Mycobacterium luteus*, and *Bacillus subtilis* increased from ≤ 0.2 μg/mL to > 100 μg/mL [40, 41] confirming inactivation. Modification to the 21- or 23-OH position of rifampin results in the inactivation of the drug, substantiating the importance of these positions for rifampin activity.

1.3.2.3 Rifampin Decomposition

Inactivation associated with the decolorization of rifampin is considered to be the result of decomposition of the antibiotic. Although this method of inactivation is observed in a number of species including *Rhodococcus, Nocardia*, and *Bacillus*, the final product of inactivation has not yet been examined [35, 36, 39, 41, 45]. While several attempts have been made to isolate and purify a decomposition end product, success has not been achieved [36, 39, 41]. This could be the result of a lack of appropriate detection methods for the decolorized compound, or the possibility that the inactivated compound has been broken down into compounds that are too complex to be isolated by standard extraction methods [39]. The gene believed to be responsible for inactivation of rifampin by decomposition, *iri*, was isolated using DNA from *Rhodococcus equi*, known to inactivate rifampin by decomposition [35]. The *iri* gene encodes a protein of 479 amino acids, which when expressed in *E. coli*, confers resistance to rifampin with MIC values >50 μg/ml [35]. BLAST searches using DNA and amino acid sequences found similarity with known monooxygenases [35]. Oxidation of antibiotics is not a widespread mechanism of inactivation, but has been observed in pathogenic bacteria [46]. One well characterized example of this is the oxidation of tetracycline antibiotics by the enzyme TetX, an oxygen-requiring flavoprotein, that causes the antibiotic to subsequently undergo a non-enzymatic rearrangement into unstable products turning, media black [46]. The similarity between the possible *R. equi* rifampin monooxygenase and monooxygenases known to act on phenolic compounds, suggests the naphthalenyl moiety of rifampin as a possible and likely target for this class of enzyme [35].

1.3.2.4 ADP-Ribosylation

Inactivation of rifampin by ribosylation was first identified in 1995 in fast growing strains of *Mycobacteria* [45]. Mass spectrometry and chromatographic mobility of inactivated products, RIP-Ma and RIP-Mb, was distinctive from that observed for products of glycosylated or phosphorylated rifampin by pathogenic species of *Nocardia* [37, 40, 45]. MIC values of ribosylated rifampin against *M. smegmatis* and *B. subtilis* were > 100 μg/mL; MICs of rifampin were 25.0 and 0.02 μg/mL respectively [45]. Mass spectrometry and ^{1}H NMR were used to determine the structures of RIP-Ma and RIP-Mb to be 3-formyl-23-[*O*-(α-D-ribofuranosyl)]rifamycin SV, and 23-[*O*-(α-D-ribofuranosyl)]rifampin respectively [45]. Although it has been observed mainly in fast growing *Mycobacteria*, such as *M. smegmatis*, ribosylation of rifampin has also been documented some species of *Rhodococcus, Gordona,* and *Tsukamurella* [38, 39, 45].

The gene responsible for the inactivation of rifampin by ribosylation, *arr,* was identified by subcloning experiments with chromosomal DNA from *M. smegmatis* DSM 43756 [15]. Disruption of the gene abolished inactivation activity thus confirming its responsibility for inactivation of rifampin by ribosylation [15]. A similar gene, *arr-2*, has been identified on a gene cassette in a class I integrons widely distributed in multidrug resistant Gram negative bacteria [3-5]. Also found on these integrons are gene cassettes carrying resistance to expanded-spectrum cephalosporins, gentamicin, aminoglycosides, β-lactams, chloramphenicol, tetracyclines, and quinolone compounds [3-5].

Overexpression of the *M. smegmatis arr* gene under control of the *lac* promoter in *E. coli* led to the detection of a novel derivative, RIP-TA [38]. ^{1}H and ^{13}C NMR were used to determine the structure of RIP-TA to be 23-(*O*-ADP-ribosyl)rifampin, an intermediate in the pathway

leading to ribosylated rifampin [38]. Discovery of the RIP-TA intermediate suggested the *arr* and *arr-2* genes encode mono ADP-ribosyl transferase enzymes that are responsible for catalyzing the transfer of the ADP-ribose moiety of NAD^+ to the 23-OH position of rifampin and rendering the drug inactive (Figure 1-9) [37]. Inactivation of rifampin by ribosylation is the first report of ribosylation as a mechanism of antibiotic inactivation [45].

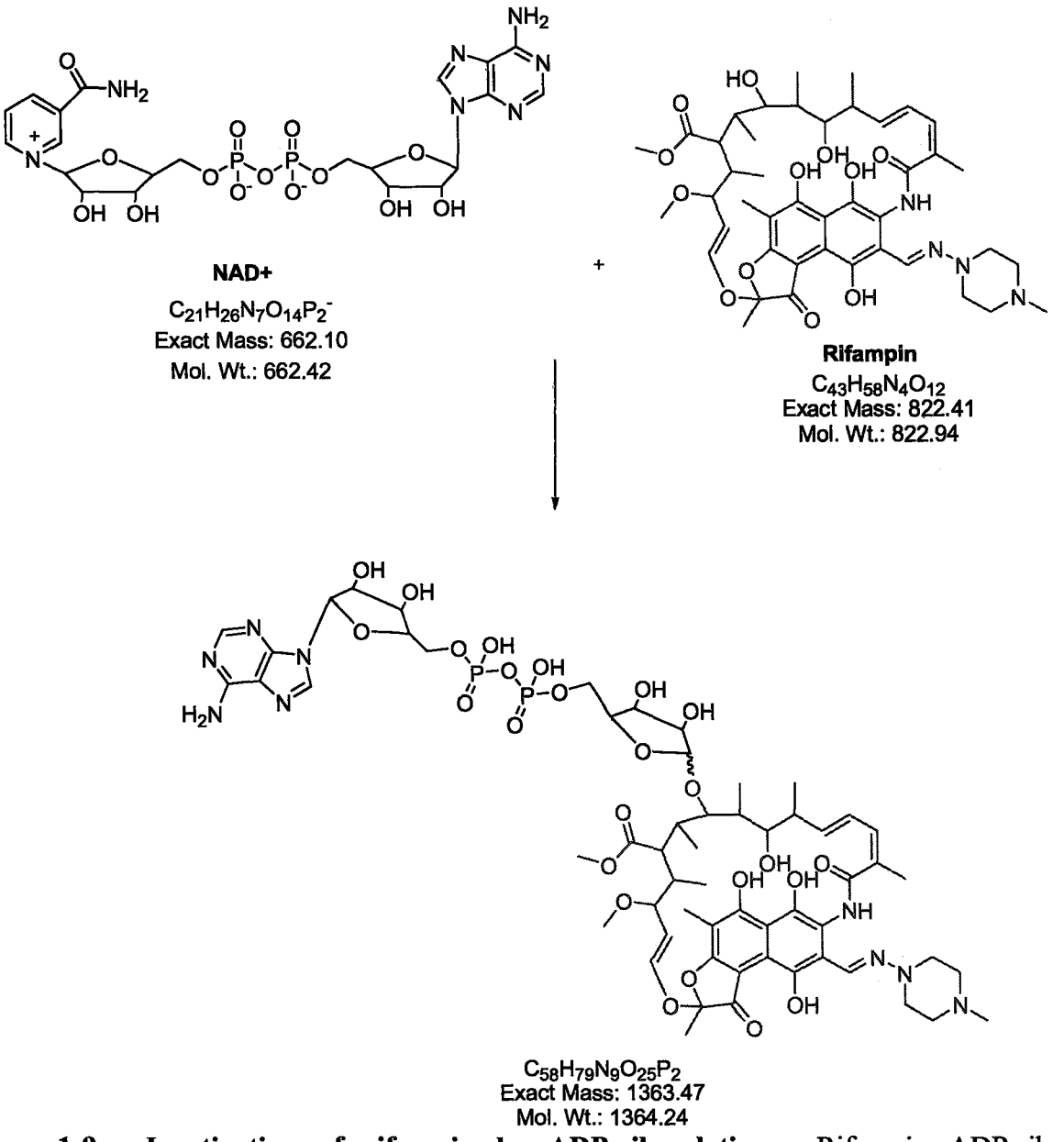

Figure 1-9. Inactivation of rifampin by ADP-ribosylation. Rifampin ADP-ribosyl transferases catalyze the transfer of the ADP-ribose moiety of NAD^+ to the 23-OH position of the ansa bridge of rifampin. Modification to this position of rifampin produces an inactivated product unable to bind its target RNAP thereby conferring resistance to rifampin.

1.4 ADP-Ribosyl Transferases

ADP-ribosylation is commonly considered a mode of metabolic regulation, or post-translational protein modification [47]. Mono(ADP-ribosyl) transferases catalyze the transfer of the ADP-ribose moiety from NAD^+ to specific amino acids on acceptor proteins, while poly(ADP-ribose) polymerases (PARPs) catalyze the transfer of branched polymers of ADP-ribose to protein acceptors [48, 49]. The recent discovery of the ADP-ribosylation of rifampin has introduced a novel class of mono ADP-ribosyl transferase enzymes with a unique small molecule acceptor.

1.4.1 Mono ADP-ribosyl Transferases and Poly(ADP)ribosyl Transferases

Mono(ADP-ribosyl) transferases are well known not only for their endogenous role in protein post-translational modifications, but also for their activity as secreted bacterial exotoxins, such as exotoxin A, diphtheria, cholera, pertussis and clostridial toxins [47, 48, 50, 51]. Bacterial ADP-ribosylating exotoxins act by catalyzing the transfer of ADP-ribose from NAD^+ to essential eukaryotic cell proteins at His (or diphthamide), Arg, or Cys residues [48]. These enzymes can be classified into five groups based on protein target: EF-2, heterotrimeric GTP-binding proteins, small molecular weight GTP-binding proteins, actin, and unidentified eukaryotic target proteins [51]. These toxins use an A:B structure function organization in which the B domain allows passage of the A domain across the cell membrane and into the cell where it can exert its ADP-ribosyl transferase activity to inhibit host cell functions [47, 51]. Bacterial ADP-ribosylating exotoxins share a structurally conserved active site, although primary sequences show little overall similarity [51].

Mono ADP-ribosyl transferases are also found in eukaryotic cells and are involved in processes such as the immune response, various signal cascades, and regulation of the cell cytoskeleton [48]

PARPs are members of a large family of enzymes that catalyze the transfer of branched polymers of ADP-ribose to specific amino acid residues on acceptor proteins, using NAD^+ as the donor of ADP-ribose [46, 48]. Presently 18 PARPs are known that share a conserved 40 kDa catalytic domain first identified by studying structure-function relationships in PARP-1 [49, 52]. PARPs are known to play a role in the control of cell cycle progression during cell division and have been found to associate with centrosomes, telomeres, centromeres, and microtubules [49]. Poly(ADP-ribosyl)ation is also an immediate response to DNA damage, responsible for the modification of histones and nuclear proteins to repair the damage [49].

Bacterial mono-ADP-ribosyl transferases and PARPs share structurally similar active site folds, however little sequence homology exists between these classes of ADP-ribosyl transferase enzymes [49].

1.4.2 Rifampin ADP-ribosyl Transferases

The rifampin ADP-ribosyl transferase enzymes (ARR) are a unique class of ADP-ribosyl transferases [38]. Unlike well known mono-ADP-ribosyl transferases and PARPs, ARR enzymes are less than 17 kDa in size, and act by catalyzing the transfer of the ADP-ribose from NAD^+ to the small molecule rifampin, rather than a protein target [38]. Chromosomal copies of the rifampin ADP-ribosyl transferase gene have been identified in *M. smegmatis* and *Streptomyces coelicolor*, as well as a Tn-encoded copy widespread in Gram negative pathogens [15].

Sequence comparisons of the two chromosomally encoded copies of ARR, and the Tn-encoded ARR-2, isolated from *Pseudomonas aeruginosa* show approximately 55% identity to each other; 3% gaps (Figure 1-10). Further understanding of the mechanism of action of the rifampin ADP-ribosyl transferase enzyme is necessary as rifamycin antibiotic use expands and enzymatic resistance becomes more prevalent.

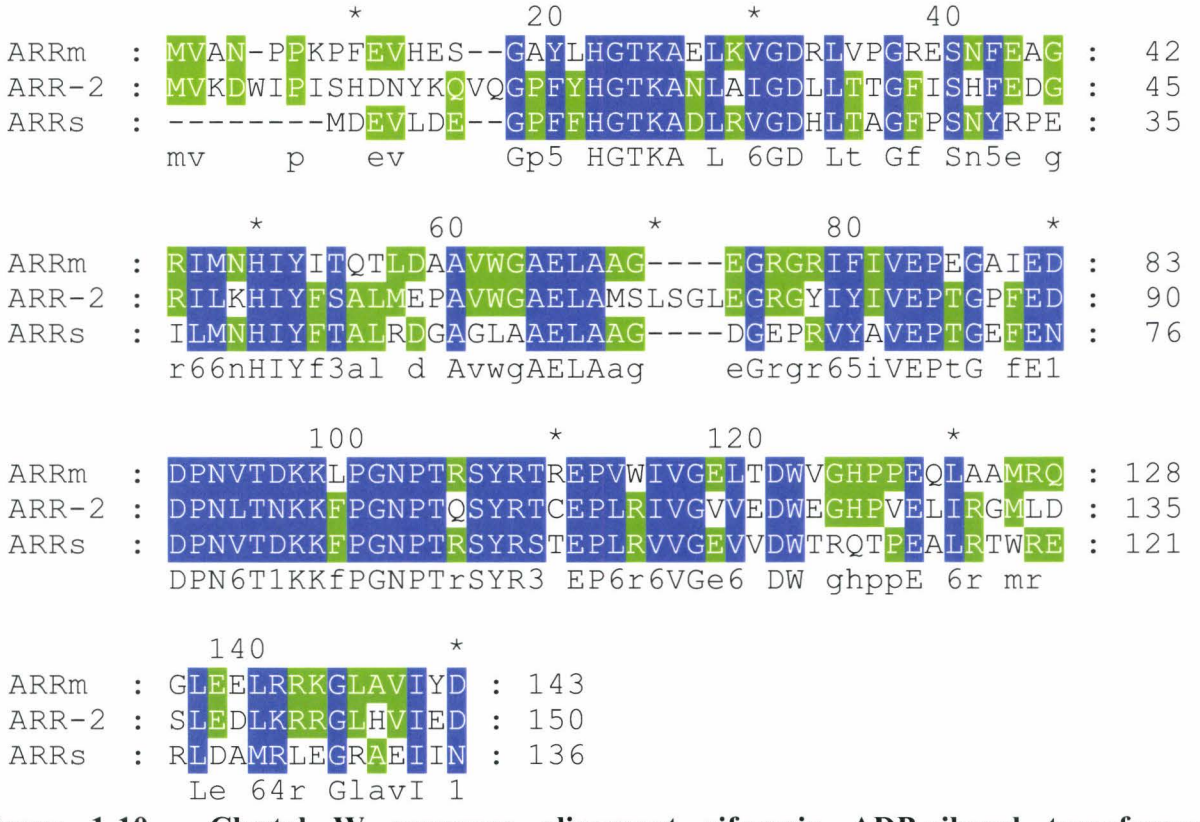

Figure 1-10. Clustal W sequence alignment rifampin ADP-ribosyl transferases. Chromosomally encoded ARR enzymes from *M. smegmatis* and *S. coelicolor*, and Tn-encoded ARR-2 show approximately 55 % identity with one another, 3 % gaps. Blue blocks represent sequence with 100 % similarity; green blocks represent sequence with 67 % similarity.

1.5 Research Objectives

As drug resistance among different classes of antibiotics continues to rise, interest in rifamycins for applications other than treatment of tuberculosis has increased as well, leading to synthesis of novel rifamycin derivatives with potential for use in the clinic. As rifamycin antibiotic use becomes more widespread enzyme-mediated rifampin resistance will also become more prevalent. The goal of this study has been to characterize one of the key enzymes associated with rifampin inactivation, the rifampin ADP-ribosyl transferase enzyme (ARR). Two chromosomally encoded ARR enzymes from *M. smegmatis* and *S. coelicolor*, and the Tn-encoded ARR-2, isolated from *P. aeruginosa* were overexpressed, purified, and assayed for determination and comparison of steady-state kinetic parameters K_m, k_{cat}, and k_{cat}/K_m. Interactions between ARR enzymes and substrates NAD^+ and rifampin were studied through examination of substrate-induced conformational changes and ligand binding experiments. Completion of the three-dimensional crystal structure of the *M. smegmatis* ARR enzyme in complex with rifampin provided further insight into the interaction between ARR enzymes and rifampin and NAD^+. Comparison of ARR with other classes of ADP-ribosyl transferases allows for the prediction of a reaction mechanism by which these unique antibiotic inactivating enzymes may function. This study provides valuable information that can be used for the development of a method to circumvent this type of resistance.

2.0 Chapter 2 – Steady-state Kinetic Parameters and Ligand-Induced Conformational Changes in ARR

2.1 Introduction

To examine the NAD^+-dependent inactivation of rifampin by the rifampin ADP-ribosyl transferase enzyme, two chromosomally encoded ARR enzymes, ARRm from *M. smegmatis* and ARRs from *S. coelicolor*, and the Tn-encoded ARR-2, were overexpressed, and purified. The enzymatic efficiency of each of the ARR enzymes was assessed and compared. Steady-state kinetic parameters, K_m, k_{cat}, and k_{cat}/K_m were determined and shown to be comparable among each of the ARR enzymes.

To gain further understanding of the mechanism of rifampin inactivation by rifampin ADP-ribosyl transferase enzymes, the interactions between ARR enzymes and substrates NAD^+ and rifampin were examined. Through a series of ligand binding studies it was shown that the ARR enzymes exhibit substrate-induced conformational changes in the presence of rifampin and/or NAD^+.

This chapter describes the determination and comparison of the catalytic efficiency of rifampin ADP-ribosyl transferase enzymes from disparate sources, and the interactions with rifampin and NAD^+ that make the ARR enzyme a unique antibiotic inactivating enzyme.

2.2 Materials and Methods

2.2.1 General Methods

Rifampin and nicotinamide adenine dinucleotide (NAD^+) were purchased from Sigma-Aldrich Chemical Co. (St. Louis, MO). Bacterial cultures were grown overnight in Luria Broth (LB) from Sigma (St. Louis, MO) at 37°C and 250 rpm, supplemented with 100 μg/mL ampicillin or 50 μg/mL kanamycin purchased from BioShop Canada, Ltd. (Burlington, ON) for plasmid selection. *E. coli* BL21(DE3) cells were used for protein overexpression. DNA analysis was done using 1% Tris-acetate-ethylenediamine-tetracetic acid (TAE) agarose gel electrophoresis stained with Sybr Safe DNA gel stain from Invitrogen (Burlington, ON).

2.2.2 Gene Amplification and Plasmid Construction

The *arr* genes from *M. smegmatis* and *S. coelicolor* were cloned into pET15b (+) and pET22b (+) expression vectors (Novagen, San Diego, CA) by previous lab members Matthew Crouch and David Boehr respectively. The nucleotide sequences for *arr* from *M. smegmatis and S. coelicolor* found in GenBank are 429 bp and 351 bp in length respectively (*M. smegmatis arr* accession no. AF001493; *S. coelicolor arr* accession no. SCO2860)

The *arr-2* gene sequence is 453 bp long and can be found in GenBank (accession no. AF078527). The *arr-2* gene was isolated from the plasmid pCTF1, a generous gift of Dr. D. Rowe-Magnus. Plasmid DNA was extracted from *E. coli* XL1 Blue cells using Qiagen QIAprep Spin Miniprep Kit (Qiagen Inc., Mississauga, ON) following the protocol outlined by the manufacturer. Plasmid DNA was used as a template for the amplification of the *arr-2* gene by Polymerase Chain Reaction (PCR). Reactions were prepared using 1 x Biotools DNA polymerase buffer containing 75 mM Tris HCl pH 9.0, 2.0 mM $MgCl_2$, 50 mM KCl, and 20 mM

$(NH_4)_2SO_4$ (Biotools Inc., Edmonton, AB) mixed with a 20 x dilution of purified plasmid template DNA, and primers at a final concentration of 1.6 μM, synthesized at the MOBIX Central facility at McMaster University (Hamilton, ON). Reactions were incubated for 1 minute at 94°C prior to the addition of 1 unit Biotools DNA polymerase. The PCR program used for amplification of the *arr-2* gene was designed to contain a gradient to test two different annealing temperatures based on the melting temperatures of the primers (Table 2-1). This program consisted of 30 cycles of the following: 94°C for 1 minute, annealing at 37.6°C or 44.1°C for 1 minute, and 72°C for 30 seconds to allow for elongation of the DNA. At the end of 30 cycles the reactions were held at 72°C for 7 minutes.

Table 2-1. Primers used for amplification of the *arr-2* gene.

	Primer (5'→3')	**Melting Temperature (°C)**
Forward	GGAATTCATATGGTAAAAGATTGGATTC	39
Reverse	CGAATTCAAGCTTCTAGTCTTCAATGACGTGTAAACC	49

Restriction sites for *Nde*I and *Hind*III are underlined in the forward and reverse primers respectively.

Following amplification, the *arr-2* gene was inserted into the Zero Blunt TOPO® vector (Invitrogen, Burlington, ON) for subcloning into the pET system. The Klenow reaction (Fermentas, Burlington, ON) was used to fill in 3' overhangs on the PCR products, making the ends blunt for insertion into the TOPO vector. The plasmid construct was then digested with restriction enzymes *Nde* I and *Hind* III at 37°C for 3 hours to excise the gene from the vector. Digestion was followed by an overnight ligation at room temperature with *Nde* I and *Hind* III digested pET28a (+) expression vector (Novagen, San Diego, CA). The construct was used to transform *E. coli* BL21 (DE3) cells.

2.2.3 Overexpression and Purification

E. coli BL21 (DE3) cells carrying expression vectors for each of the *arr* genes share the same general growth conditions. Single colonies of *E. coli* BL21 (DE3) cells carrying the plasmid with the gene of interest were inoculated into 25 mL of LB supplemented with antibiotic for selection (Table 2-2), and incubated overnight at 37°C at 250 rpm. From these cultures, 10 mL aliquots were used to inoculate 1L of LB plus antibiotic, which were incubated at 37°C and 250 rpm. Cultures were grown to an OD_{600nm} of ~ 0.6 where they were induced by addition of isopropyl β-D-thiogalactopyranoside (IPTG) to a final concentration of 1 mM. For overexpression of *S. coelicolor* ARR and ARR-2, cultures were induced at 16°C for 20 hours; for overexpression of *M. smegmatis* ARR, cultures were induced at 25°C for 5 hours.

Table 2-2. Summary of plasmids, bacterial strains and antibiotics used for overexpression of ARRs, ARRm, and ARR-2 proteins.

Protein	**ARRs**	**ARRm**	**ARR-2**
Plasmid	pET15b (+)	pET22b (+)	pET28a (+)
Bacterial Strain	*E. coli* BL21 (DE3)	*E. coli* BL21 (DE3)	*E. coli* BL21 (DE3)
Antibiotic Resistance Gene	Ampicillin	Ampicillin	Kanamycin

Cells were harvested by centrifugation at 6, 000 rpm for 10 min. Cells were then resuspended in 20 mL lysis buffer consisting of 50 mM HEPES pH 7.5, 1 mM ethylenediaminetetraacetic acid (EDTA), and 1 mM phenylmethyl sulfonyl fluoride (PMSF), and passed three times through a French Press at 20, 000 psi to lyse the cells. Following cell lysis, centrifugation at 15, 000 rpm for 20 min was used to remove cell debris.

Fractions containing protein were analyzed using 15% sodium dodecyl sulfate polyacrylamide gel electrophoresis (SDS-PAGE). Electrophoresis was carried out at a constant voltage of 200 V. Gels were stained with Coomassie blue for protein visualization.

2.2.3.1 Purification of M. smegmatis ARR

The purification of the ARRm enzyme was carried out in two steps. Cell lysate was applied directly to a 20 mL HiPrep Q Sepharose Column (Pharmacia, Piscataway, NJ) at a flow rate of 1.0 mL/min. The protein eluted at approximately 10 % buffer B using a linear gradient (Buffer conditions are described in Table 2-3). Fractions containing the ARRm protein, as shown by analysis using 15% SDS-PAGE, were pooled and concentrated to approximately 20 mL using 10, 000 MWCO Amicon ultra-15 centrifugation filters from Millipore (Etobioke, ON). The second step of the purification was done using a 1 mL HR 5/5 Phenyl Superose Hydrophobic Interaction Column (Pharmacia, Piscataway, NJ). The pooled sample was equilibrated with 1.25 M ammonium sulfate and applied to the column, pre-equilibrated with 1.25 M ammonium sulfate, at a flow rate of 0.5 mL/min. The protein was eluted at approximately 50% buffer B using a linear gradient (Buffer conditions are described in Table 2-3). Following analysis using 15% SDS-PAGE, fractions containing ARRm were pooled and dialyzed overnight in 50 mM HEPES pH 7.5 at 4°C and stored at -20°C in 40% glycerol. For the crystallization of the ARRm protein a HiPrep 26/10 Desalting column (Pharmacia, Piscataway, NJ) was used to equilibrate ARRm in 20 mM HEPES pH 7.5 instead of using dialysis.

2.2.3.2 Purification of S. coelicolor ARR and ARR-2

Following lysis and centrifugation, supernatants were applied directly onto a 5 mL Hi Trap Chelating HP Column (Amersham Biosciences, Piscataway, NJ) at a flow rate of 1.0 mL/min. Both the ARRs and ARR-2 proteins were eluted at a concentration of approximately 15% buffer B using a linear gradient (Buffer conditions are described in Table 2-3). Fractions containing ARRs or ARR-2 protein as established by 15% SDS-PAGE were pooled and dialyzed

overnight into 50 mM HEPES pH 7.5 at 4°C. The ARRs and ARR-2 proteins were stored at -20°C in 40% and 20% glycerol respectively.

Table 2-3. Summary of columns and buffer conditions used for purification of ARRm, ARRs, and ARR-2 proteins.

Protein	Column	Buffer A	Buffer B
ARRm	20 mL HiPrep Q Sepharose	50 mM HEPES pH 7.5 1 mM EDTA	50 mM HEPES pH 7.5 1 mM EDTA 1 M NaCl
ARRm	1 mL Phenyl Superose	50 mM Sodium Phosphate pH 7.0 1.25 M ammonium sulfate	50 mM Sodium Phosphate pH 7.0
ARRs	5 mL Hi Trap Chelating HP	50 mM HEPES pH 7.5 20 mM Imidazole	50 mM HEPES pH 7.5 250 mM Imidazole
ARR-2	5 mL Hi Trap Chelating HP	50 mM HEPES pH 7.5 20 mM Imidazole	50 mM HEPES pH 7.5 250 mM Imidazole

2.2.4 Steady-State Kinetic Assays by High Performance Liquid Chromatography

Liquid Chromatography/Mass Spectrometry (LC/MS) using Applied Biosystems QTRAP LC/MS/MS (Boston, MA) was used to confirm the presence of ADP-ribosyl rifampin as a product of the reaction of each of the ARR enzymes prior to assay development. Samples were characterized using the following method: 0-1 min 5% solvent B; 1-11 min, linear gradient up to 97% solvent B; 11-12.5 min, 5% solvent B; 12.5-14.5 min, 5% solvent B; 0.05% formic acid (v/v) (Solvent A), acetonitrile/0.05% formic acid (v/v) (Solvent B). The activity of rifampin ADP-ribosyl transferase enzymes ARRm, ARRs, and ARR-2 was analyzed with a discontinuous reverse phase high performance liquid chromatography (HPLC) assay using a DIONEX C18 column equilibrated in 0.05% Trifluoroacetic acid (TFA) (v/v) (Solvent A). Products were eluted using a linear gradient in acetonitrile/0.05% TFA (v/v) (Solvent B) at a flow rate of 1.0 mL/min.

2.2.4.1 Initial Velocity Studies

Progress curves were generated for each of the ARR enzymes at three different substrate concentrations and used to determine the initial rate range of the reaction. Reactions were prepared in 100 µL of 50 mM HEPES pH 7.5, 1 nmole ARR, and 0.1 mM, 0.5 mM, or 1.0 mM of NAD^+ or rifampin. Reaction mixes were incubated 0, 2, 5, 10, 15, 30, and 45 min, and stopped by the addition of methanol to 50% (v/v). Product formation was analyzed by reverse phase HPLC according to the following method: 0-1 min, 5% solvent B; 1-11 min, linear gradient up to 97% solvent B; 11-12.5 min, 5% solvent B; 12.5-14.5 min, 5% solvent B (Solvent A: 0.05% TFA (v/v); Solvent B: acetonitrile/0.05% TFA (v/v)). The area under the curve (AUC) of the product as shown on the HPLC chromatogram was then plotted against time and the linear part of the curve was used to determine the initial rate range of the reaction at each substrate concentration to be 5 minutes.

2.2.4.2 Assay Development and kinetics

Steady state kinetic parameters for rifampin and NAD^+ were determined for the ARRm and ARR-2 enzymes by varying substrate at six concentrations from 0.05 – 2.0 mM, and for the ARRs enzyme by varying substrate at five concentrations from 0.05 – 1.0 mM. Reactions were prepared in 100 µL of 50 mM HEPES pH 7.5, 1 nmole ARR, 0.5 mM NAD^+, and varied rifampin concentrations to determine steady state kinetics for rifampin, as well as in 100 µL of 50 mM HEPES pH 7.5, 1 nmole protein, 0.5 mM rifampin, and varied concentrations of NAD^+ to determine steady state kinetics for NAD^+. All reactions were set up in duplicate. Reaction mixes were incubated five minutes, stopped by the addition of methanol to 50% (v/v), and analyzed by HPLC for product formation using the gradient and solvent system described above

in section 2.2.4.1. The area under the curve (AUC) of the product shown on the HPLC chromatogram was used to determine the initial rate of reaction at each substrate concentration. A calculated conversion factor based on the AUC of a fixed concentration of rifampin at 340 nm was used to convert the product AUC into units of molarity. Data for NAD^+ were fit to Equation 1 for Michaelis-Menten kinetics, and data for rifampin were fit to Equation 2 for substrate inhibition using the computer software GraFit [53].

$$v = V_{max} S / (K_m + S) \quad (1)$$

$$v = V_{max} S / (K_m + S (1 + S/K_i)) \quad (2)$$

v = initial reaction velocity
V_{max} = maximum velocity of the reaction
S = substrate concentration
K_m = substrate concentration at half V_{max}
K_i = binding constant

2.2.4.3 Assay Validation

Steady state kinetic parameters for each of the rifampin ADP-ribosyl transferase enzymes were determined based on the assumption that the extinction coefficient for rifampin and ADP-ribosyl rifampin is the same at 340 nm. To validate these results ADP-ribosyl rifampin was purified and the extinction coefficient was calculated at 340 nm and compared to that of rifampin.

Purification of product was carried out by thin layer chromatography (TLC) using Uniplate Silica Gel GF, 20x20 cm, 2000 micron TLC plates in a solvent system of chloroform: methanol, 9:2. Reactions were prepared in 6.5 mL volume of 50 mM HEPES pH 7.5 with 2.0 mM rifampin and 2.0 mM NAD^+ and incubated for 2 hours. Samples were lyophilized overnight, re-dissolved in chloroform-methanol (9:2), and spotted onto the TLC plate. Product

was visualized by its orange colour (Rf = 0.2). The band was extracted from the plate and dissolved in methanol with assistance of sonication. Methanol was removed from the sample by evaporation and the sample was dissolved in 50% acetonitrile and water, lyophilized and stored at -80°C.

Rifampin and ADP-ribosyl rifampin were each dissolved in methanol in 10 mL volumetric flasks and absorbance was read at 340 nm on a Cary UV Visible Spectrophotometer. The extinction coefficient of each compound was calculated using Equation 3, Beers Law.

$$A = \varepsilon lc \tag{3}$$

A = absorbance
ε = extinction coefficient
l = path length (1 cm)
c = concentration

2.2.5 Spectroscopic Studies

2.2.5.1 Circular Dichroism Spectroscopy

Circular Dichroism (CD) spectroscopy was used to investigate observable changes in the secondary structure of ARR-2 upon binding substrates rifampin and NAD^+. CD spectra of ARR-2 samples were recorded using an AVIV CD Spectrometer, Model 215, using a 1 mm path length quartz cell. Samples were scanned from 260 to 190 nm at 25°C. Samples contained 0.25 mg/mL ARR-2 in 50 mM phosphate buffer pH 7.0. To examine changes in the secondary structure of ARR-2 in the presence of substrate, samples were prepared containing 0.25 mg/mL ARR-2 in 50 mM phosphate buffer pH 7.0 with 0.025 mM rifampin, 0.025 mM NAD^+, or 0.025 mM of both rifampin and NAD^+. All samples were baseline corrected using baseline spectra for phosphate buffer alone as well as buffer with rifampin, NAD^+, and both substrates where appropriate.

2.2.5.2 Fluorescence Spectroscopy

Further examination of conformational changes in ARR in response to binding rifampin was carried out using the innate fluorescence of tryptophan residues in ARR. These experiments were done using both ARR-2 and ARRs. Samples with ARR-2 contained 10 nM ARR-2 in 50 mM phosphate buffer pH 7.0 with addition of 1.25 mM rifampin in increasing volumes from 2-200 μL. Samples with ARRs contained either 100 μM or 0.5 mM ARRs in 50 mM HEPES pH 7.5 with addition of 10 mM or 0.125 mM rifampin in increasing volumes from 2-200 μL. Tryptophan fluorescence was selected by excitation at 295 nm and emission spectra were obtained by scanning between 310 and 430 nm. Fluorescence measurements were performed on the PTI Fluorescence System in 1 cm path length quartz cuvettes at room temperature. All fluorescence spectra were baseline corrected.

2.2.6 Proteolysis Studies

The susceptibility of ARR-2 to trypsin, chymotrypsin, elastase, and subtilisin proteases was assessed by 15% SDS-PAGE. Reaction tubes were prepared containing 5 μg of ARR-2 in 20 mM HEPES pH 7.5 in the presence of 4 μg/mL, 6 μg/mL, and 10 μg/mL of each protease, and 10 x reaction buffer (500 mM HEPES pH 7.5, 400 mM KCl, and 100 mM $MgCl_2$) and incubated up to 45 minutes at room temperature. Aliquots were taken from each reaction tube at 0, 5, 10, 15, 20, 25, 30, and 45 minutes and quenched by addition to 100 mM PMSF plus 2 x SDS-PAGE loading dye. Samples were applied to 15% SDS polyacrylamide gels for analysis of digestion patterns in ARR-2 resulting from exposure to each of the protease enzymes. Susceptibility of ARR-2 to trypsin digestion was further examined in the presence of rifampin and NAD^+. Reactions were prepared containing 5 μg of ARR-2 in 20 mM HEPES pH 7.5 in the presence of 6 μg/mL trypsin, 1 mM rifampin or 1 mM NAD^+, and 10 x reaction buffer (500 mM

HEPES pH 7.5, 400 mM KCl, and 100 mM $MgCl_2$). Reactions were incubated up to 45 minutes. Aliquots were taken from each reaction tube at 0, 5, 10, 15, 20, 25, 30, and 45 minutes, quenched by addition of 100 mM PMSF plus 2 x SDS-PAGE loading dye, and analyzed by 15% SDS-PAGE. Susceptibility of ARRm to trypsin digestion in the presence of rifampin and NAD^+ was also examined following the same protocol as described for ARR-2.

Activity of trypsin digested ARR-2 and ARRm was assessed and compared to the activity of full length enzyme using reverse phase HPLC with the gradient and solvent system described in section 2.2.4.1. Five micrograms of each ARR-2 and ARRm were incubated with 6 μg/mL trypsin for 15 minutes to digest 50% of the enzyme. Activity of digested ARR-2 and ARRm was then examined at two substrate concentrations. Reactions were prepared in 100 μL of 50 mM HEPES pH 7.5, 0.5 nmole of digested or full length protein, and 0.5 mM rifampin and 0.5 mM NAD^+, or 1.0 mM rifampin and 1.0 mM NAD^+. All reactions were set up in duplicate. Reactions were incubated five minutes, stopped by the addition of methanol to 50% (v/v), and analyzed for product formation by HPLC.

2.2.7 Protein ^{15}N-^{1}H NMR

Heteronuclear Single Quantum Correlation Spectroscopy (HSQC) experiments were used to further characterize protein conformational changes upon interaction of ARR-2 with substrate. ^{15}N-labeled ARR-2 was obtained by purification of the protein (as described in section 2.2.3.2) from cells grown in Spectra 9 minimal medium supplemented with isotopically enriched with ^{15}N. HSQC experiments were carried out on samples of ^{15}N-labeled ARR-2 containing 0.2 mM protein in 500 μL of 50 mM HEPES, 50 mM NaCl buffer pH 7.0, 0.5 M urea and 5% D_2O. Effects of ligand binding were observed by the addition of 1.0 mM rifampin, 1.0 mM NAD^+, 1.0

mM ADP-ribosyl rifampin (purified according to procedures in section 2.2.4.3), or 1.0 mM of each rifampin and NAD^+. Spectra were recorded at a temperature of 298 K on a Bruker AV 700 MHz spectrometer equipped with a TCI cryo-probe. NMR experiments were carried out using methods as performed in the Melacini Lab, McMaster University, (Hamilton, ON), described below. The ^1H and ^{15}N carrier frequencies were set at the water resonance and at the center of the amide ^{15}N region respectively. The ^{15}N dimension was digitized with 128 complex points for a spectral width of 31.8 ppm, and the ^1H dimension was digitized with 512 complex points for a spectral width of 14.2 ppm. The GARP pulse train implemented with an RF strength of 1.32 kHz was used during ^1H acquisition to decouple ^{15}N. Spectra were acquired using 8 scans per transient following 64 dummy scans, using an inter-scan delay of 1 sec. Spectra were sensitivity and gradient enhanced and included water-flip back pulses. All data sets were processed using Xwinnmr (Bruker Inc.) or NMRPipe [54].

2.2.8 Isothermal Titration Calorimetry Experiments

Further investigation of binding of rifampin and NAD^+ to ARR was done using Isothermal Titration Calorimetry (ITC). These experiments were carried out using both ARRm and ARR-2. ITC measurements were made using a MicroCal VP-ITC isothermal titration calorimeter from MicroCal, Inc. (Northampton, MA). For titrations with rifampin, a 40 μM solution of ARRm or ARR-2 in 20 mM HEPES pH 7.5 was added to the sample cell. The injection syringe was loaded with 0.2 mM rifampin for titration into ARRm; 0.6 mM rifampin for titration into ARR-2. For these experiments rifampin was dissolved in 20 mM HEPES using sonication. For titrations with NAD^+, a 50 μM solution of ARRm or ARR-2 in 20 mM HEPES pH 7.5 was added to the sample cell, and the injection syringe was loaded with 1.0 mM NAD^+.

Each titration began with a 60 s delay followed by injections of titrant solution spaced apart by 300 s. Titration of rifampin into ARRm was done using 14 injections of 20 µl of titrant; titration of rifampin into ARR-2 was done using 18 injections of 15 µl of titrant; titration of NAD^+ into ARRm and ARR-2 was done using 29 injections of 10 µl of titrant. In each titration the sample cell was stirred at 300 rpm, and the temperature was maintained at 30°C throughout the experiment. Additional experiments were performed as described above using a 100 µM solution of ARRm in 20 mM HEPES pH 7.5 in the sample cell and 1.0 mM NAD^+ in the injection syringe, as well as using a 50 µM solution of ARRm in 20 mM HEPES pH 7.5 in the sample cell, with 5.0 mM NAD^+ in the injection syringe. For these titrations 29 injections of 10 µl titrant were used. Control titrations of substrate into buffer were also performed. Titration data were analyzed using Origin 5.0 software supplied by Microcal. Data were fit to a theoretical titration curve describing one binding site for titrant.

2.3 Results

2.3.1 Amplification of the arr-2 *gene and Overexpression and Purification of ARR Enzymes*

Using the pCTF1 plasmid as template DNA and primer pairs complementary to the 5' terminal and 3' terminal of the *arr-2* gene, DNA fragments of 0.45 kb were amplified by PCR (Figure 2-1). The bands were visualized on 1 % TAE-agarose gels and shown to be consistent with the predicted size of the *arr-2* gene in the Genbank data base. The sequence of the amplified *arr-2* was verified by sequencing of the entire gene at the MOBIX Central Facility of McMaster University.

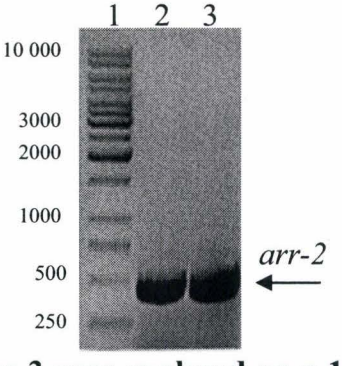

Figure 2-1. Amplification of the *arr-2* gene analyzed on a 1 % TAE-agarose gel. Lanes 2 and 3 show the PCR amplified *arr-2* gene at approximately 450 bp. Lane 1 shows the standard 1 kb DNA ladder.

The amplified gene was inserted into a pET28a (+) expression vector treated with *Nde I* and *Hind III* endonucleases. As described in section 2.2.2, the *arr* genes encoding the ARR enzymes from *S. coelicolor* and *M. smegmatis* were previously cloned into the pET15b (+) and pET22b (+) expression vectors by respective past lab members David Boehr and Matthew Crouch. The pET28a (+) and pET15b (+) expression vectors each encode an N-terminal hexa His-tag and a T7 promoter for protein overexpression. The pET22b (+) expression vector encodes the T7 promoter for protein overexpression. The hexa His-tagged proteins, ARR-2 and ARRs were overexpressed and purified using a 5 mL HiTrap chelating column. Although

ARRm could be expressed from the pET15b (+) encoding a hexa His-tag, protein expression was greater when expressed from the pET22b (+) vector. The ARRm protein was purified using a HiPrep Q Sepharose column, followed by a HR 5/5 Phenyl Superose column. All proteins were analyzed using 15% SDS-PAGE, showing bands consistent with the predicted molecular weights of 15.3 kDa, 15.9 kDa, and 16.9 kDa for ARRs, ARRm and ARR-2 respectively (Figure 2-2).

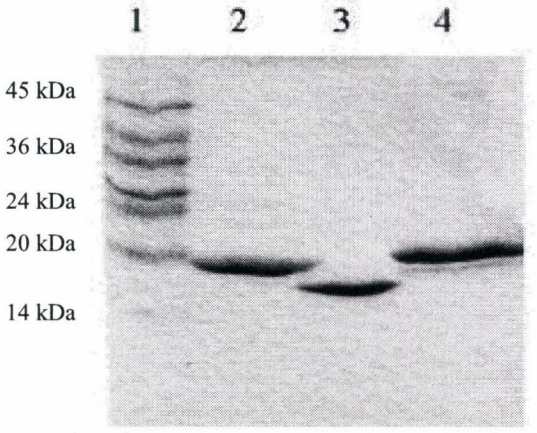

Figure 2-2. SDS-PAGE analysis of ARR enzymes. Lane 1 – low molecular mass standards: bovine serum albumin (66kDa), chicken egg ovalbumin (45 kDa), glyceraldehyde-3-phosphate dehydrogenase (36 kDa), carbonic anhydrase (29 kDa), trypsinogen (24 kDa), trypsin inhibitor (20 kDa), and lysozyme (14 kDa); Lane 2 – purified *S. coelicolor* ARR (ARRs) protein; Lane 3 – purified *M. smegmatis* ARR (ARRm) protein; Lane 4 – purified ARR-2 protein. The ARRs and ARR-2 enzymes migrate as larger proteins on SDS-PAGE.

Table 2-4. Summary of the ARRs, ARRm and ARR-2 predicted and observed molecular weights (kDa) as seen on SDS-PAGE, and the average yield of each protein in mg/mL from a 1 L culture.

Protein	ARRs	ARRm	ARR-2
Predicted Molecular Mass (kDa)	16.1	15.9	17.7
Observed Molecular Mass (kDa)	19	16	20
Average Yield (mg/L)	20	65	50

2.3.2 HPLC Assay Development

Following purification of each of the ARR enzymes, Liquid Chromatography/ Mass Spectrometry (LC/MS) was used to confirm their activity. Figure 2-3 shows the LC/MS analysis of the formation of ADP-ribosyl rifampin, the product of the reaction of ARR and its substrates rifampin and NAD^+ for each of the ARR enzymes. The predicted molecular weight of ADP-ribosyl rifampin is 1364.24; the observed masses for products of the reactions with ARRs, ARRm, and ARR-2 are 1362.6, 1362.7, and 1362.7, $[M-2H]^-$ respectively.

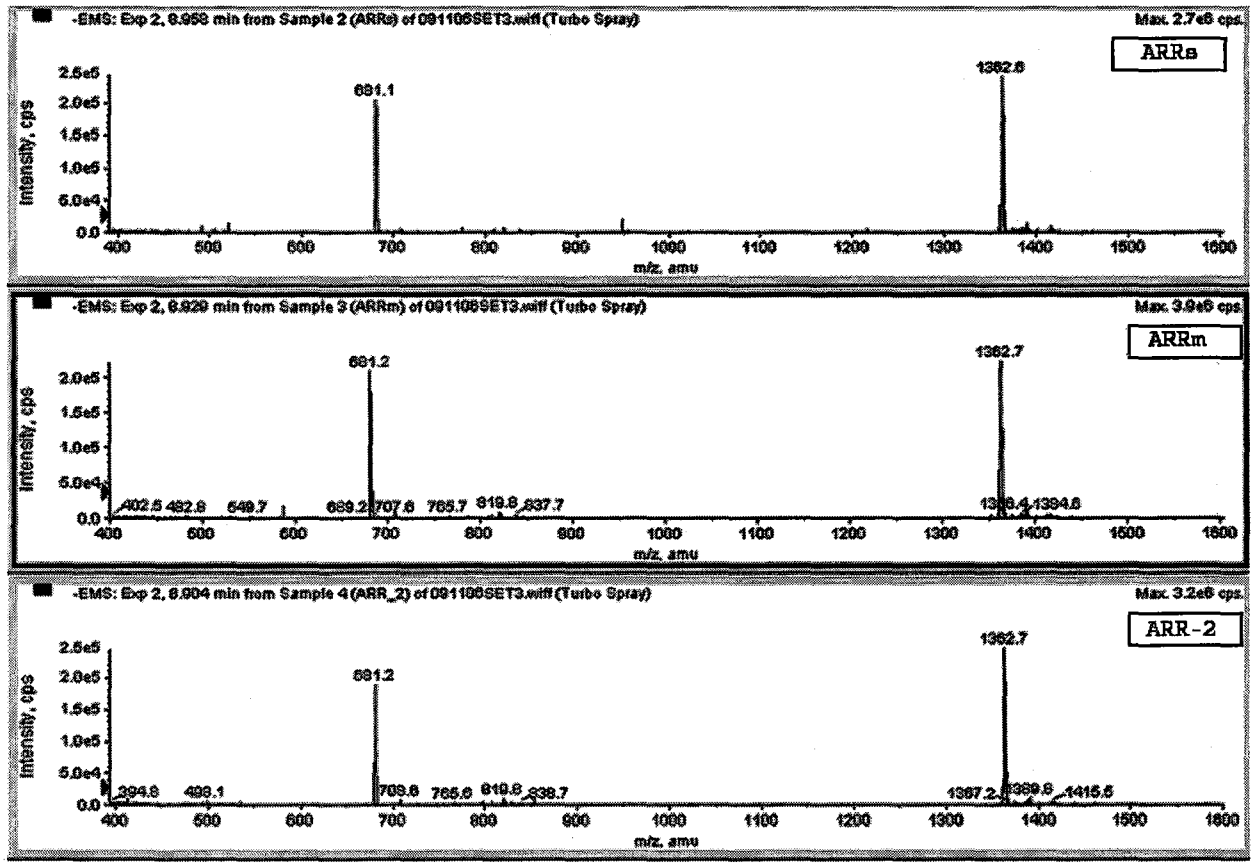

Figure 2-3. Liquid Chromatography/Mass Spectrometry (LC/MS) analysis of ADP-ribosyl rifampin. The presence of ADP-ribosyl rifampin, produced by the reactions between the ARR enzymes and rifampin and NAD^+, was confirmed by electrospray LC/MS analysis, showing masses of $[M-2H]^-$ of 1362.6, 1362.7, and 1362.7 for ARRs, ARRm, and ARR-2 respectively.

Determination of steady-state kinetic parameters for the ARR enzymes was carried out using a discontinuous reverse phase HPLC assay. In this type of assay, reagents are incubated together allowing the reaction to proceed for a fixed amount of time. Reactions are then terminated and analyzed for formation of product or consumption of substrate.

2.3.2.1 Initial Velocity studies

In a discontinuous assay, progress curves must be generated at several substrate concentrations and used to establish an initial rate region for the reaction during which the velocity of the enzyme is constant. Reactions were prepared for each of the ARR enzymes in 1.5 mL eppendorf tubes at three concentrations of substrate, 0.1 mM, 0.5 mM, or 1.0 mM, with 1 nmole of ARR. Reactions were incubated up to 45 min, and 100 µl aliquots were taken from the tube at fixed time points and terminated with the addition of 100 µl methanol. Aliquots of 100 µl of each of the reaction time points were taken and injected onto a DIONEX C18 column equilibrated in 0.05 % Trifluoroacetic acid (TFA) (v/v) (Solvent A). The chromatogram in Figure 2-4 shows an example of the formation of product and consumption of substrate at 220 nm, in the reaction between the ARR-2 enzyme 0.5 mM rifampin and 0.5 mM NAD^+ from 0 to 45 minutes. Chromatogram 1 shows the substrates NAD^+ and rifampin with respective retention times of 1.9 min and 10.8 min. The reaction was initiated by addition of 1 nmole ARR-2. Chromatograms 2 to 10 show the appearance and increase of a product peak at 8.5 min over 2 to 45 min.

The product area under the curve was plotted against time to generate progress curves for the reaction. A tangent to the curve can be drawn to determine the linear part of the curve from

which the initial rate range for the reaction can be estimated to be approximately 5 min (Figure 2-5).

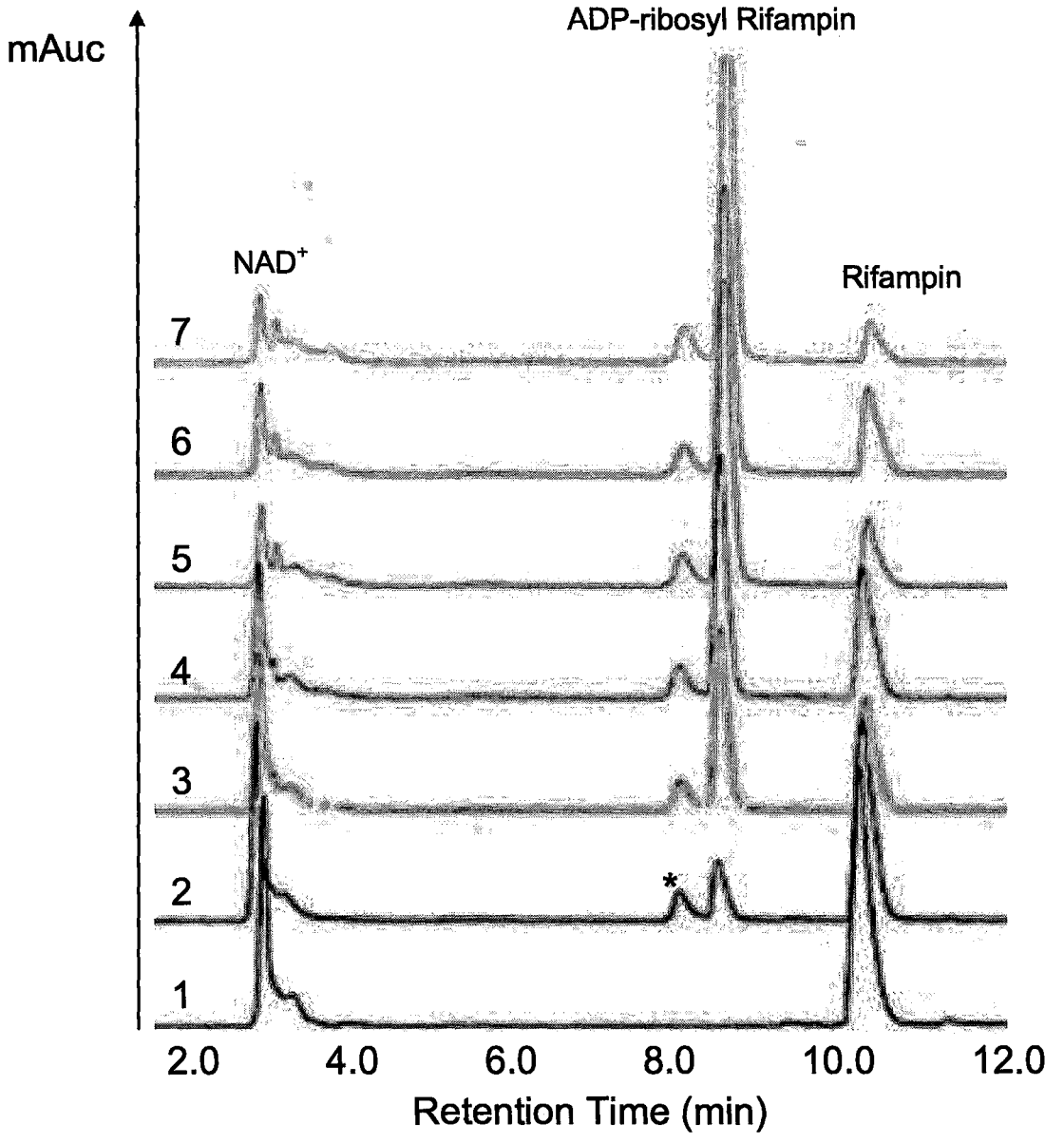

Figure 2-4. HPLC analysis of the ADP-ribosyl transferase reaction, catalyzed by the ARR-2 enzyme over a 45 minute incubation time. NAD^+ and rifampin substrate peaks are observed at 220 nm at retention times of 1.9 min and 10.8 min respectively. Product is eluted using a linear gradient in acetonitrile/0.05% TFA (v/v) (Solvent B), showing a peak at a retention time of 8.5 min at 220 nm. As NAD^+ and rifampin are consumed, an increase in product peak is observed. Chromatograms are numbered according to time: 1 – 0 min, 2 – 2 min, 3 – 5 min, 4 – 10 min, 5 – 15 min, 6 – 30 min, and 7 – 45 min. The asterisk indicates the protein peak on the chromatogram.

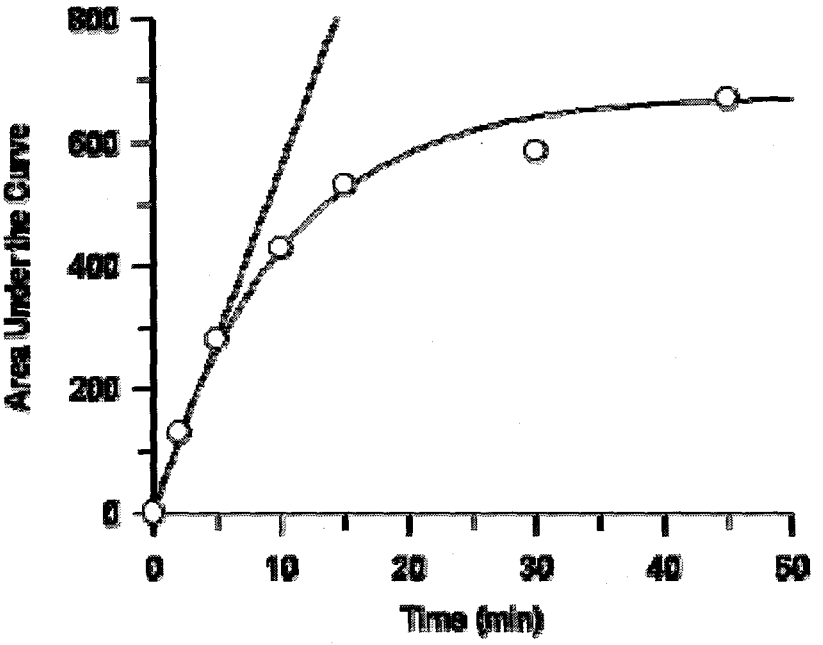

Figure 2-5. Example of a progress curve used to calculate the initial rate range of the reaction. Product area under the curve at 340 nm is plotted against time to generate a progress curve for the reaction over 45 minutes. A tangent can be drawn to the curve to determine the linear range of the reaction. Once identified, the linear range of the reaction can be used to determine an optimal reaction time that can be used for determination of steady state kinetic parameters in a discontinuous assay. For the reaction with the ARR enzymes, the linear initial rate range was determined to be 5 minutes.

2.3.2.2 Steady-State Kinetics of ARR Enzymes

After establishing the initial rate range of the reaction the steady-state kinetic parameters for rifampin and NAD^+ were determined for each of the ARR enzymes using reverse phase HPLC. Reactions were initiated by addition of 1 nmole ARR and terminated after 5 min with addition of methanol to 50% (v/v). Samples were injected onto a DIONEX C18 column equilibrated in 0.05% Trifluoroacetic acid (TFA) (v/v) (Solvent A) in 100 µl volumes. Products were eluted using a linear gradient in acetonitrile/0.05% TFA (v/v) (Solvent B) at a flow rate of 1.0 mL/min.

The area under the curve (AUC) of the product as shown on the HPLC chromatogram was then used to determine the initial rate of the reaction at each substrate concentration in area

units per minute. At 340 nm, rifampin and the product of the reaction both have absorbance maxima. Based on the assumption that the extinction coefficient for each is the same at 340 nm, area units can be converted into units of molarity using the AUC of rifampin at a known substrate concentration to determine a conversion factor. The average AUC for rifampin at a fixed concentration was calculated and used to determine the concentration of 1 area unit, which was used as a conversion factor to convert area units to concentration (nM). This was validated by determination of the extinction coefficient of the purified product of the reaction ($\varepsilon_{340,\ rif}$ = 2229.2; $\varepsilon_{340,\ product}$ = 2364.0). Purity of ADP-ribosyl rifampin was assessed using LC/MS analysis (Figure 2-6).

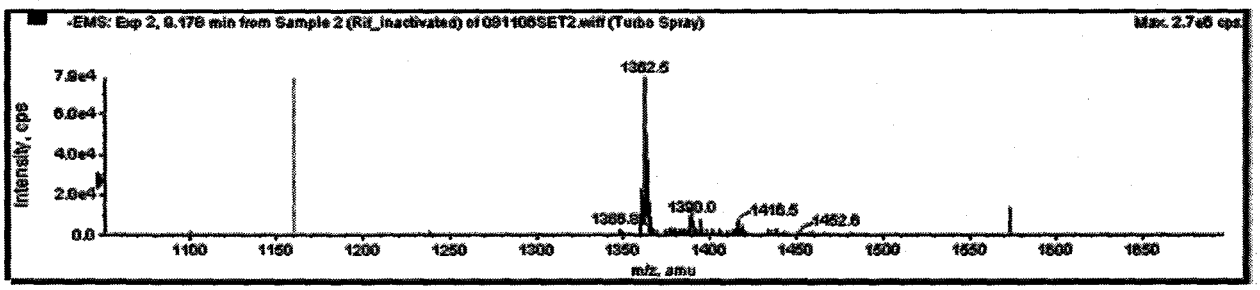

Figure 2-6. LC/MS analysis of purified ADP-ribosyl rifampin. The reaction between the ARR enzymes and rifampin and NAD^+ produces an inactivated ADP-ribosyl form of rifampin, with an expected mass of 1364.24. LC/MS analysis of the purified reaction product shows a mass of $[M-2H]^-$ of 1362.5.

GraFit software was used to fit data to Michaelis-Menten curves (Figure 2-7, 2-8, and 2-9).

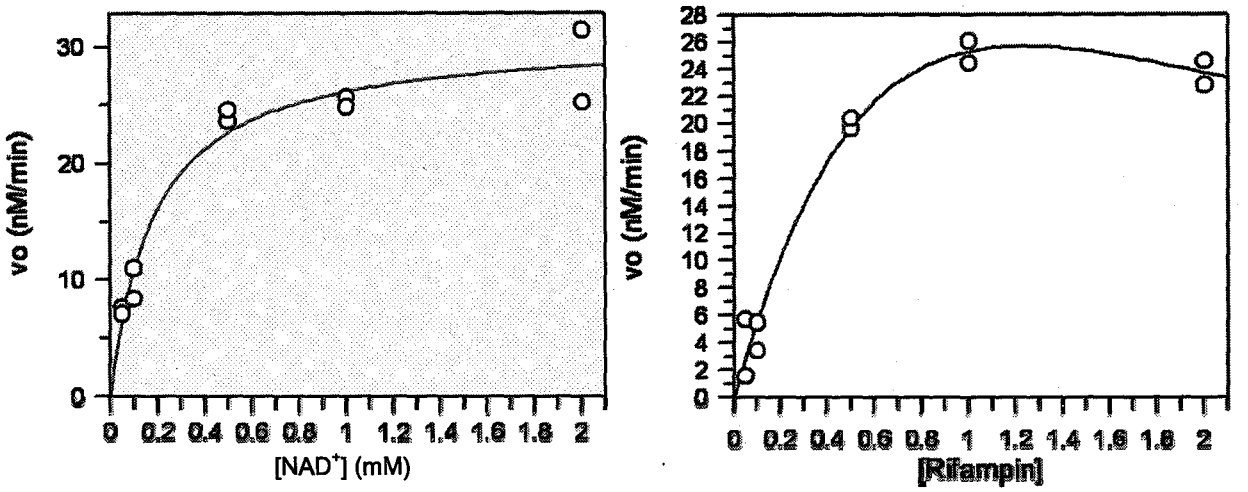

Figure 2-7. Michaelis-Menten curves for determination of steady-state kinetic data of NAD^+ and rifampin for the ARRm enzyme. Data for NAD^+ were fit to Equation 1; data for rifampin were fit to Equation 2 for substrate inhibition.

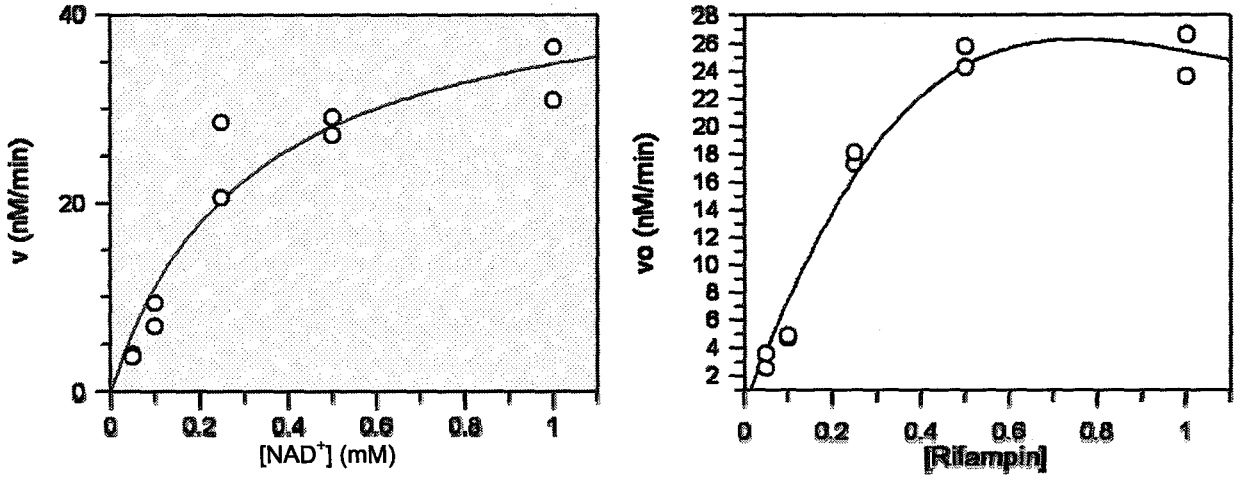

Figure 2-8. Michaelis-Menten curves for determination of steady-state kinetic data of NAD^+ and rifampin for the ARRs enzyme. Data for NAD^+ were fit to Equation 1; data for rifampin were fit to Equation 2 for substrate inhibition.

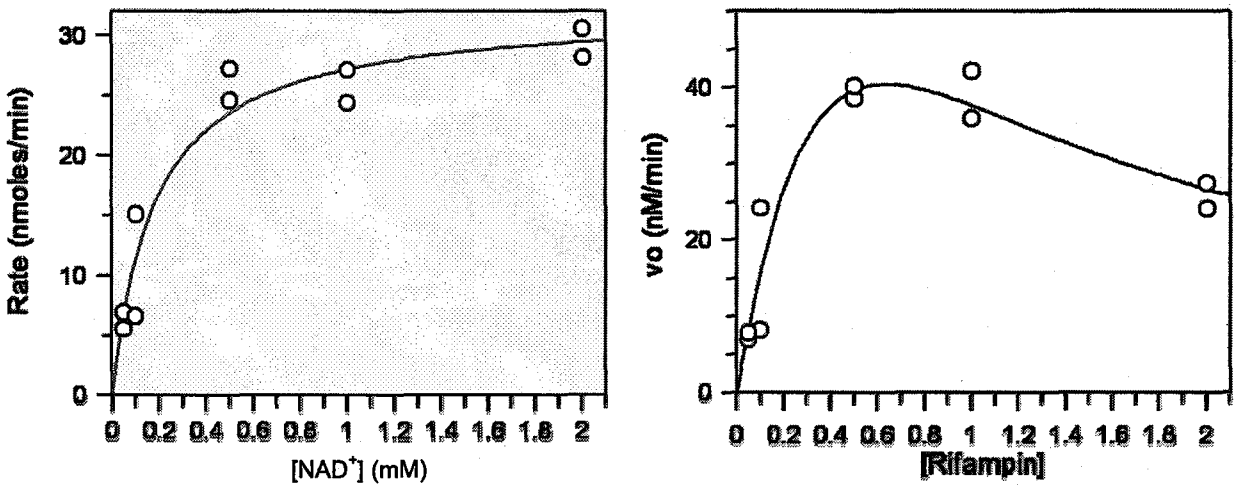

Figure 2-9. Michaelis-Menten curves for determination of steady-state kinetic data of NAD^+ and rifampin for the ARR-2 enzyme. Data for NAD^+ were fit to Equation 1; data for rifampin were fit to Equation 2 for substrate inhibition.

Table 2-5 summarizes the kinetic parameters calculated for rifampin ADP-ribosyl transferase enzymes.

Table 2-5. Steady-State Kinetic Parameters of ARR Enzymes

Enzyme	Substrate	K_m (mM)	K_i (mM)	k_{cat} (s^{-1})	k_{cat}/K_m ($s^{-1}M^{-1}$)
M. smegmatis ARR	Rifampin	1.42±0.38	1.07±0.35	2.84±0.57	$2.00x10^3$
	NAD^+	0.18±0.04		0.98±0.05	$5.44x10^3$
S. coelicolor ARR	Rifampin	2.80±0.80	0.20±0.07	7.34±1.90	$2.62x10^3$
	NAD^+	0.31±0.11		1.52±0.21	$4.87x10^3$
ARR-2	Rifampin	0.74±0.34	0.55±0.30	4.48±1.49	$6.05x10^3$
	NAD^+	0.18±0.05		1.02±0.07	$5.67x10^3$

2.3.3 CD Spectroscopy and Trp Fluorescence

The CD spectrum of uncomplexed ARR-2 demonstrates significant negative ellipticity at approximately 208 nm indicative of the α-helical component of the enzyme (Figure 2-10). Addition of NAD^+ had no observable effect on the resulting spectra (Figure 2-10), indicating that there were no significant changes to the secondary structure of ARR-2 upon binding to NAD^+. The addition of rifampin showed a significant decrease in the ellipticity of the CD spectrum of

ARR-2 at 208 nm, indicating the possibility of a secondary structure rearrangement in ARR-2 by the binding of rifampin (Figure 2-10). Addition of both NAD^+ and rifampin showed a greater decrease in the ellipticity of the CD spectrum of ARR-2 at 208 nm, again indicating the possibility of further rearrangements in secondary structure of ARR-2 when both substrates were bound and a reaction was allowed to occur (Figure 2-10).

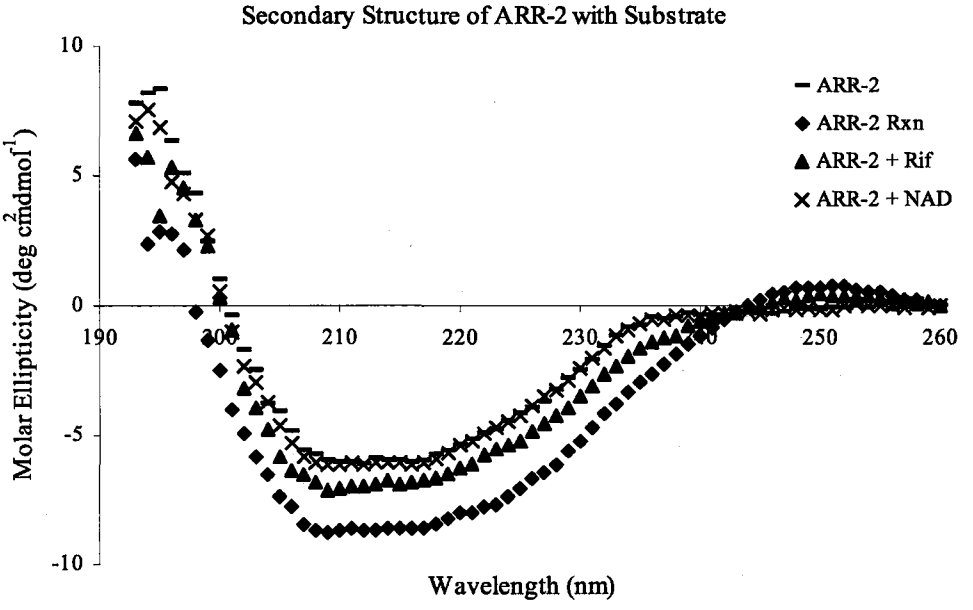

Figure 2-10. Influence of substrates, NAD^+ and rifampin on the CD spectra of ARR-2. Spectra for free and complexed forms of the ARR-2 enzyme are shown according to the legend above.

Results of CD spectroscopy show a conformational change in the ARR-2 enzyme upon interaction with rifampin, but not upon interaction with NAD^+. This suggest that while it is possible that NAD^+ may not induce a significant conformational change on binding, or that the enzyme was prurified in the presence of NAD^+ thus no change was observed, it is also possible that NAD^+ may not be able to bind ARR in absence of rifampin. Tryptophan fluorescence was employed to examine further the binding interactions between ARR and its substrates.

There are three Trp residues within the ARR-2 protein, one in the N-terminus at position 4, one in the central part of the enzyme at position 62, and one in the C-terminal region at position 122. In the ARRs protein, there are two Trp residues, both within the C-terminal region of the enzyme at positions 108 and 119. Titration of rifampin resulted in a decrease in Trp fluorescence for both ARR-2 and ARRs. Due to the absorbance of rifampin at 340 nm, accurate values for $[L]_{free}$ were unable to be calculated. The use of Trp fluorescence was not suitable for examination of binding interactions between ARR and its substrates.

2.3.4 Proteolysis Studies

Incubation of ARRm and ARR-2 with tryspin in the presence and absence of rifampin and NAD^+ resulted in digestion of the enzyme, and the production of a protein fragment of approximately 12.5 kDa (Figure 2-11). The pattern of digestion was the same for free ARR and ARR in complex with rifampin or NAD^+, suggesting the presence of a loop region accessible for proteolytic digestion that is unaffected by substrate-induced conformational changes. Binding of substrates did not protect ARRm or ARR-2 from proteolytic cleavage. Activity of digested ARR-2 and ARRm was assayed showing a loss of enzymatic activity upon digestion, indicating that full length ARR is required for enzymatic activity.

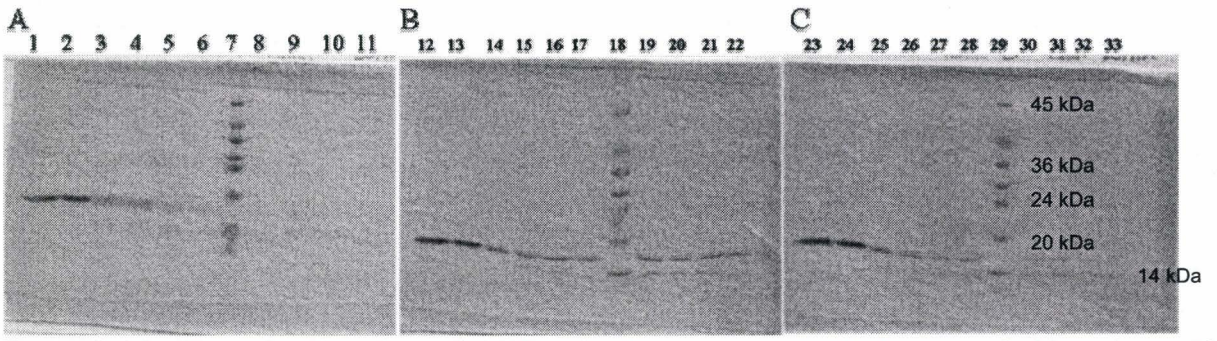

Figure 2-11. Trypsin digestion of ARRm in the presence and absence of rifampin and/or NAD^+. A – uncomplexed ARRm, B – ARRm in complex with rifampin, C – ARRm in complex with NAD^+. Lanes 1 and 2, 12 and 13, 23 and 24 - trypsin digest incubated 0 min, Lanes 3 and 4, 14 and 15, 25 and 26 – trypsin digest incubated 5 min, Lanes 5 and 6, 16 and 17, 26 and 28 – trypsin digest incubated 10 min, Lanes 8 and 9, 19 and 20, 30 and 31 – trypsin digest incubated 15 min, Lanes 10 and 11, 21 and 22, 32 and 33 – trypsin digest incubated 20 min, Lanes 7, 18, and 29 – low molecular mass standards.

2.3.5 Protein ^{15}N-^{1}H NMR

Based on CD results showing conformational changes to ARR-2 in the presence of rifampin but no change in the presence of NAD^+, ^{15}N-^{1}H heteronuclear correlation experiments were employed to further examine the interactions between the ARR-2 enzyme and its substrates, and to aid in the characterization of protein-induced conformational changes. Spectra were collected with native ARR-2 and compared to spectra collected with ARR-2 in complex with both substrate and reaction product. Correlation experiments demonstrated significant changes in the enzyme upon binding each of the substrates, rifampin and NAD^+, as well as upon binding ADP-ribosyl rifampin (Figure 2-12).

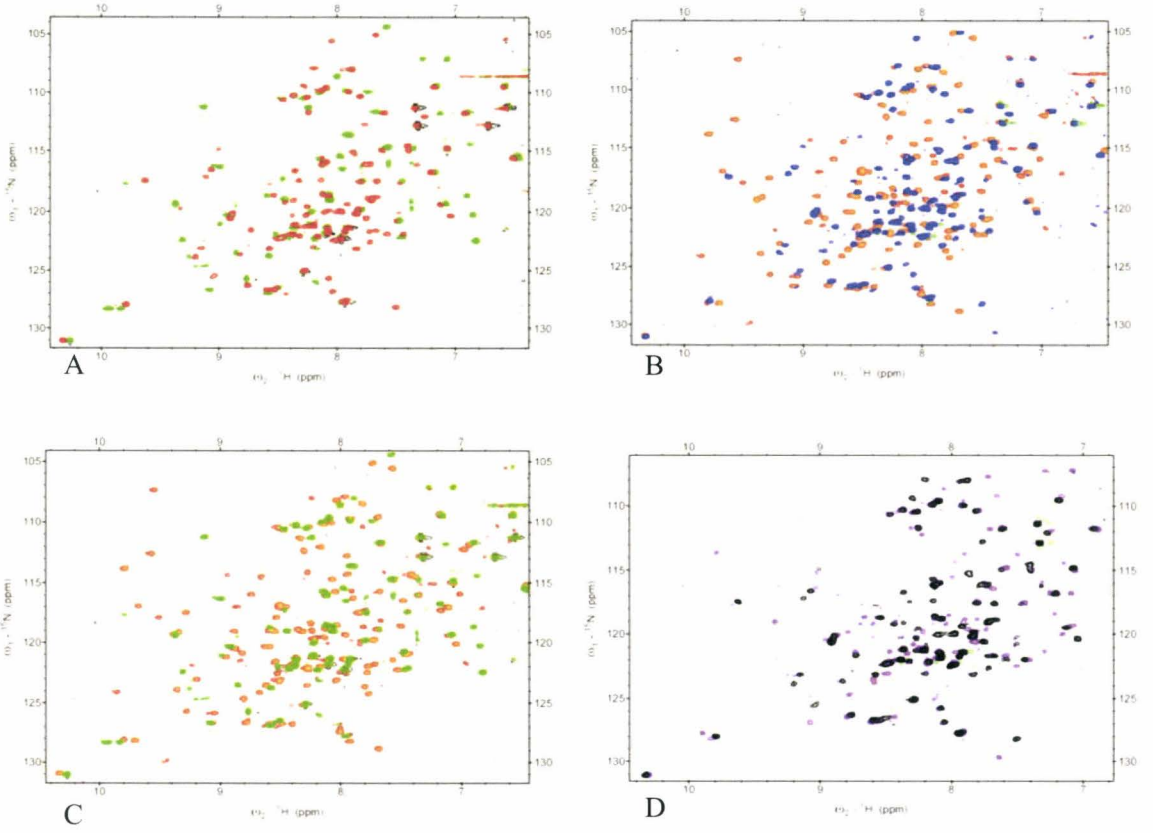

Figure 2-12. NMR-based evidence for ligand-induced conformational changes in ARR-2. ^{15}N-^{1}H spectra are shown for the ARR-2 enzyme in the presence of rifampin, NAD^+, and purified ADP-ribosylated rifampin. (A) Uncomplexed ARR-2 – red, ARR-2 with rifampin – green, (B) uncomplexed ARR-2 – blue, ARR-2 with NAD^+ - orange, (C) ARR-2 with rifampin – green, ARR-2 with NAD^+ - orange, (D) uncomplexed ARR-2 – black, ARR-2 with purified reaction product – purple. Ligands were present in molar excess.

Addition of rifampin and NAD^+ each demonstrated significant changes in the spectra of ARR-2 (Figure 2-12A and 2-12B). An overlay of these two spectra is shown in Figure 2-12C. Significant differences are seen in the dispersion pattern of ARR-2 in complex with rifampin and NAD^+, indicating a difference in the conformation of the enzyme when bound to each substrate. Figure 2-12D shows a comparison of the ^{15}N-^{1}H heteronuclear correlation between native ARR-2 and ARR-2 bound to ADP-ribosyl rifampin. Again it can be noted that there are significant changes in chemical shift dispersion when the enzyme is interacting with the product of the reaction. The changes in ^{15}N and ^{1}H chemical shift dispersion observed in the spectra shown in

Figure 2-12 illustrate alterations in enzyme flexibility upon binding of product and substrate to the enzyme; the enzyme appears to become less flexible and more structured. There are 157 expected amide peaks derived from ARR-2, including Asn, Gln, Trp, and His sidechains. In the non-complexed enzyme, 101 peaks are clearly resolved (Figure 2-12), upon binding of NAD^+ (Figure 2-12B) the number of resolvable peaks increases to 127, indicating significant conformational changes in ARR-2 are induced by these interactions. NMR data confirm that both rifampin and NAD^+ are able to bind the enzyme individually and that binding of rifampin is not required for ARR to bind NAD^+.

2.3.6 ITC Studies

To further investigate the binding of rifampin and NAD^+ to ARR and gain a better understanding of the interactions of each substrate with the enzyme, ITC studies were employed. These experiments were carried out using the ARR-2 and ARRm enzymes. The ITC profiles for rifampin binding ARRm and ARR-2 are shown in Figures 2-13 and 2-14 respectively. Titration data for rifampin binding each ARRm and ARR-2 was best fit to a theoretical model binding curve that describes one binding site for the titrant. The K_d values with the lowest standard error are 2.83 ± 0.32 μM and 0.48 ± 0.05 μM for ARRm and ARR-2 respectively, much lower than K_m values reported in Table 2-5. Based on the assumption that inactivation of rifampin occurs by either an ordered Bi Bi reaction mechanism in which NAD^+ likely binds first, or a random Bi Bi reaction mechanism in which either substrate may bind first, K_d and K_m for rifampin will not be equal. Binding constants for rifampin measure the specific interaction between free ARR and rifampin in the absence of NAD^+. The K_m values are calculated for ARR in the presence of both

rifampin and NAD^+ and therefore are measuring the binding of rifampin under conditions in which NAD^+ may or may not already be bound to the enzyme.

The ITC profiles for NAD^+ binding ARRm and ARR-2 are shown in Figures 2-15 and 2-16 respectively. Data collected for the titration of ARRm with NAD^+ could not be fit to a binding curve as no change in heat absorption was observed (Figure 2-15). Titration data recorded for NAD^+ binding ARR-2 appeared to suggest a best fit to a model describing one binding site, although data could not be fit to this type of binding curve without increasing amounts of error. Attempts were made to fit the data to a model for two binding sites, however again high error values prevented the data from accurately fitting this model. Based on titration results for NAD^+ with ARRm and ARR-2 a K_d value could not be calculated, suggesting that NAD^+ may already be tightly bound to the enzyme when purified. NMR data would indicate that this is not the case, and that ITC simply may not be a suitable technique for measuring binding affinities for this enzyme. Further examination of the binding of NAD^+ to the ARR enzyme is necessary to understand the interaction between these enzymes and their substrates.

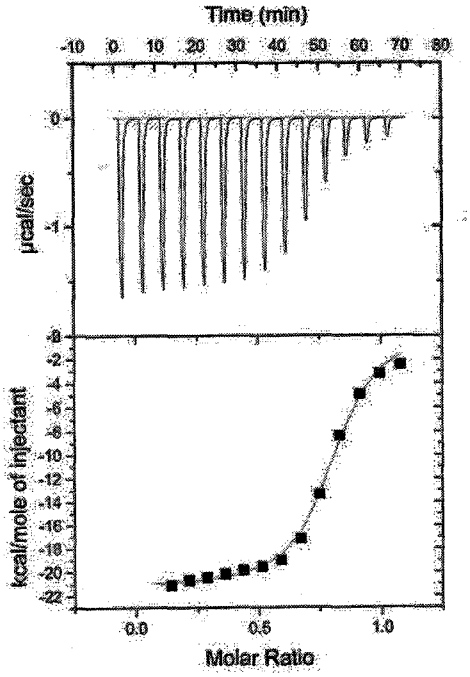

Figure 2-13. ITC profile of ARRm with rifampin as the titrant. Top: raw experimental data from 14 automatic injections of 20 µL each of 0.2 mM rifampin. Bottom: integrated titration curve to a model describing one binding site for rifampin.

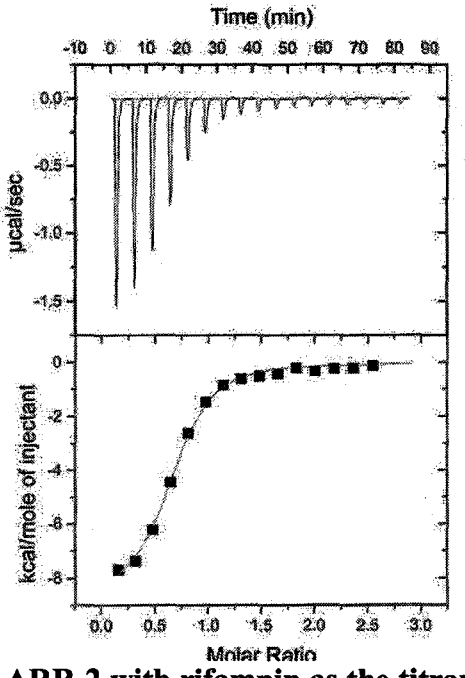

Figure 2-14. ITC profile of ARR-2 with rifampin as the titrant. Top: raw experimental data from 18 automatic injections of 15 µL each of 0.6 mM rifampin. Bottom: integrated titration curve to a model describing one binding site for rifampin.

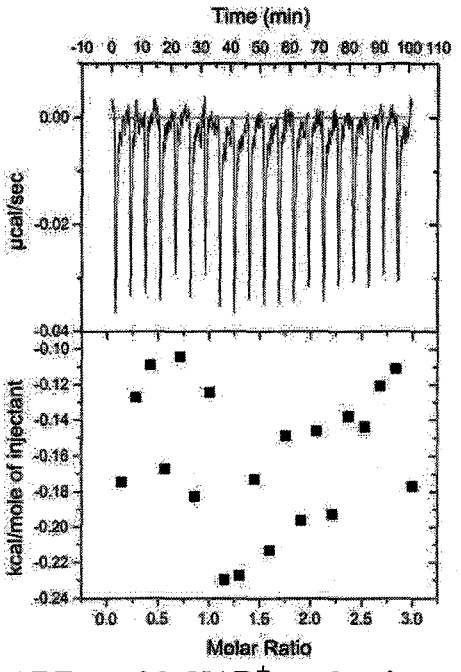

Figure 2-15. ITC profile of ARRm with NAD^+ as the titrant. Top: raw experimental data from 29 automatic injections of 10 µL each of 1.0 mM NAD^+. Bottom: data points were not able to be integrated as no titration was observed.

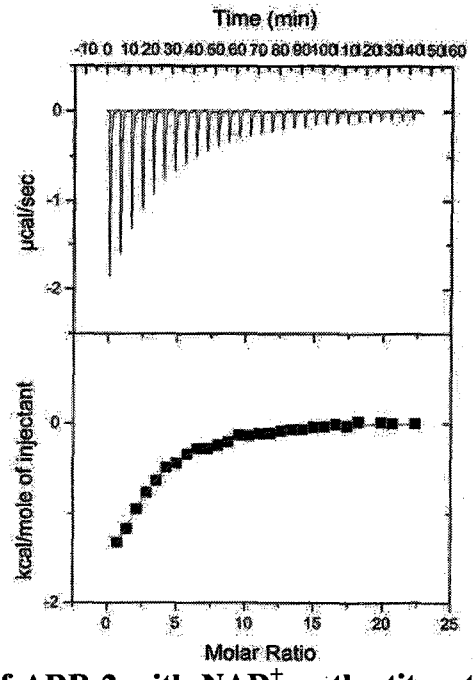

Figure 2-16. ITC profile of ARR-2 with NAD^+ as the titrant. Top: raw experimental data from 29 automatic injections of 10 µL each of 1.0 mM NAD^+. Bottom: attempt to integrate titration curve to a model describing two binding sites for NAD^+. Data points however were unable to be successfully integrated into titration curves describing one or two independent binding sites for NAD^+.

2.4 Discussion and Concluding Remarks

To gain insight into the mechanism of action and catalytic properties of these unique ADP-ribosylating enzymes, rifampin ADP-ribosyl transferases from three sources, two chromosomal copies from *S. coelicolor* (ARRs) and *M. smegmatis* (ARRm) (constructs made by David Boehr and Matthew Crouch) and one Tn-encoded copy isolated from *P. aeruginosa* (ARR-2), were cloned and overexpressed in *E. coli.* Each of the ARR enzymes was purified (Figure 2-2) and used in studies to determine kinetic and structural properties.

The inactivation of rifampin by the ARR enzyme is a bisubstrate reaction involving the transfer of the ADP-ribose moiety from NAD^+ to rifampin. To determine the catalytic efficiency of the ARR enzyme a reverse phase discontinuous HPLC assay was developed. Prior to assay development, LC/MS analysis was used to confirm the activity of each of the ARR enzymes by detection of the mass of the reaction product (Figure 2-3).

To characterize the catalytic efficiency of this inactivation reaction, kinetic parameters K_m, V_{max}, and k_{cat}/ K_m must be determined. Progress curves were generated for each reaction at three substrate concentrations (0.1 mM, 0.5 mM, and 1.0 mM) over 45 minutes (Figure 2-4). The product area under the curve, as seen on the HPLC chromatogram was plotted against time and used to determine the initial rate range for the enzyme to be approximately five minutes (Figure 2-5). This is important in a discontinuous assay, as reactions cannot be monitored continuously for product formation and must be terminated before they can be analyzed.

After establishing the initial rate range of the reaction, steady-state kinetic parameters for rifampin and NAD^+ were determined for each of the ARR enzymes using the discontinuous HPLC assay. Reactions were initiated at five or six substrate concentrations by addition of 1 nmole ARR and terminated after 5 min with addition of methanol to 50% (v/v). The initial rate

of reaction was determined at each substrate concentration in area units per minute using the product area under the curve at 340 nm as seen on the HPLC chromatogram. To make the data comparable to reported kinetic parameters, area units were converted into units of molarity by use of a calculated conversion factor determined by the area under the curve of rifampin at a fixed concentration. Rifampin and the product of the reaction share the same extinction coefficient at 340 nm, thus validating the use of a conversion factor as an accurate means of modifying area units to concentration units.

Results of the kinetics assay are summarized in Table 2-5. The ARR enzymes from disparate sources are indistinguishable by their steady state kinetic parameters for each of the substrates. The catalytic efficiency of the ARR enzymes is on the order of 10^3, while enzymes considered to be evolutionarily perfect have k_{cat}/K_m values on the order of 10^{8-9}. Reported specificity constants of DT for NAD^+ and eEF-2 are on the order of 10^7 and 10^8 respectively, while reported values of ETA for NAD^+ and eEF-2 are lower, at 10^4 and 10^5 respectively [55, 56]. The k_{cat}/K_m values of ARR enzymes suggest that they may be present in the cell to serve another purpose and may have evolved to inactivate rifampin, or perhaps just have this activity by chance. Nevertheless, ARR enzymes confer a high level of rifampin resistance to E. coli when expressed in this organism. These enzymes therefore have sufficient catalytic efficiency to protect the cell from this class of toxic compounds. As a result there is apparently no evolutionary pressure to increase the catalytic efficiency any further.

To gain further insight into the interactions between these unique enzymes and their substrates, a series of ligand binding studies were conducted, the results of which are summarized in Table 2-6. CD spectroscopy was used to examine the secondary structure of the ARR-2 enzyme in the presence and absence of both rifampin and NAD^+. The CD spectra of

ARR-2 bound to NAD^+ showed no observable differences from that of ARR-2 alone (Figure 2-10), however upon addition of rifampin a decrease in ellipticity was observed, indicating that binding rifampin induced a change in the secondary structure of the enzyme (Figure 2-10). These results could have a number of different implications for the interaction between ARR and its substrates. Based on CD results, it is possible that the enzyme may need to bind rifampin and undergo a structural rearrangement before binding of NAD^+ is able to occur, or that the ARR enzyme was purified with NAD^+ already tightly bound, therefore the effects of binding could not be observed. It is also possible that NAD^+ binding was occurring but induced no significant change in the conformation of the enzyme. To understand the interactions between ARR and its substrates, a variety of other techniques can be employed, including determination of the kinetic mechanism, and various other thermodynamic techniques like Fluorescence, NMR, ITC or equilibrium dialysis.

The fluorescent properties of tryptophan residues and proteolysis studies were used to probe changes in enzyme conformation in response to ligand binding. Fluorescence experiments were carried out to examine rifampin-induced conformational changes in ARR-2 and ARRs. As protein samples were titrated with increasing volumes of rifampin, a decrease in fluorescence was observed in emission spectra that should indicate a change in enzyme conformation resulting in Trp residues becoming buried within the enzyme thus emitting less of a fluorescence signal. The absorbance of rifampin at 340 nm however interferes with Trp emission and therefore it is uncertain whether changes observed in Trp fluorescence are due to structural changes in the enzyme or due to fluorescence quenching properties of rifampin.

Incubation of ARR-2 and ARRm with trypsin in the presence and absence of rifampin and NAD^+ showed similar patterns of digestion for bound and free enzyme, showing that

substrate binding is unable to protect against proteolytic digestion. This data suggests the presence of a loop region within the ARR enzymes susceptible to proteolysis that is structurally unchanged upon substrate binding. Activity of digested ARR-2 and ARRm was assessed to determine if cleavage occurred in a tail region of the enzyme separate from the active site and not required for catalysis. Trypsin digested ARR-2 and ARRm were inactive indicating the loop region may join two catalytically important parts of the enzyme.

To investigate the binding interactions between ARR-2 and rifampin and NAD^+ further, ^{15}N-^1H heteronuclear correlation experiments were employed. Comparison of spectra collected with native ARR-2 to ARR-2 in complex with each substrate and the reaction product, ADP-ribosyl rifampin, showed significant changes to the conformation of the enzyme upon binding each of these ligands (Figure 2-12). Among the spectra collected for ARR-2 in complex with substrate and product, each showed the enzyme in a unique conformation. The changes in ^{15}N and ^1H chemical shift dispersion observed in the spectra shown in Figure 2-12 illustrate alterations in enzyme flexibility upon binding of product and substrate to the enzyme; the enzyme appears to become less flexible and more structured. NMR data show that the enzyme is able to bind both rifampin and NAD^+ individually and does so in a unique conformation characteristic of the interaction between the enzyme and the substrate. As ADP-ribosyl rifampin is produced, the enzyme takes on yet another conformation different from those observed when bound to rifampin or NAD^+.

ITC experiments were used to examine more closely the binding interactions between the ARR enzymes and rifampin and NAD^+. Titrations of ARRm and ARR-2, with rifampin produced data that was easily fit to model binding curves characteristic of one binding site on the enzyme for the substrate (Figures 2-13 and 2-14 respectively). ITC data showed that rifampin

bound easily to each of the enzymes even at low concentrations (0.2 mM rifampin was used for titration of ARRm). Binding constants were calculated to be 2.83 μM and 0.48 μM for ARRm and ARR-2 respectively. Titrations of ARRm and ARR-2 with NAD^+, however did not produce straightforward results. Despite the use of a variety of combinations of substrate and enzyme concentrations no titration was observed for NAD^+ into ARRm (Figure 2-15). Titration of NAD^+ into ARR-2 however did produce titration data (Figure 2-16), although data could not be successfully fit to a binding curve modeled around one or two unique binding sites for the substrate on the enzyme. The K_d values observed for rifampin demonstrate a high affinity of ARR for this substrate. Results for titrations of ARR with NAD^+ suggested that NAD^+ may be pre-bound to ARR during purification and that is why a titration cannot be observed. The peak shift observed by ^{15}N-^1H NMR in the presence of NAD^+ however confirms that NAD^+ is not likely bound already and that binding can be detected. These results indicate that ITC is a poor method for measuring NAD+ binding constants. Table 2-6 summarizes the results of ligand binding studies with the ARR enzyme.

Table 2-6. Summary of ARR Ligand Binding Studies.

	Rifampin	NAD^+	Prediction
CD Spectroscopy	Conformational change	No observable change in conformation	NAD^+ may be unable to bind ARR in the absence of rifampin
Proteolysis	No change in digestion pattern from free ARR	No change in digestion pattern from free ARR	Binding of rifampin and NAD^+ is unable to protect against proteolytic digestion
	* tryspin digested ARR was inactive as shown by HPLC analysis		
^{15}N-^{1}H NMR	Conformational change	Conformational change	Both NAD^+ and rifampin bind ARR
ITC	Titration observed and fit to a model for one binding site	Titration data could not be fit to a binding curve	

Chromosomally and Tn-encoded rifampin ADP-ribosyl transferase enzymes exhibit indistinguishable, substrate specific steady state kinetics. Circular dichroism spectroscopy, ITC and NMR data suggest that the rifampin ADP-ribosyl transferase enzyme exists in a dynamic and flexible conformation that is easily altered upon interaction with rifampin and NAD^+. While CD spectroscopy originally suggested that NAD^+ may be unable to bind ARR in the absence of rifampin, NMR data confirmed that each substrate was able to bind the absence of one another. ITC was employed to provide further insight into binding interactions between ARR and its substrates, showing that in the absence of NAD^+, ARR has a high affinity for rifampin binding. This technique however was not appropriate for measuring the K_d of ARR for NAD^+. Perhaps there is a preferred order of substrate binding to the ARR enzyme stabilizing its structure and allowing the inactivation reaction to proceed. This type of interaction resembles the induced fit model of enzyme-substrate binding and catalysis, but cannot be determined conclusively based on current data.

Determination of the steady state kinetic mechanism would provide further insight into the mechanism if rifampin inactivation by ARR and aid in understanding binding interactions between ARR and NAD^+ and rifampin. While this work was being completed, the structure of the ARRm enzyme in complex with rifampin was solved, offering valuable information regarding rifampin and NAD^+ binding.

3.0 Chapter 3 – Crystallization of ARRm in Complex with Rifampin and Examination of Substrate Binding Site

3.1 Introduction

The characterization and comparison of ARR enzymes from *M. smegmatis*, *S. coelicolor* and the Tn-encoded ARR-2 have shown that within the class of rifampin ADP-ribosyl transferase enzymes, comparable substrate specific steady state kinetic features and substrate-induced conformational changes are observed. These findings suggest that ARR enzymes may demonstrate a preferred order of substrate binding and may act according to an induced fit model of catalysis. To understand further how the ARR enzyme interacts with rifampin, the three-dimensional crystal structure of ARR from *M. smegmatis* was solved in complex with rifampin. Comparisons of this structure with ADP-ribosyl transferases of other classes has allowed for the prediction of the NAD^+ binding site of ARRm. This structure shows a conserved NAD^+ binding fold and a unique rifampin binding pocket. Examination of the active site of ARRm has allowed for the prediction of potential active site residues, providing further insight into the mechanism of action of the ARR enzyme. An S_N1 type reaction has been predicted for ARR enzymes based on the three-dimensional structure of ARRm in complex with rifampin, and an NAD^+ binding site inferred by comparison with other ADP-ribosyl transferases. This chapter describes the crystallization of ARRm in complex with rifampin and examination of possible active site residues by site-directed mutagenesis.

3.2 Materials and Methods

3.2.1 General Crystallization Set Up

Polyethylene glycol (PEG) 8000 used in crystallization was purchased from Calbiochem, VWR (Mississauga, ON), $MgCl_2$ was obtained from BioShop Canada, Ltd. (Burlington, ON), and 2-methyl-2, 4-pentanediol (MPD) and rifampin were purchased from Sigma-Aldrich Chemical Co. (St. Louis, MO). EasyXtal 24-well plates and Nextal crystallization tools were purchased from Qiagen (Qiagen Inc., Mississauga, ON), VDX 24-well and siliconized cover slides were obtained from Hampton Research (Laguna Niguel, CA) and high vacuum grease was purchased from Corning, VWR (Mississauga, ON). The crystallization trial kits Wizard I and Wizard II were acquired from Emerald Biostructures, DeCode Genetics (BainBridge Island, WA), Crystal Magic was obtained from Biogenova (Toronto, ON). The crystallization screens Crystal Screen, Crystal Screen II, Additives Screen I, II, and III, and Detergents Screen I, II, and III were purchased from Hampton Research (Laguna Niguel, CA).

Purification of ARRm was carried out in a two-step process described in section 2.2.3.1. Protein samples were analyzed by 15 % SDS-PAGE to assess purity and pooled accordingly. The pooled fractions were applied to a HiPrep 26/10 Desalting column equilibrated in 20 mM HEPES pH 7.5 at a flow rate of 8.0 mL/min for buffer exchange. The protein was then concentrated to 10 mg/mL using a 10, 000 MWCO Amicon ultra-15 centrifuge filter and stored at 4°C. The protein sample was centrifuged to pellet large particles and/or precipitate that could impede crystallization. Rifampin was added to a concentration of 1 mM prior to drop set-up.

3.2.1.1 Hanging Drop Method of Crystallization

Protein-substrate crystals grown using the standard hanging drop/vapour diffusion method were done so in EasyXtal 24-well plates sealed with the Nextal crystallization tool. Drop size was varied from 2-4 μL in different ratios of protein to precipitant solution mixed on a siliconized cap and inverted over reservoirs containing 800 μL of varying concentrations of ammonium sulfate. Initial screens using commercially available kits, Wizard I, Wizard II, Crystal Magic, Crystal Screen and Crystal Screen II, were done using 1 μL of protein mixed with 1 μL of kit solution. Kits contained 48 solutions each and all drops were prepared in duplicate. Crystal trays were incubated at 20°C in thermostable incubators or at 4°C.

3.2.1.2 Sitting Drop Method of Crystallization

Protein-substrate crystals grown using the standard sitting drop/vapour diffusion method were done using VDX 24-well plates with siliconized cover slides sealed with high vacuum grease. Drop size was varied from 12-100 μL, prepared on microbridges that were inserted into reservoirs containing 0.8-50 mL of varying concentrations of ammonium sulfate. The sitting drop method of crystallization was used for optimization of crystal size and condition once suitable growth conditions had been established using the commercially available kits.

3.2.2 Crystal Optimization – Fine Screening Technique

Fine screening optimization was carried out on the crystallization conditions that resulted in nucleation or crystal growth in the initial screen using the crystal screening kits. The fine screening technique was employed to improve crystal size and quality by altering several significant crystallization variables. These variables include pH of the buffer [57], concentration

of precipitant, salt concentration, and temperature [58]. Optimization of ARRm included screening different buffers at concentrations ± 50 mM, as well as at different pH values which were monitored from 0.8 pH units below to 1.6 pH units above the pH in the original kit solution. Precipitant concentrations were screened ± 5 % and ± 10 % for polyethylene glycol (PEG) 8000 and 2-methyl-2, 4-pentanediol (MPD) respectively. During the fine screening process, the addition of different salts, protein concentration, and ratio of protein to crystallization solution within the drop were also examined for effects on crystal growth. Crystal trays were incubated at 20°C in thermostable incubators and at 4°C in the attempt to decrease heavy precipitation and improve crystal quality.

3.2.3 Crystal Optimization – Additives and Detergents

The supplementation of additives and detergents was also employed for further optimization of the size and quality of ARRm crystals. Optimization using additives and detergents was carried out in combination with the crystallization conditions previously optimized using the fine screening technique. The additives screen consists of a series of small molecules including ions, salts, and low molecular weight PEGs that improve crystal growth by helping to stabilize the protein and enhance crystal contacts and protein-solvent interactions. The detergents screen is used to influence protein solubility. Additives and detergents were added to a final concentration of 10 % in the drop. Additive Screening kits I, II, and III, and Detergent Screening kits I, II, and III from Hampton Research were used for optimization of crystals.

3.2.4 Data Collection and Processing

Since there is no previously solved rifampin ADP-ribosyl transferase structure available for molecular replacement, selenomethionine-derived ARRm crystals were prepared. Data were collected for a native ARRm crystal and for a selenomethionine-derived crystal. Both data sets were used to solve the structure of the ARRm protein. Selenium atoms incorporated into the protein crystal were used to obtain phase information required for model building, while the native data set was used for model refinement. All data sets were collected at the National Synchrotron Light Source (NSLS). Native crystal data was collected at beamline X8C using an ADSC Quantum-4 CCD detector. Multiple wavelength Anomalous Dispersion data (MAD) data was collected at beamline X25 using an ADSC Quantum-315 CCD detector. MAD data collection involves measuring diffraction data at multiple wavelengths and using the anomalous signal to gain phase information. The software CBASS, which acts as the beamline and experimental control system was used to manipulate data collection steps. Crystals were mounted and flash frozen in a stream of liquid nitrogen at 100 K. Crystals were kept frozen in a continuous stream of liquid nitrogen using a CryoJet. Native and MAD diffraction data were collected at 100 K. Each image for the native crystal was exposed for 60 sec with a 0.5° oscillation, and images for the selenomethionine-derived crystal were each exposed for 5 sec with a 1° oscillation per image. Following collection of diffraction images, the patterns were indexed to identify space groups and unit cell dimensions using HKL2000. Following refinement of unit cell parameters, the reflections on each diffraction image were integrated to create a list of all the reflections measured. These reflections were scaled and averaged together to produce a final reflection list. Data processing was carried out using the same computer software and programs for both the native and selenomethionine-derived ARRm crystals.

3.2.5 Site-Directed Mutagenesis of ARRm

To study structure-function relationships in the ARRm protein, H19A, Y49A, and D84A mutants were prepared. Site-specific mutations were introduced into the *arr* gene sequence from *M. smegmatis* using the QuickChange Site-Directed Mutagenesis Kit (Stratagene, La Jolla, CA) following the protocol of the manufacturer. Using the pET22b (+) vector carrying the *arr* gene as a template, PCR was used to introduce and amplify the selected mutation in the gene. Primers were designed as outlined in the QuickChange protocol to have melting temperatures greater than 78°C (Table 3-1). Reactions were prepared using 10 x reaction buffer containing 100 mM KCl, 100 mM $(NH_4)_2SO_4$, 200 mM Tris HCl pH 8.8, 20 mM $MgSO_4$, 1 % Triton® X-100, and 1 mg/mL nuclease free bovine serum albumin (BSA) (Stratagene, La Jolla, CA), mixed with pET22b (+) DNA containing *arr,* and primers at a final concentration of 1.6 μM, synthesized at the MOBIX Central facility at McMaster University (Hamilton, ON). Reactions were incubated 1 minute at 95°C prior to the addition of 2.5 units of PfuTurbo DNA polymerase. The PCR program used for mutagenesis was designed to have 18 cycles of the following: 95°C for 1 minute, annealing at 55°C for 1 minute, and elongation at 68°C for 12 minutes. At the end of 18 cycles the reactions were held at 68°C for 20 minutes, the temperature was then lowered and held at 16°C. The pET22b (+) vectors carrying the amplified genes for the *arr* mutants were used to transform *E. coli* BL21 (DE3) cells. Mutants were confirmed by DNA sequencing at the MOBIX Central facility at McMaster University (Hamilton, ON).

Table 3-1. Primers used for site-directed mutagenesis of ARRm. Codons targeted for mutagenesis are shown in bold.

Mutant	Primer (5'→3')
H19A	Forward 5'-CTATCTG**CAG**GGCACCAAGGCCGAACTCAAGGTGGGGGAC-3' Reverse Complement 5'-GTCCCCCACCTTGAGTTCGGCCTTGGTGCC**CTG**CAGATAG-3'
Y49A	Forward 5'-GGCGCATCATGAATCACATC**GCC**ATCACCCAG-3' Reverse Complement 5'-CTGGGTGAT**GGC**GATGTGATTCATGATGCGCC-3'
D84A	Forward 5'-GAGGGCGCGATCGAAGAC**GCC**CCGAACGTCACCGACAAGAAG-3' Reverse Complement 5'-CTTCTTGTCGGTGACGTTCGG**GGC**GTCTTCGATCGCGCCCTC-3'

3.2.6 Purification of Site-Directed Mutants and Steady-State Kinetic Analysis

Single colonies of *E. coli* BL21 (DE3) cells carrying pET22b (+) expression vectors with the desired mutations were inoculated into 25 mL of LB supplemented with ampicillin and incubated overnight at 37°C at 250 rpm. From these cultures, 10 mL aliquots were used to inoculate 1L of LB plus ampicillin. Cultures were incubated at 37°C and 250 rpm and grown to an OD_{600nm} of ~ 0.6 where they were induced by the addition of IPTG to a final concentration of 1 mM. Cultures were induced for 20 hours at 16°C.

Cells were harvested by centrifugation at 6, 000 rpm for 10 min, then resuspended in 20 mL lysis buffer consisting of 50 mM HEPES pH 7.5, 1 mM EDTA, and 1 mM PMSF, and passed three times through a French Press at 20, 000 psi to lyse the cells. Following cell lysis, centrifugation at 15, 000 rpm for 20 min was used to remove cell debris.

Purification of the ARRm mutants was carried out in two steps. Cell lysate was applied directly to a 20 mL HiPrep Q Sepharose Column (Pharmacia, Piscataway, NJ) at a flow rate of 1.0 mL/min. The protein eluted at approximately 10 % buffer B using a linear gradient (Buffer conditions are described in Table 2-3). Fractions containing the ARRm protein, as shown by

analysis using 15 % SDS-PAGE, were pooled and concentrated to approximately 20 mL using 10, 000 MWCO Amicon ultra-15 centrifugation filters from Millipore (Etobioke, ON). The second step of the purification was done using a 1 mL HR 5/5 Phenyl Superose Hydrophobic Interaction Column (Pharmacia, Piscataway, NJ). The pooled sample was equilibrated with 1.25 M ammonium sulfate and applied to the column, pre-equilibrated with 1.25 M ammonium sulfate, at a flow rate of 0.5 mL/min. The protein was eluted at approximately 50 % buffer B using a linear gradient (Buffer conditions are described in Table 2-3). Fractions containing protein were analyzed using 15 % SDS-PAGE, pooled, and dialyzed overnight in 50 mM HEPES pH 7.5 at 4°C and stored at -20°C in 40 % glycerol.

Enzymatic activity of the H19A, Y49A, and D84A mutants was analyzed using the discontinuous reverse phase HPLC assay employed for determination of steady-state kinetics of the wild type ARR enzymes. Using a DIONEX C18 column equilibrated in 0.05 % Trifluoroacetic acid (TFA) (v/v) (Solvent A), products were eluted using a linear gradient in acetonitrile/0.05 % TFA (v/v) (Solvent B) at a flow rate of 1.0 mL/min. The initial rate range for the reaction between wild type ARRm and rifampin and NAD^+ had previously been determined to be 5 min. To ensure that the initial rate of each of the mutants occurs within the first 5 minutes of the reaction, activity of each of the mutants was assessed at 2, 5, 10 and 45 min. Reactions were prepared in 100 µL of 50 mM HEPES pH 7.5, 1 nmole enzyme, and 0.5 mM of rifampin and NAD^+. Reactions were incubated 0, 2, 5, 10, and 45 min, and stopped by the addition of methanol to 50 % (v/v). Product formation was analyzed by reverse phase HPLC according to the following method: 0-1 min, 5 % solvent B; 1-11 min, linear gradient up to 97 % solvent B; 11-12.5 min, 5 % solvent B; 12.5-14.5 min, 5 % solvent B (Solvent A: 0.05 % TFA

(v/v); Solvent B: acetonitrile/0.05 % TFA (v/v)) to ensure that each mutant remained in the initial rate range of the reaction.

Once this had been established, steady-state kinetic parameters for rifampin and NAD^+ were determined for ARRm mutants, H19A by varying substrate at six concentrations from 0.05 – 2.0 mM. Reactions were prepared in 100 µL of 50 mM HEPES pH 7.5, 1 nmole mutant ARR, 0.5 mM NAD^+, and varied rifampin concentrations to determine steady state kinetics for rifampin, as well as in 100 µL of 50 mM HEPES pH 7.5, 1 nmole H19A, 0.5 mM rifampin, and varied concentrations of NAD^+ to determine steady state kinetics for NAD^+. All reactions were set up in duplicate. Reaction mixes were incubated five minutes, stopped by the addition of methanol to 50% (v/v), and analyzed by HPLC for product formation using the gradient and solvent system described above. The area under the curve (AUC) of the product shown on the HPLC chromatogram was used to determine the initial rate of reaction at each substrate concentration. A calculated conversion factor was used to convert the product AUC into units of molarity as described in section 2.2.4.2. Data were fit to Equation 1 for Michaelis-Menten kinetics using the computer software GraFit (reference GraFit) and compared to results for wild type ARRm.

3.2.7 MIC Determinations of Site Mutants

The rifampin MIC was determined for ARRm and the H19A, Y49A, and D84A mutants by broth dilution in Mueller-Hinton broth (MHB). Colonies of *E. coli* BL21 (DE3) cells were picked from fresh overnight plates and mixed with 0.85 % saline to an OD_{625nm} of 0.08 – 0.1. Aliquots of 100 µL of the saline solution were mixed into 18.9 mL of MHB. Following this, 95 µL of the mixture was added to each well of a sterile 96-well microtitre plate containing serial

dilutions of rifampin at concentrations ranging from 512 to 0 μg/mL. Each well contained 5 μL of rifampin dilution. The plate was incubated overnight at 37°C and assessed for bacterial growth.

3.3 Results

3.3.1 Crystal Structure of ARRm

Native crystals and crystals of selenomethionine-derived ARRm complexed with rifampin were grown in 50 mM Tris pH 8.2, PEG 8, 000 5% (w/v), MPD 30% (v/v) and 5 mM $MgCl_2$ in a ratio of protein : crystallization solution of 1 : 2 over a reservoir of 1.8 M ammonium sulfate. Trays were incubated at 20°C. Rifampin was added fresh to protein samples to a final concentration of 1 mM. From the additive screen the dipeptide glycylglycine was observed to significantly improve the quality of ARRm crystals. Glycylglycine was added to each drop to a final concentration of 10%. Addition of glycylglycine likely helped to stabilize ARRm, thus improving crystal quality. Crystals were taken to NSLS by Dr. Murray Junop for data collection.

The crystallographic data obtained from native and selenomethionine-derived crystals of ARRm in complex with rifampin were processed using HKL2000 software. For each crystal, the C2 space group was chosen. The software CNS was used to obtain phase information from the MAD data set, and CCP4 was used for model refinement. The ARRm structure was solved using Single Anomalous Diffraction, which uses phase information gained from diffraction data collected at the peak wavelength. Refinement of the structure was completed using data collected from the native crystal to 1.45 Å using the computer program refmac version 8.0 of the CCP4 software. Iterative cycles of manual model building were done using wincoot and refmac. Table 3-2 summarizes the crystallographic data collected and refinement statistics.

The final model refinement gave an R value of 13.4 % and an R_{free} value of 18.5 %. The complete data set demonstrated an average redundancy of 4.5 (Total number of reflections/Number of unique reflections) with a signal to noise ratio of 20.6 and an R_{merge}[c] value

of 5.8 % ($R_{merge}^{c} = \Sigma \mid I_{obs} - I_{avg} \mid / \Sigma I_{avg}$). The refined unit cell dimensions for ARRm were a = 55.7 Å, b = 61.0 Å, c = 45.6 Å, with angles of $\alpha = \gamma = 90°$, and $\beta = 91.8°$ as listed in Table 3-2.

A stereo diagram of the structure of the *M. smegmatis* rifampin ADP-ribosyl transferase enzyme in complex with rifampin is shown if Figure 3-1. This structure consists primarily of unstructured loop regions linked by helices 1 and 2, and beta strands 1 through 7 (Figure 3-1). Rifampin binding occurs in an active site pocket consisting of H1 and H2 and a loop region formed between β5 and β6 that extends upward, wrapping around rifampin (Figure 3-1). The dipeptide additive glycylglycine is bound alongside rifampin in the active site of ARRm (Figure 3-1).

Table 3-2. Crystallographic data and refinement statistics for *M. smegmatis* ARR in complex with the substrate rifampin.

Data Collection		
Derivative	SelenoMethionine	Native
Wavelength (Å)	0.9794	1.100
Space group	C2	C2
Unit-cell parameters (Å)	a = 55.0, b= 61.0 and c = 45.8 $\alpha = \gamma = 90, \beta = 92.6$	a = 55.7, b= 61.0 and c = 45.6 $\alpha = \gamma = 90, \beta = 91.8$
No. of molecules in asymmetric unit	1	1
Resolution range (Å)[a]	25.0 – 1.65 (1.71 – 1.65)	50.0 – 1.45 (1.50 – 1.45)
Unique reflections	18,271	26,649
Data Redundancy[a]	7.6 (7.4)	4.5 (4.0)
Completeness (%)[a]	100.0 (100.0)	98.0 (95.9)
$I/\sigma(I)$[a]	21.6 (4.0)	20.6 (2.7)
R_{merge} (%)[a]	7.4 (51.4)	5.8 (54.4)
Model and refinement		
Resolution range (Å)[a]		30.18 – 1.45
R_{work} (%)		13.4
R_{free} (%)		18.5
Refl. observed		25,293
Refl. test set		1,342
No. of amino acid residues/atoms		138/1113
Ligand atoms		68
No. of waters		272
r.m.s.d bond lengths (Å)		0.021
r.m.s.d bond angles (°)		2.19
Average *B* factor (Å^2)		29.6

[a]Data for the highest resolution shell are shown in parentheses.

R_{merge}[c] = $\Sigma \mid I_{obs} - I_{avg} \mid / \Sigma I_{avg}$

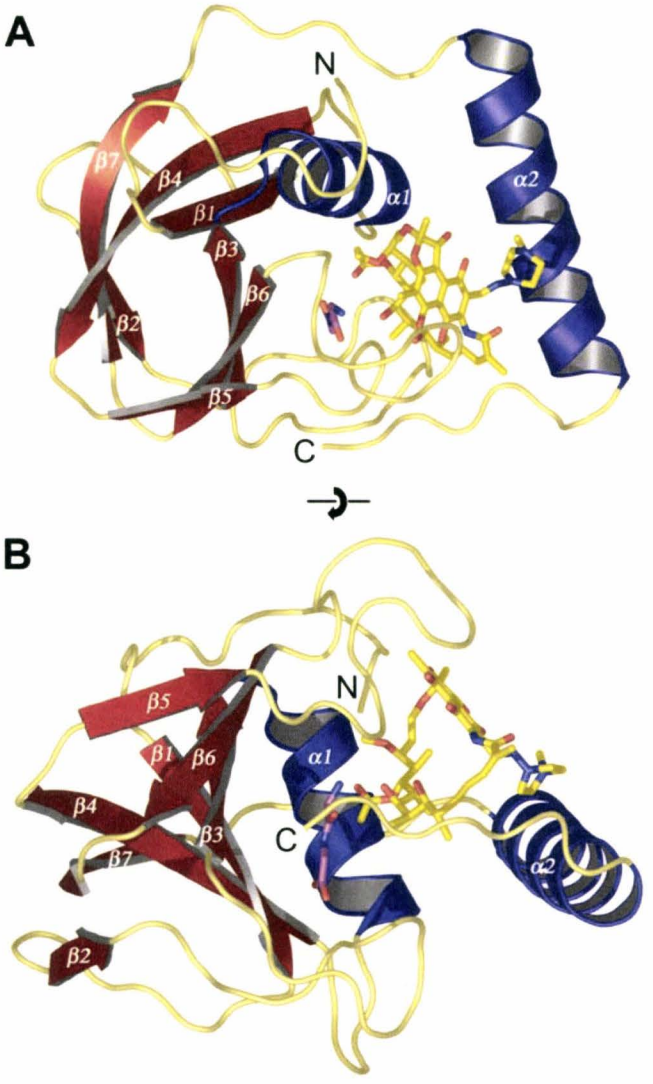

Figure 3-1. Orthagonal view of the three dimensional protein structure of *M. smegmatis* rifampin ADP-ribosyl transferase (ARRm) with bound substrate, rifampin. The tertiary structure of *M. smegmatis* ARR with rifampin bound shows a binding pocket for rifampin (yellow) formed by helices 1 and 2 and the β5-β6 loop. The dipeptide additive glycylglycine is shown in purple. The structure was solved by Single Anomalous Diffraction and refined to 1.45 Å using data collected for the native ARRm crystal.

Using the DALI server at EMBL, a network service for comparing three dimensional protein structures, the structures of two ADP-ribosyl transferase enzymes, the catalytic domain of *P. aeruginosa* exotoxin A domain III (ETA), and a Poly(ADP-ribose) polymerase (PARP), and one probable RNA 2'- phosphotransferase were found to have the same general fold as the structure of ARRm (Figure 3-2). Topological maps of each of these structures are shown in Figure 3-2. The α/β fold identified among these four enzymes includes H1 and β1, β3, β4, β5, β6, and β7 of ARRm, and is conserved among ADP-ribosyl transferases [59-63]. A central cleft is formed at the interface of two anti-parallel β sheets, making up the NAD^+ binding site, and containing conserved catalytic residues including, His19, Gly20, Thr21, and Tyr49 [60-63]. Despite little sequence identity in this region, only approximately 20 %, the NAD^+ binding cleft is conserved among PARP, ETA, diphtheria toxin (DT), cholera-toxin-related heat-labile enterotoxin (LT), pertussis toxin (PT), *Clostridium perfringens* Iota-toxin (Ia), and *Clostridium botulinum* exoenzyme C3 [60-63].

A core alignment of the structures shown in Figure 3-2 with ARRm further illustrates the structural similarity of the NAD^+ binding site among each of the enzymes (Figure 3-3). The structure of ETA domain III was solved in complex with a non-hydrolyzable NAD analogue β-methylene-thiazole-4-carboxamide adenine dinucleotide (β-TAD) showing the predicted position of NAD^+ in the active site [64]. Based on the core alignment it can be inferred that in the ARRm structure beta strands 1 through 7 excluding β2 form a structurally conserved active site cleft on which NAD^+ is bound. The site for NAD^+ binding is tucked under the binding sit for rifampin, implying that NAD^+ likely binds ARR first.

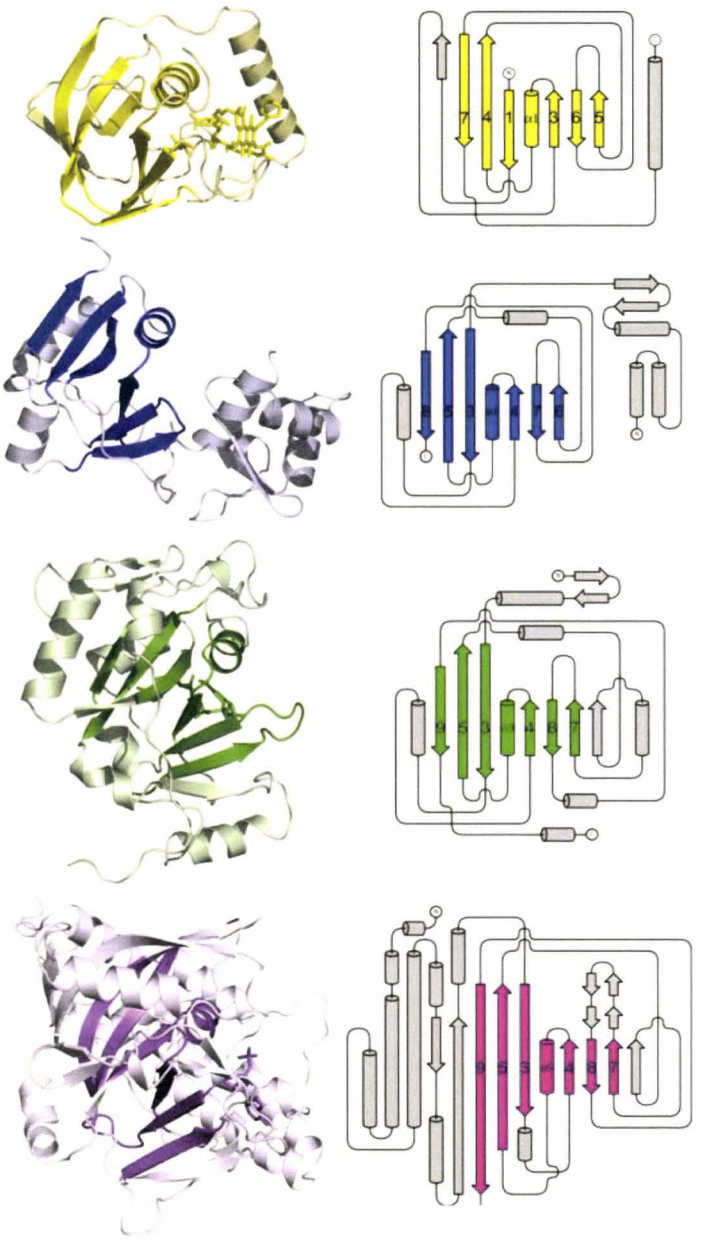

Figure 3-2. Comparison of the three-dimensional structures and general topology of ARRm and structurally similar proteins. The DALI server was used to compare the 3D structure of ARRm (yellow) with previously solved structures. Structures found to have a conserved fold included *P. aeruginosa* domain III (green), Poly(ADP-ribose) polymerase (purple), and a probable 2'-RNA phosphotransferase (blue). PDB accession codes are 1AER, 1A26, and 1WFX respectively.

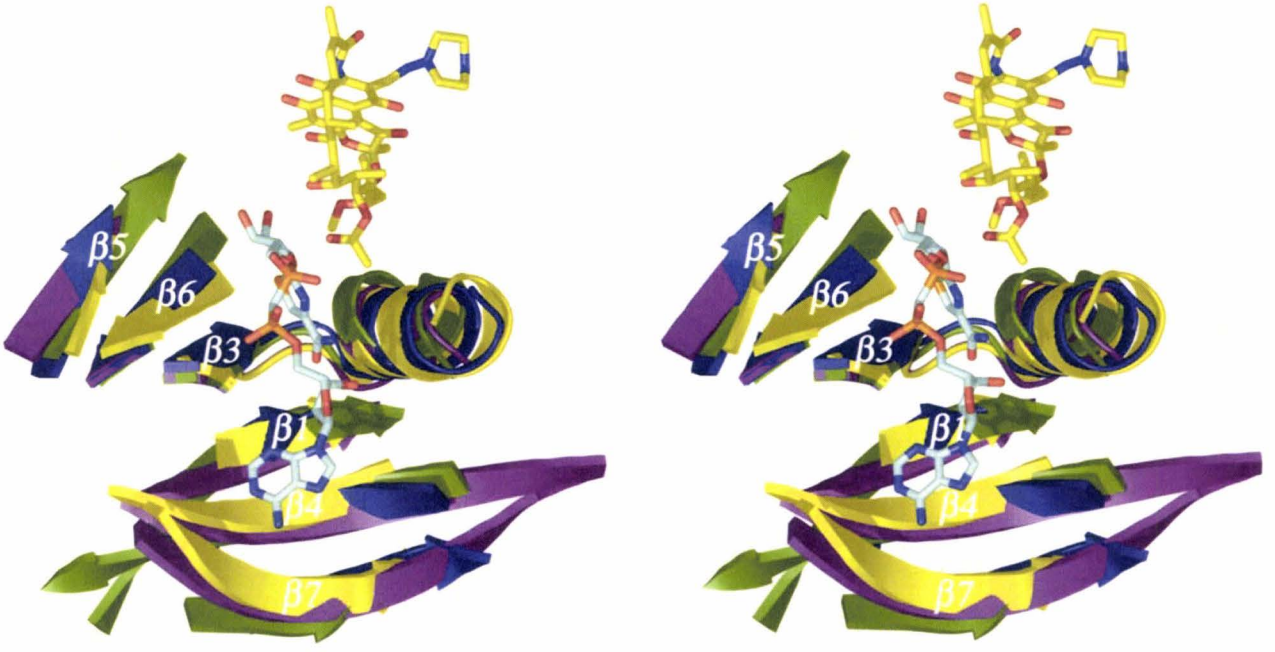

Figure 3-3. Three-dimensional core alignment of the NAD^+ binding cleft conserved among ADP-ribosyl transferase enzymes. The structure of ARRm (yellow) in complex with rifampin is shown aligned with the structurally conserved NAD^+ binding of cleft of *P. aeruginosa* domain III (green), Poly(ADP-ribose) polymerase (purple), and a probable 2'-RNA phosphotransferase (blue) are shown in stereo view. PDB accession codes are 1AER, 1A26, and 1WFX respectively. The structure *P. aeruginosa* domain III was solved in complex with β-TAD shown here in light blue to highlight the NAD^+ binding site.

A structure based alignment of these four structures, as well as other ADP-ribosyl transferases (Figure 3-4), highlights residues conserved among ADP-ribosyl transferase enzymes. Rifampin ADP-ribosyl transferases shown in Figure 3-4 were selected from a BLAST search using the sequence of ARRm. BLAST results are shown in Table 3-3. Residues making direct contact with NAD^+ are found in β1, β2, and β3. His19, Gly20, Thr22, and Tyr49, and are highly conserved among ARRm, ETA and DT; Ser is found in place of Thr22 in PARP. Leu25 is conserved among all rifampin ADP-ribosyl transferases, but is replaced by a highly conserved Ile residue in other ADP-ribosyl transferases. The rifampin binding site on ARRm is unique to the rifampin ADP-ribosyl transferase class of these enzymes. Aside from H1, which makes no direct contacts with NAD^+, it is not found within the structurally conserved region of the protein

shown in Figure 3-3. Residues involved in rifampin binding are found in H1 and H2 and the loop region between β5 and β6. In H1, Trp59, Gly60, and Leu63 are conserved in approximately 70 % of the rifampin ADP-ribosyl transferases shown in Figure 3-4. While rifampin does make contacts with residues in the structurally conserved H1, Figure 3-4 shows a conserved Tyr residue in other ADP-ribosyl transferase structures that aligns with Gly60 in ARRm. This residue is conserved as either Gly or Ala in rifampin ADP-ribosyl transferases (Figure 3-4). The carboxyl group of rifampin is located next to Gly60 in ARRm. The presence of Try in this position would prevent rifampin binding in ARRm and is predicted to exclude rifampin binding in bacterial exotoxins and PARPs that typically bind and ADP-ribosylate protein substrates. Other highly conserved residues involved in rifampin binding include Lys90, Lys91, Pro96, and Thr97, which exist in the β5-β6 loop and Met126 and Leu130 in H2 (Figure 3-4). A conserved Asp residue, Asp84, is found just before the β5-β6 and makes direct contact with NAD^+.

Table 3-3. BLAST search results for Rifampin ADP-ribosyl transferases shown in Figure 3-4.

Organism	E-value	Percent Similarity
Clostridium sp. OhILAs	1e-33	51
Bacillus megatrium	8e-32	53
Vibrio cholerae	5e-36	57
ARR-2	1e-35	57
Burkholderia cenocepacia	2e-28	51
ARRs	4e-27	53

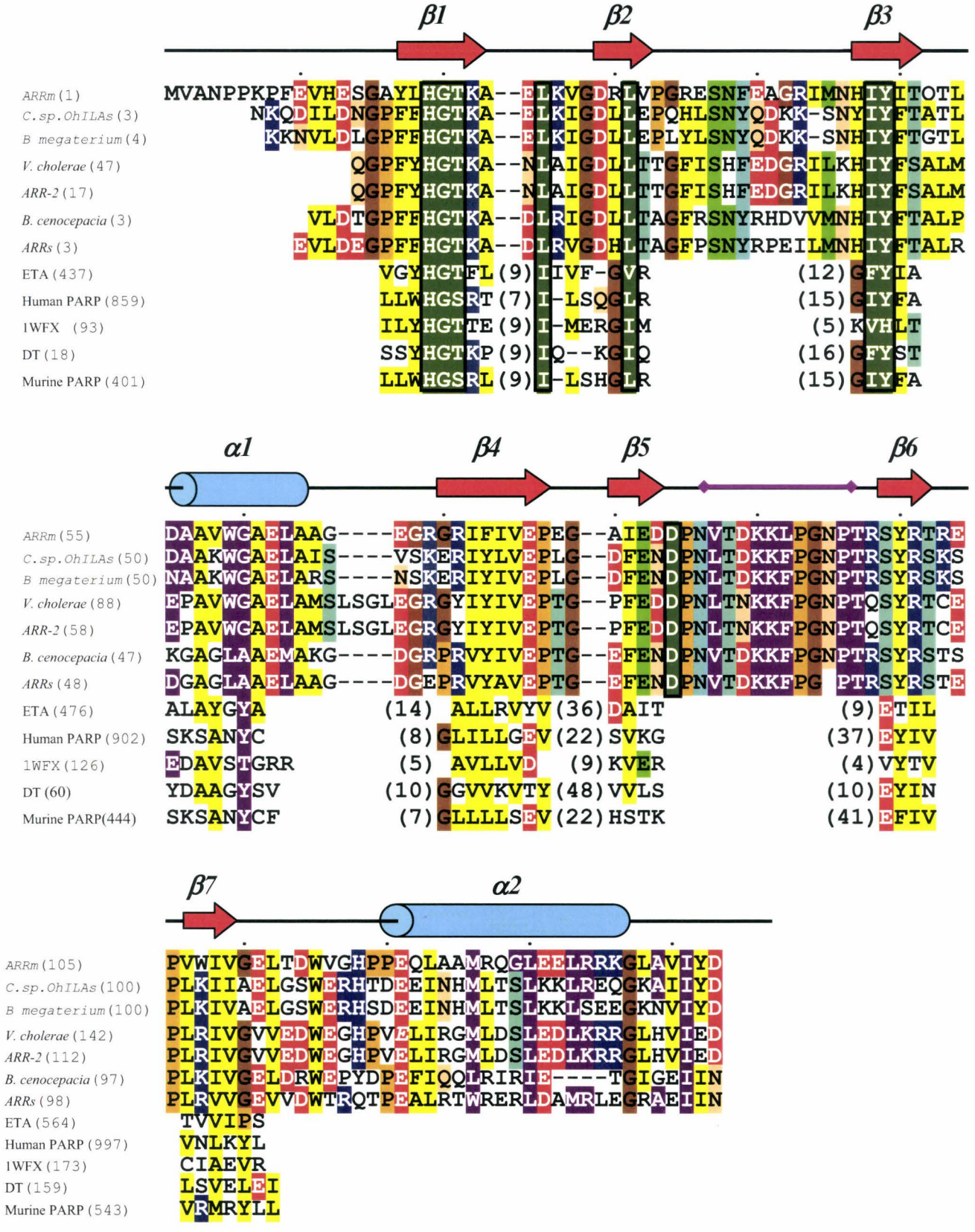
β1
β2
β3
ARRm (1)
C. sp. OhILAs (3)
B megaterium (4)
V. cholerae (47)
ARR-2 (17)
B. cenocepacia (3)
ARRs (3)
ETA (437)
Human PARP (859)
1WFX (93)
DT (18)
Murine PARP (401)
α1
β4
β5
β6
ARRm (55)
C. sp. OhILAs (50)
B megaterium (50)
V. cholerae (88)
ARR-2 (58)
B. cenocepacia (47)
ARRs (48)
ETA (476)
Human PARP (902)
1WFX (126)
DT (60)
Murine PARP(444)
β7
α2
ARRm (105)
C. sp. OhILAs (100)
B megaterium (100)
V. cholerae (142)
ARR-2 (112)
B. cenocepacia (97)
ARRs (98)
ETA (564)
Human PARP (997)
1WFX (173)
DT (159)
Murine PARP (543)

Figure 3-4. Structure based alignment of rifampin ADP-ribosyl transferases, mono ADP-ribosyl transferases, and PARPs. Alignment includes ARR enzymes listed by species name, mono ADP-ribosyl transferases ETA (1AER) and DT (1DTP), the catalytic fragment of human (1A26) and murine (1GS0) PARP, and a probable 2' RNA-phosphtransferase, listed by its PDB id number, 1WFX. PDB id numbers are shown in parenthesis. Conserved residues making contact with NAD^+ are outlined and shown in dark green. Residues making contact with NAD^+ in ARR only are shown in dark green. Residues making contacts with rifampin are shown in purple, and residues contacting both NAD^+ and rifampin are shown in teal blue. Red and blue show negative and positively charged residues respectively; hydrophobic residues are shown in yellow and polar residues in peach. Glycine and proline are shown in brown and orange respectively.

Examination of the residues conserved among all classes of ADP-ribosyl transferases believed to be involved in NAD^+ binding, allowed for the prediction of residues likely to be involved in catalysis. This included His19 and Tyr49, predicted to be involved in NAD^+ binding, and Thr21 and Asp84, which likely play a role in stabilizing the carbocation intermediate formed upon dissociation of the nicotinamide leaving group (Figure 3-5).

The dipeptide additive, glycylglycine is bound to ARRm in the NAD^+ binding site, as predicted by the position of β-TAD in the ETA structure, possibly mimicking NAD^+ binding and stabilizing the structure of ARRm (Figure 3-5).

Figure 3-6 shows a close up view of the orientation of Asp84 and Tyr49 with respect to NAD^+ or glycylglycine and surrounding water molecules in the active site of ARRm.

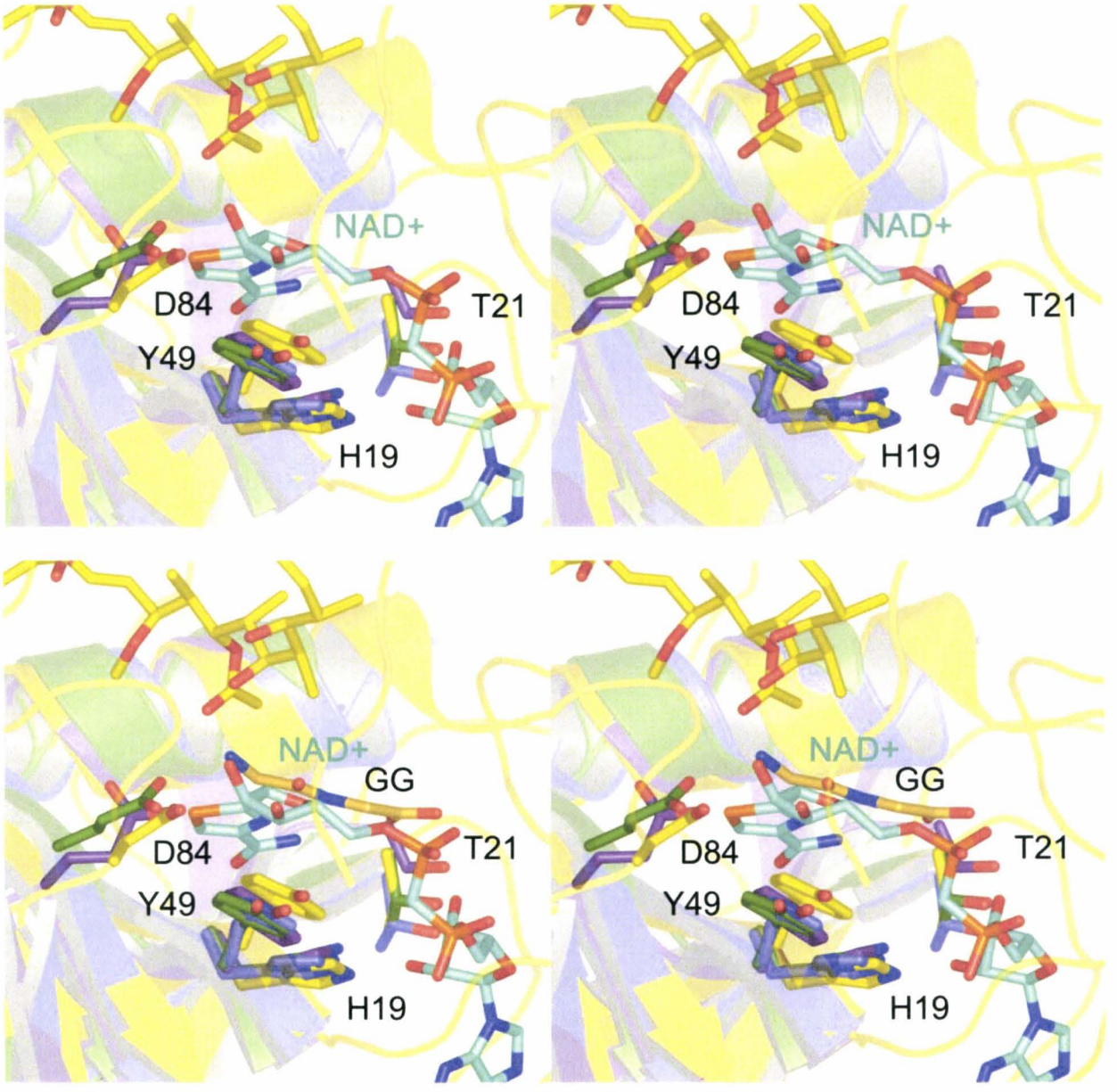

Figure 3-5. Predicted binding of NAD^+ in the active site of ARRm and conserved residues likely to be involved in binding and catalysis. Stereo views of the NAD^+ binding cleft and the residues conserved between ARRm (yellow), ETA (green), and PARP (purple) that are believed to be involved in NAD^+ binding and catalysis. Positioning of NAD^+ with respect to highlighted residues is based on the structure of ETA in complex with β-TAD. The bottom panel shows the position of the dipeptide additive glycylglycine with respect to NAD^+ in the active site.

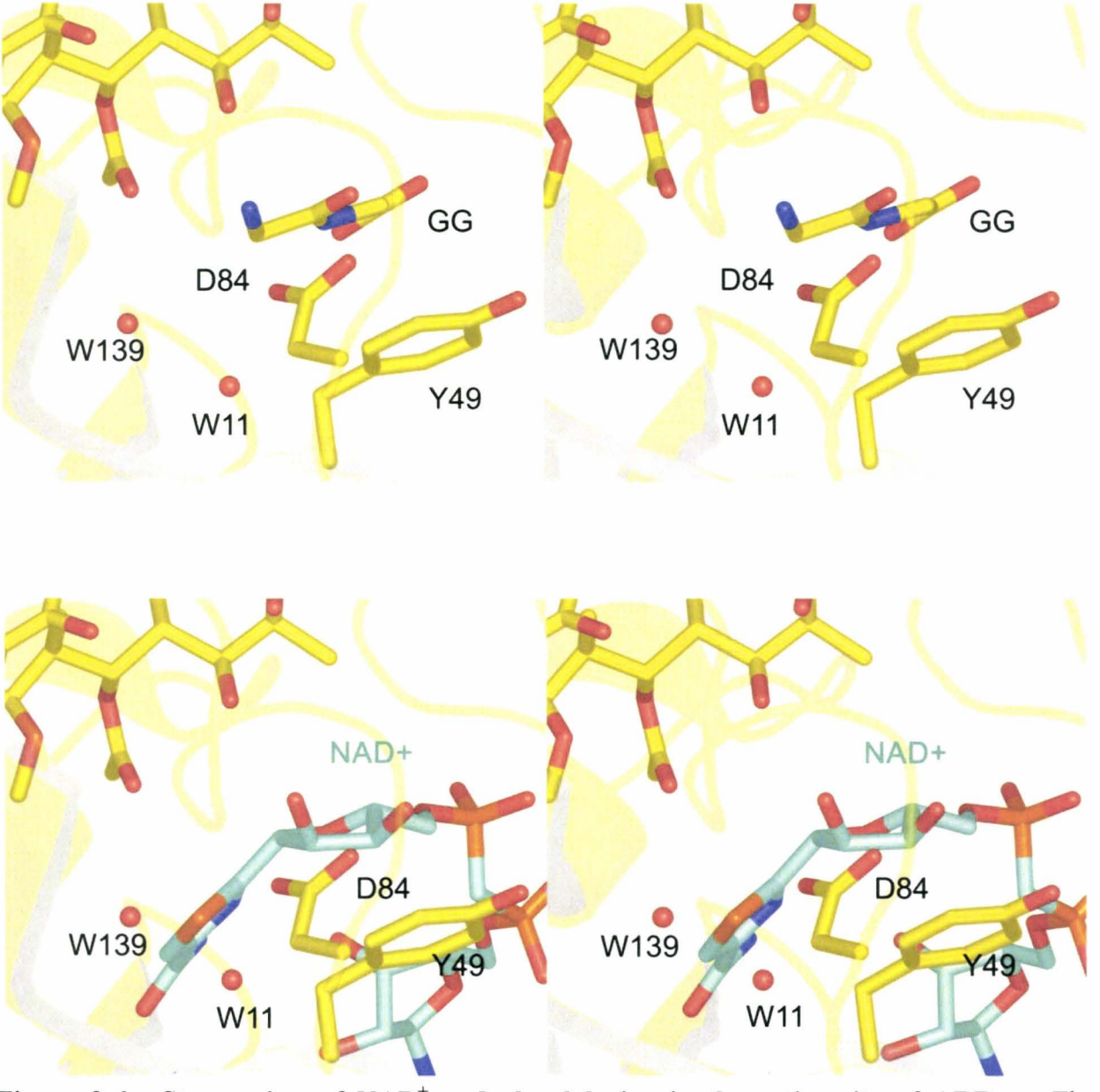

Figure 3-6. Stereo view of NAD^+ and glycylglycine in the active site of ARRm. The dipeptide additive glycylglycine in the active site of ARRm and the positioning of Asp84, Tyr49, and active site water molecules is shown in the top panel. The position of NAD^+ in the active site of ARRm, predicted based on the structure of ETA with β-TAD, is shown in the bottom panel. The position of Asp84, predicted to stabilize the carbocation intermediate formed upon dissociation of nicotinamide from NAD^+, Tyr49, and active site water molecules with respect to NAD^+ is shown.

Figure 3-7 shows an $|F_{obs}| - |F_{calc}|$ map, contoured to 3 σ, of rifampin and glycylglycine in the active site of ARRm. The secondary structural elements making up the rifampin binding pocket, H1, H2, and the β5-β6 loop are shown in Figure 3-7A. The position of glycylglycine in the active site of ARRm likely mimics the binding site for NAD^+ (Figure 3-5). Glycylglycine is bound next to the 23-OH of rifampin, where the ADP-ribose moiety from NAD^+ is attached (Figure 3-7B).

Residues making contact with rifampin, shown in purple in Figure 3-4, are located within H1, H2, and the β5-β6 loop region of ARRm. These residues are highly conserved among rifampin ADP-ribosyl transferases, but absent in other classes, illustrating the unique rifampin binding site in this particular class of ADP-ribosyl transferase enzymes (Figure 3-4). The arrangement of these residues with respect to rifampin in its binding pocket is shown in Figure 3-8. Excluding Asn86, all residues making direct contacts with rifampin do so through van der Waals interactions. The only direct hydrogen bonding contact made between rifampin and ARRm is through Asn86, which hydrogen bonds with O1 of rifampin. All other hydrogen bonding interactions are with ordered water molecules surrounding rifampin in the active site. Hydrogen bonds are made to O1, O2, O4, O5, O8-O11, and N1 of rifampin holding the molecule in its binding pocket on the enzyme.

The rifampin binding pocket is situated so that NAD^+ binding must likely occur prior to rifampin binding, suggesting ARR operates by an ordered Bi Bi reaction mechanism. This can be confirmed by determination of the steady state kinetic mechanism.

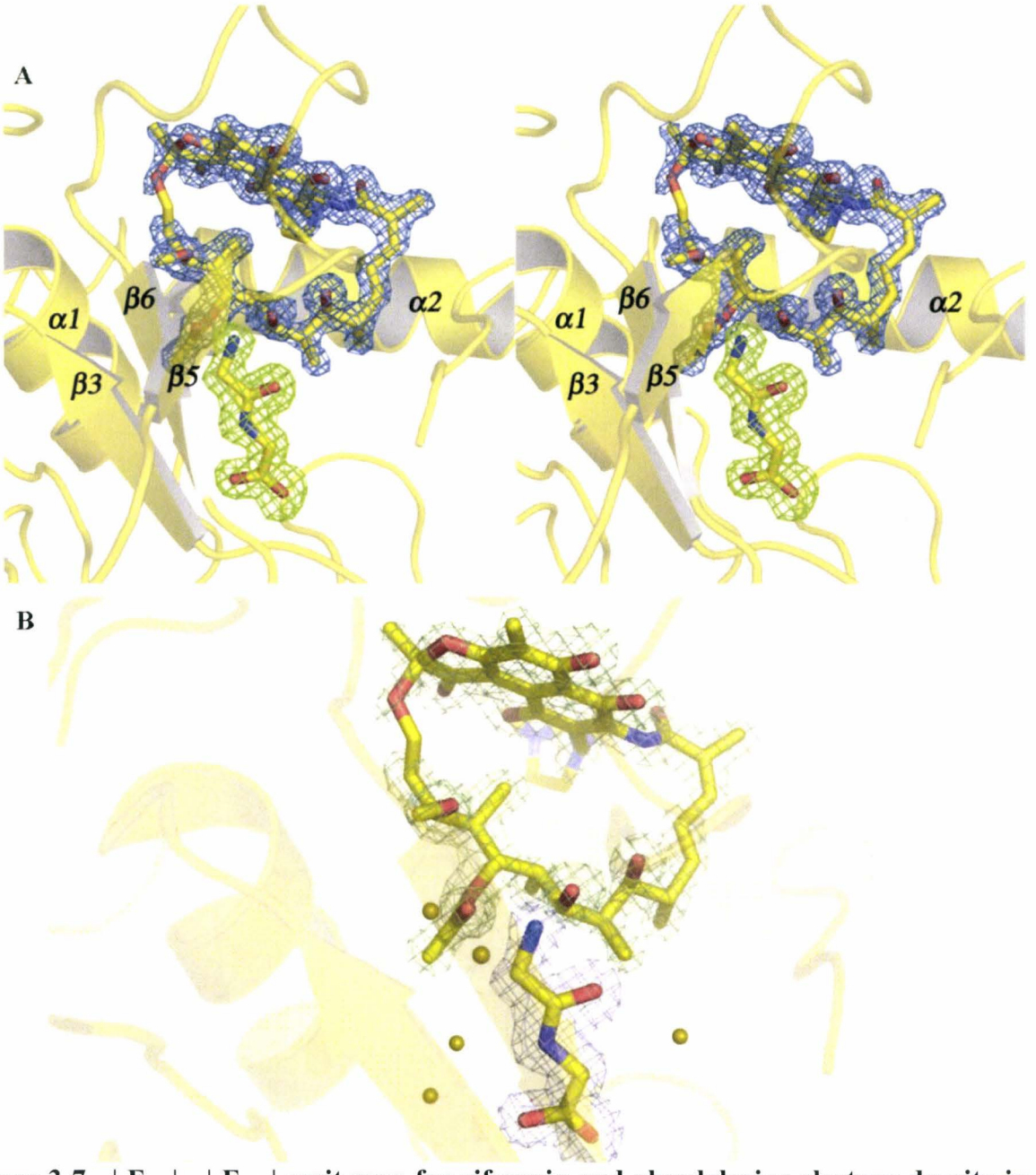

Figure 3-7. $|F_{obs}| - |F_{calc}|$ omit map for rifampin and glycylglycine electron density in the ARRm-rifampin complex. Electron density is shown at 1.45 Å and contoured at 3 σ. A. Stereo view of the electron density of rifampin and glycylglycine in the active site of ARRm. B. A closer view of the interaction of rifampin and glycylglycine. Glycylglycine is oriented next to the 23OH position of rifampin where the ADP-ribose from NAD^+ is added.

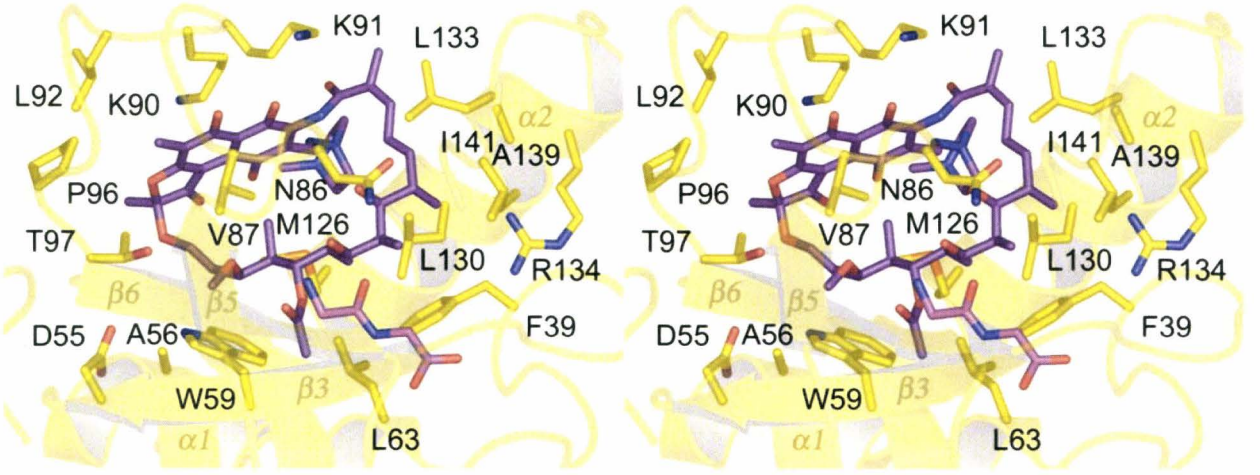

Figure 3-8. Stereo view of residues forming the rifampin binding pocket on ARRm. Rifampin, shown in purple, binds in a pocket on ARRm formed by H1, H2, and the β5-β6 loop region. Side chains making contact with rifampin are conserved among rifampin ADP-ribosyl transferase enzymes and make up a binding site for rifampin unique to this class of enzymes. All contacts made between rifampin and ARRm, with the exception of Asn86, are van der Waals contacts. Asn86 makes the only hydrogen bond contact between rifampin and the enzyme.

3.3.2 Site-Directed Mutagenesis of ARRm

Based on the crystal structure of ARRm His19, Y49, and Asp84 were chosen for site-directed mutagenesis to investigate the catalytic mechanism of the enzyme. The steady-state kinetic parameters for ARRm were determined using a discontinuous reverse phase HPLC assay. This assay was employed to characterize the steady-state kinetic properties for each of the ARRm mutants.

Reactions were prepared for site mutants and monitored for the appearance of product. No product peak was observed on the HPLC chromatogram for reactions with either the Y49A or D84A mutants, indicating that the enzymes were not able to catalyze the inactivation of rifampin. This was confirmed by LC/MS, showing the absence of a product with a mass corresponding to the expected mass of ADP-ribosyl rifampin. HPLC analysis of reactions with H19A showed the production of negligible amounts of inactivated rifampin over a period from 0 to 10 minutes indicating the H19A mutant was also inactive.

MIC values were determined for each of the ARRm mutants as well as for wild type ARRm and pET22b (+) vector without the *arr* gene. Results are summarized in Table 3-4.

Table 3-4. MIC Determinations for ARRm site mutants

	Rifampin MIC (μg/mL)
pET22b (+)	16
ARRm	256
His19Ala	4
Tyr49Ala	4
Asp84Ala	8

MIC's were done induced and un-induced, results were consistent for each.

The MIC values for each of the ARRm mutants are greatly reduced from wild type, confirming the inactivity of each mutant.

3.4 Discussion and Concluding Remarks

The structure of *M. smegmatis* ARR in complex with rifampin is the first in a novel class of ADP-ribosyl transferase enzymes that catalyze the transfer of the ADP-ribose moiety from NAD^+ to a small molecule substrate, rifampin. The structure consists of a large number of loop regions linked by two α-helices and 7 β strands (Figure 3-1) which likely can account for the dynamic behaviour observed in ITC and NMR studies. Binding of substrate to ARR may stabilize the conformation of the enzyme. NMR data suggested that upon interaction with substrate, ARR-2 became less flexible and more ordered. The active site is comprised of two helices (H1 and H2) and a β5-β6 loop region making up the rifampin binding site, and a highly conserved β sheet fold predicted to be involved in NAD^+ binding [50, 60-62, 65]. The presence of this conserved fold was detected using the DALI server, which identified the three dimensional structure of ETA domain III, PARP, and a probable RNA phosphotransferase to have the same general fold as ARRm (Figure 3-2). Comparison of the topological maps of each

of these structures highlights the common fold between ARRm, ETA, PARP and the probable RNA phosphotransferase, as well as illustrates the differences in overall structure. While ETA, PARP, and the probable RNA phosphotransferase each have a number of unconserved structural elements aside from the NAD^+ binding cleft, the structure of ARRm is quite compact and contains only one helix and one β strand outside of the conserved fold. A three dimensional core alignment of these structures with ARRm further illustrates the conservation of the NAD^+ binding cleft, predicted based on the structure of ETA domain III solved in complex with the non-hydrolysable NAD^+ analogue β-TAD [64] (Figure 3-3). This predicted NAD^+ binding cleft of ARRm is also found in a variety of other bacterial ADP-ribosylating exotoxins, including the well characterized PT, DT, and LT, as well as it is conserved across the PARP-superfamily of poly(ADP-ribose) polymerases [49, 59-61].

The binding site for rifampin, formed by H1, H2, and the β5-β6 loop region, is unique to the rifampin ADP-ribosylating class of ADP-ribosyl transferases. The β5-β6 loop structure of ARRm extends up around rifampin holding it in place in the binding pocket blocking the site for NAD^+ binding. Aside from Asn86, no direct hydrogen bonding is observed between ARRm and rifampin. The dipeptide additive glycylglycine is bound adjacent to rifampin in the active site of ARRm predictably mimicking NAD^+ binding and stabilizing the structure of ARRm. The structure of ARRm is concise and compact, forming an active site with a conserved NAD^+ binding cleft and a unique rifampin binding pocket, with little extraneous structure.

Within the NAD^+ binding site, there are several residues highly conserved among bacterial ADP-ribosylating toxins, PARPs, and other rifampin ADP-ribosyl transferases that make direct contacts with NAD^+ (Figure 3-4). These residues are mainly found in β1, β2, and β3. Examination of residues conserved among all classes of ADP-ribosyl transferases identified

residues of ARRm likely to be involved in NAD^+ binding and/or catalysis. Based on the structure based alignment in Figure 3-4, His19, and Try49, were chosen for mutagenesis to examine their roles in the ADP-ribosylation of rifampin. His19 of ARRm aligns with His440 of ETA, His21 of DT, and His35 of PT which have been predicted to be involved in NAD^+ binding by forming hydrogen bonds with the AMP-ribose of NAD^+ [60, 64]. Replacement of His440 in ETA with an Ala residue resulted in a 1000-fold decrease in ADP-ribosyl transferase activity of the enzyme, but had no effect on NAD^+ binding, suggesting this residue may be involved in the transfer of the ADP-ribose moiety to EF-2, the protein substrate of the reaction [66]. Mutagenesis of His19 to Ala in ARRm resulted in very slight activity, as analyzed by HPLC. MIC values for H19A were below that of MIC values for pET22b (+) vector without the *arr* gene, confirming that the enzyme was unable to inactivate rifampin. Based on these results the direct role for His19 in the inactivation of rifampin by ARRm cannot be determined definitively, however the structure suggests that His19 does hydrogen bond with the 2' position of the AMP-ribose.

Tyr49 of ARRm is also highly conserved among all classes of ADP-ribosyl transferases. Substitution of Tyr470 of ETA with Phe caused no significant change to ADP-ribosylation activity verifying that in ETA Tyr470 was not involved in catalysis [67]. Replacement of Tyr49 with Ala in ARRm however resulted in inactivity, confirmed by HPLC analysis and MIC determination, suggesting that for the rifampin ADP-ribosyl transferase this conserved Tyr plays an important role in NAD^+ binding and/or catalysis. Structural evidence demonstrates this Tyr stacks with the nicotinamide ring of NAD^+.

In the structure of ARRm Asp84 is conserved among rifampin ADP-ribosyl transferases, but is absent in other classes of ADP-ribosyl transferases. Asp84 makes direct contacts with

NAD^+, and is located at the end of β5, just before the start of the β5-β6 loop, in the vicinity of a highly conserved Glu residue found in other classes of ADP-ribosyl transferases (Glu553 in ETA, Glu148 in DT, and Glu988 in PARP). The conserved Glu residue is essential for catalysis of ADP-ribosylation reactions in a variety of bacterial ADP-ribosyl transferases and PARP [61-64, 68]. The negative charged carboxylate forms hydrogen bonds to the 2'-hydroxyl of the nicotinamide ribose of NAD^+, stabilizing the predicted oxocarbenium ion intermediate following dissociation of the nicotinamide leaving group in an S_N1 type reaction [61-64]. It has also been proposed that Glu148 of DT and Glu988 of PARP may act to activate the diphthamide residue on EF-2 and the 2'-hydroxyl terminal adenosine group of a nascent poly-ADP ribose chain respectively to carry out a nucleophilic attack on the nicotinamide ribose of NAD^+ in and S_N2 type displacement reaction [61, 68]. Substitution of Asp84 with Ala eliminated ADP-ribosyl transferase activity of ARRm. The position of Asp84 with respect to NAD^+ in the active site of ARRm (Figure 3-5 and 3-6) and the loss of ADP-ribosyl transferase activity of in the presence of a D84A mutation imply that this residue is essential for enzymatic activity of ARRm. Upon dissociation of the nicotinamide leaving group, Asp84 is predicted to hydrogen bond to the nicotinamide ribose of NAD^+ and stabilize the carbocation intermediate of an S_N1 type reaction. Although Asp84 is predicted to have a similar role in catalysis in ARRm as Glu residues in other classes of ADP-ribosyl transferases, the lack of conservation of this residue could be the result of the substrate difference between these classes of ADP-ribosyl transferase enzymes.

Like the unique small molecule substrate of the ARR enzymes, the binding pocket for rifampin on ARRm is unique to this class of rifampin ADP-ribosyl transferase enzymes. The alignment shown in Figure 3-4 highlights residues conserved among ARR enzymes. These residues are located in H1, H2, and the β5-β6 loop region that make up the rifampin binding

pocket and are absent in other classes of ADP-ribosyl transferases. What is interesting is the presence of a conserved Tyr residue in bacterial exotoxins and PARPs that is replaced by a conserved Gly residue in ARR enzymes. Mutation of Tyr481 of ETA to Phe caused a 10-fold reduction in ADP-ribosyltransferase activity and caused no significant changes to the NAD-glycohydrolase activity of the enzyme [67]. This data suggested that Tyr481 was not involved in NAD^+ binding as originally predicted, but likely interacts with the EF-2 substrate [67]. The Gly60 of ARRm and the complementary Tyr481 of ETA are located in H1, the only structural feature of the rifampin binding pocket that is conserved among all classes of ADP-ribosyl transferases (Figure 3-2). The presence of Tyr in this position is predicted to exclude rifampin binding in bacterial exotoxins and PARPs that would typically bind and ADP-ribosylate protein substrates. The existence of a Gly residue in this position of ARRm is a unique structural feature of the rifampin inactivating class of ADP-ribosyl transferases that allows these enzymes to selectively bind and ADP-ribosylate the small molecule rifampin rather than a protein substrate.

The three-dimensional structure of ARRm in complex with rifampin confirms that binding of NAD^+ to ARR likely occurs prior to rifampin binding, and that interaction with substrates may act to stabilize the loopy conformation of ARR enzymes, allowing the inactivation reaction to occur. The structure provides valuable information on reaction mechanism and the specific interactions between ARR and its substrates.

4.0 Conclusions and Prospects for Future Research

4.1 Concluding Remarks and Future Directions

Rifampin ADP-ribosyl transferase enzymes from *M. smegmatis, S. coelicolor*, and a Tn-encoded copy found in a number of Gram negative pathogens have been overexpressed, characterized and compared. Each of the ARR enzymes studied exhibits comparable substrate specific steady state kinetics. Catalytic efficiency for the rifampin ADP-ribosyl transferase enzyme is on the order of 10^3, while reported values for DT and ETA are 10^7 and 10^8 respectively for NAD^+, and 10^4 and 10^5 respectively for eEF-2. This indicates the enzyme may be responsible for an alternate function in the cell, and may have evolved the ability to inactivate rifampin.

Examination of the interactions between ARR and its substrates, rifampin and NAD^+, was completed to gain insights into the mechanism of rifampin inactivation. Circular dichroism spectroscopy data suggested that rifampin binding may be necessary to induce a conformational change in the enzyme required for binding of NAD^+, or that NAD^+ binding did not induce any significant conformational changes to the enzyme. To determine the order of substrate binding and the mechanism of rifampin inactivation by the ARR enzymes, determination of the steady state kinetic mechanism or detailed thermodynamic experiments could be used. To examine the interaction of rifampin with ARR, intrinsic fluorescence of Trp residues was exploited. Changes in fluorescence emission in the presence of substrate can be used to calculate dissociation constants, however this technique was not suitable in the case of the ARR enzyme.

To investigate binding of rifampin and NAD^+ to ARR, ^{15}N-^1H NMR experiments were employed. NMR data showed that both rifampin and NAD^+ were able to bind ARR in the absence of one another, and that upon binding a change in the conformation of ARR was

observed that was unique to each substrate interaction. These results also illustrated the flexibility of ARR, and the role of rifampin and NAD^+ in stabilization of the structure. Addition of rifampin and the dipeptide additive glycylglycine (bound to ARRm in the predicted NAD^+ binding site) to ARRm for crystallization improved crystal size and quality, supporting NMR data that suggests the substrates stabilize the structure of the enzyme.

ITC experiments were used to further characterize the binding interactions between ARR and rifampin and NAD^+. Results confirmed that while rifampin could easily bind to the ARR enzyme with high affinity (K_d values of 2.83 μM and 0.48 μM for ARRm and ARR-2 respectively), binding interactions with NAD^+ were unable to produce a K_d value. Dissociation constants for rifampin showed a greater affinity of ARR for the drug than K_m values calculated in the steady state. Dissociation constants measured for rifampin by ITC are specific to the interaction between free ARR and rifampin in the absence of NAD^+. Assuming that inactivation of rifampin by ARR occurs by an ordered Bi Bi reaction mechanism in which NAD^+ likely binds first, Km is measuring the formation of the rifampin-NAD^+-ARR complex, independent from measurements for the interaction of rifampin and ARR made by ITC. To confirm this, the steady state kinetic mechanism must be determined.

Based on the ARRm structure and ligand binding studies, it appears that ARR enzymes may exhibit a preferred order of substrate binding in which NAD^+ binds first followed by rifampin which occupies a binding pocket positioned over the NAD^+ binding cleft. While the structure of ARRm in complex with rifampin suggests NAD^+ binding occurs first, steady state kinetics or equilibrium dialysis must be used to confirm order of substrate binding and reaction mechanism. The structure of ARRm in addition to data from ligand binding studies allows for detailed investigation into the binding of rifampin and NAD^+ to ARR and the mechanism by which these

enzymes inactivate rifampin. Comparison of ARRm with the structure of ETA domain III in complex with β-TAD, and a variety of ADP-ribosyl transferase enzymes with a conserved NAD^+ binding fold allowed for the prediction of the NAD^+ binding site of ARRm. The position of the NAD^+ and rifampin binding sites confirm predictions made based ligand binding studies.

Comparison of ARRm with known ADP-ribosyl transferase enzymes of other classes allowed for the determination of residues likely to be involved in NAD^+ binding and catalysis, including His19, Tyr49, and Asp84. Site directed mutagenesis of these residues resulted in a loss of ADP-ribosyl transferase activity. Based on the structure of ARRm and results of site-directed mutagenesis studies it can be predicted that the ARR enzyme catalyzes the transfer of the ADP-ribose of NAD^+ to the 23-OH position of rifampin by an S_N1-type reaction (Figure 4-1). In this predicted mechanism the nicotinamide ring dissociates from NAD^+ forming a carbocation intermediate, stabilized by hydrogen bond interactions between the negative charged carboxylate of Asp84 to the nicotinamide ribose of NAD^+. The highly nucleophilic 23-OH of rifampin can then attack the carbocation intermediate, transferring the ADP-ribose to rifampin.

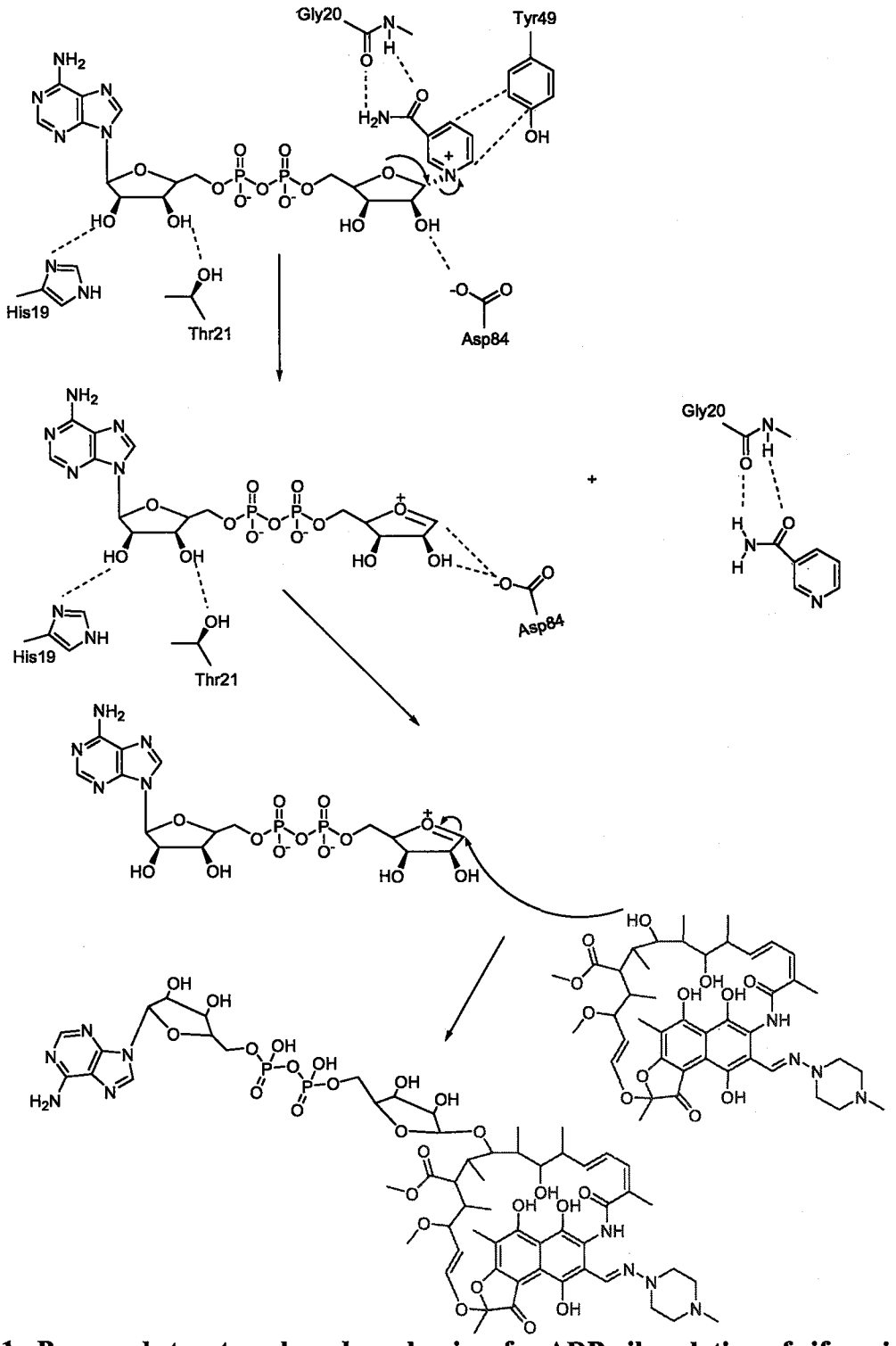

Figure 4-1. Proposed structure-based mechanism for ADP-ribosylation of rifampin. The schematic drawing for the mechanism shows the proposed S_N1 mechanism and the expected roles of Asp84, Gly20, and Thr21; NAD^+ cleavage via S_N1-type reaction, stabilization of the carbocation intermediate, and ADP-ribosyl group transfer. Tyr49 is believed to provide stacking interactions with the nicotinamide ring of NAD^+. Stereochemistry for the reaction product is predicted based on the crystal structure.

Rifampin ADP-ribosyl transferase enzymes exhibit indistinguishable substrate specific steady state kinetic parameters and substrate induced conformational changes whether chromosomally or Tn-encoded. Data from CD, NMR, and ITC in combination with the three-dimensional structure of ARRm in complex with rifampin have allowed for a detailed characterization of this unique class of ADP-ribosyl transferase enzyme. This information can be used in attempts to design potential inhibitors of ARR to aid in the continuing fight against antibiotic resistance.

4.2 References

1. Levy, S.B., and Marshall, B. (2004). Antibacterial resistance worldwide: causes, challenges and responses. *Nat Med 10*, S122-129.
2. Andries, K., Verhasselt, P., Guillemont, J., Gohlmann, H.W., Neefs, J.M., Winkler, H., Van Gestel, J., Timmerman, P., Zhu, M., Lee, E., Williams, P., de Chaffoy, D., Huitric, E., Hoffner, S., Cambau, E., Truffot-Pernot, C., Lounis, N., and Jarlier, V. (2005). A diarylquinoline drug active on the ATP synthase of Mycobacterium tuberculosis. *Science 307*, 223-227.
3. Tribuddharat, C., and Fennewald, M. (1999). Integron-mediated rifampin resistance in Pseudomonas aeruginosa. *Antimicrob Agents Chemother 43*, 960-962.
4. Houang, E.T., Chu, Y.W., Lo, W.S., Chu, K.Y., and Cheng, A.F. (2003). Epidemiology of rifampin ADP-ribosyltransferase (arr-2) and metallo-beta-lactamase (blaIMP-4) gene cassettes in class 1 integrons in Acinetobacter strains isolated from blood cultures in 1997 to 2000. *Antimicrob Agents Chemother 47*, 1382-1390.
5. Girlich, D., Naas, T., Leelaporn, A., Poirel, L., Fennewald, M., and Nordmann, P. (2002). Nosocomial spread of the integron-located veb-1-like cassette encoding an extended-pectrum beta-lactamase in Pseudomonas aeruginosa in Thailand. *Clin Infect Dis 34*, 603-611.
6. D'Costa, V.M., McGrann, K.M., Hughes, D.W., and Wright, G.D. (2006). Sampling the antibiotic resistome. *Science 311*, 374-377.
7. Floss, H.G., and Yu, T.W. (2005). Rifamycin-mode of action, resistance, and biosynthesis. *Chem Rev 105*, 621-632.
8. Lancini, G.a.C., B. (1997). Rifamycins. In Biotechnology of Antibiotics second edition, Volume 82, 2 Edition, W.R. Strohl, ed. (New York: Marcel Dekker, inc), pp. 521-549.
9. Parenti, F.a.L., G. (2003). Rifamycins. In Antibiotic and Chemotherapy Anti-infective agents and their use in therapy, 8 Edition, R.G. Finch, Greenwood, D., Norrby, S.R., and Whitely, R.J., ed. (New York: Churchill Livingstone), pp. 374-381.
10. Chaisson, R.E. (2003). Treatment of chronic infections with rifamycins: is resistance likely to follow? *Antimicrob Agents Chemother 47*, 3037-3039.
11. Padayachee, T., and Klugman, K.P. (1999). Molecular basis of rifampin resistance in Streptococcus pneumoniae. *Antimicrob Agents Chemother 43*, 2361-2365.
12. Oppolzer, W., Prelog, V., and Sensi, P. (1964). [The composition of rifamycin B and related rifamycins]. *Experientia 20*, 336-339.
13. Murphy, C.K., Mullin, S., Osburne, M.S., van Duzer, J., Siedlecki, J., Yu, X., Kerstein, K., Cynamon, M., and Rothstein, D.M. (2006). In vitro activity of novel rifamycins against rifamycin-resistant Staphylococcus aureus. *Antimicrob Agents Chemother 50*, 827-834.
14. Honore, N., and Cole, S.T. (1993). Molecular basis of rifampin resistance in Mycobacterium leprae. *Antimicrob Agents Chemother 37*, 414-418.
15. Quan, S., Venter, H., and Dabbs, E.R. (1997). Ribosylative inactivation of rifampin by Mycobacterium smegmatis is a principal contributor to its low susceptibility to this antibiotic. *Antimicrob Agents Chemother 41*, 2456-2460.
16. Gillespie, S.H. (2002). Evolution of drug resistance in Mycobacterium tuberculosis: clinical and molecular perspective. *Antimicrob Agents Chemother 46*, 267-274.

17. Duncan, K., and Barry, C.E., 3rd (2004). Prospects for new antitubercular drugs. *Curr Opin Microbiol 7*, 460-465.
18. Luna-Herrera, J., Reddy, M.V., and Gangadharam, P.R. (1995). In vitro activity of the benzoxazinorifamycin KRM-1648 against drug-susceptible and multidrug-resistant tubercle bacilli. *Antimicrob Agents Chemother 39*, 440-444.
19. Dickinson, J.M., and Mitchison, D.A. (1987). In vitro activity of new rifamycins against rifampicin-resistant M. tuberculosis and MAIS-complex mycobacteria. *Tubercle 68*, 177-182.
20. Moghazeh, S.L., Pan, X., Arain, T., Stover, C.K., Musser, J.M., and Kreiswirth, B.N. (1996). Comparative antimycobacterial activities of rifampin, rifapentine, and KRM-1648 against a collection of rifampin-resistant Mycobacterium tuberculosis isolates with known rpoB mutations. *Antimicrob Agents Chemother 40*, 2655-2657.
21. Suchland, R.J., Bourillon, A., Denamur, E., Stamm, W.E., and Rothstein, D.M. (2005). Rifampin-resistant RNA polymerase mutants of Chlamydia trachomatis remain susceptible to the ansamycin rifalazil. *Antimicrob Agents Chemother 49*, 1120-1126.
22. Kutlin, A., Kohlhoff, S., Roblin, P., Hammerschlag, M.R., and Riska, P. (2005). Emergence of resistance to rifampin and rifalazil in Chlamydophila pneumoniae and Chlamydia trachomatis. *Antimicrob Agents Chemother 49*, 903-907.
23. Roblin, P.M., Reznik, T., Kutlin, A., and Hammerschlag, M.R. (2003). In vitro activities of rifamycin derivatives ABI-1648 (Rifalazil, KRM-1648), ABI-1657, and ABI-1131 against Chlamydia trachomatis and recent clinical isolates of Chlamydia pneumoniae. *Antimicrob Agents Chemother 47*, 1135-1136.
24. Akada, J.K., Shirai, M., Fujii, K., Okita, K., and Nakazawa, T. (1999). In vitro anti-Helicobacter pylori activities of new rifamycin derivatives, KRM-1648 and KRM-1657. *Antimicrob Agents Chemother 43*, 1072-1076.
25. Rothstein, D.M., Farquhar, R.S., Sirokman, K., Sondergaard, K.L., Hazlett, C., Doye, A.A., Gwathmey, J.K., Mullin, S., van Duzer, J., and Murphy, C.K. (2006). Efficacy of Novel Rifamycin Derivatives against Rifamycin-Sensitive and -Resistant Staphylococcus aureus Isolates in Murine Models of Infection. *Antimicrob Agents Chemother 50*, 3658-3664.
26. Pakyz, A.L. (2005). Rifaximin: a new treatment for travelers' diarrhea. *Ann Pharmacother 39*, 284-289.
27. McClure, W.R., and Cech, C.L. (1978). On the mechanism of rifampicin inhibition of RNA synthesis. *J Biol Chem 253*, 8949-8956.
28. Campbell, E.A., Korzheva, N., Mustaev, A., Murakami, K., Nair, S., Goldfarb, A., and Darst, S.A. (2001). Structural mechanism for rifampicin inhibition of bacterial rna polymerase. *Cell 104*, 901-912.
29. Naryshkina, T., Mustaev, A., Darst, S.A., and Severinov, K. (2001). The beta ' subunit of Escherichia coli RNA polymerase is not required for interaction with initiating nucleotide but is necessary for interaction with rifampicin. *J Biol Chem 276*, 13308-13313.
30. Zhang, G., Campbell, E.A., Minakhin, L., Richter, C., Severinov, K., and Darst, S.A. (1999). Crystal structure of Thermus aquaticus core RNA polymerase at 3.3 A resolution. *Cell 98*, 811-824.
31. Schulz, W., and Zillig, W. (1981). Rifampicin inhibition of RNA synthesis by destabilisation of DNA-RNA polymerase-oligonucleotide-complexes. *Nucleic Acids Res 9*, 6889-6906.

32. Mustaev, A., Zaychikov, E., Severinov, K., Kashlev, M., Polyakov, A., Nikiforov, V., and Goldfarb, A. (1994). Topology of the RNA polymerase active center probed by chimeric rifampicin-nucleotide compounds. *Proc Natl Acad Sci U S A 91*, 12036-12040.
33. Artsimovitch, I., Vassylyeva, M.N., Svetlov, D., Svetlov, V., Perederina, A., Igarashi, N., Matsugaki, N., Wakatsuki, S., Tahirov, T.H., and Vassylyev, D.G. (2005). Allosteric modulation of the RNA polymerase catalytic reaction is an essential component of transcription control by rifamycins. *Cell 122*, 351-363.
34. Hetherington, S.V., Watson, A.S., and Patrick, C.C. (1995). Sequence and analysis of the rpoB gene of Mycobacterium smegmatis. *Antimicrob Agents Chemother 39*, 2164-2166.
35. Andersen, S.J., Quan, S., Gowan, B., and Dabbs, E.R. (1997). Monooxygenase-like sequence of a Rhodococcus equi gene conferring increased resistance to rifampin by inactivating this antibiotic. *Antimicrob Agents Chemother 41*, 218-221.
36. Dabbs, E.R., Yazawa, K., Tanaka, Y., Mikami, Y., Miyaji, M., Andersen, S.J., Morisaki, N., Iwasaki, S., Shida, O., Takagi, H., and et al. (1995). Rifampicin inactivation by Bacillus species. *J Antibiot (Tokyo) 48*, 815-819.
37. Morisaki, N., Iwasaki, S., Yazawa, K., Mikami, Y., and Maeda, A. (1993). Inactivated products of rifampicin by pathogenic Nocardia spp.: structures of glycosylated and phosphorylated metabolites of rifampicin and 3-formylrifamycin SV. *J Antibiot (Tokyo) 46*, 1605-1610.
38. Quan, S., Imai, T., Mikami, Y., Yazawa, K., Dabbs, E.R., Morisaki, N., Iwasaki, S., Hashimoto, Y., and Furihata, K. (1999). ADP-ribosylation as an intermediate step in inactivation of rifampin by a mycobacterial gene. *Antimicrob Agents Chemother 43*, 181-184.
39. Tanaka, Y., Yazawa, K., Dabbs, E.R., Nishikawa, K., Komaki, H., Mikami, Y., Miyaji, M., Morisaki, N., and Iwasaki, S. (1996). Different rifampicin inactivation mechanisms in Nocardia and related taxa. *Microbiol Immunol 40*, 1-4.
40. Yazawa, K., Mikami, Y., Maeda, A., Akao, M., Morisaki, N., and Iwasaki, S. (1993). Inactivation of rifampin by Nocardia brasiliensis. *Antimicrob Agents Chemother 37*, 1313-1317.
41. Yazawa, K., Mikami, Y., Maeda, A., Morisaki, N., and Iwasaki, S. (1994). Phosphorylative inactivation of rifampicin by Nocardia otitidiscaviarum. *J Antimicrob Chemother 33*, 1127-1135.
42. Jin, D.J., and Gross, C.A. (1988). Mapping and sequencing of mutations in the Escherichia coli rpoB gene that lead to rifampicin resistance. *J Mol Biol 202*, 45-58.
43. Severinov, K., Mustaev, A., Severinova, E., Kozlov, M., Darst, S.A., and Goldfarb, A. (1995). The beta subunit Rif-cluster I is only angstroms away from the active center of Escherichia coli RNA polymerase. *J Biol Chem 270*, 29428-29432.
44. Ohno, H., Koga, H., Kohno, S., Tashiro, T., and Hara, K. (1996). Relationship between rifampin MICs for and rpoB mutations of Mycobacterium tuberculosis strains isolated in Japan. *Antimicrob Agents Chemother 40*, 1053-1056.
45. Dabbs, E.R., Yazawa, K., Mikami, Y., Miyaji, M., Morisaki, N., Iwasaki, S., and Furihata, K. (1995). Ribosylation by mycobacterial strains as a new mechanism of rifampin inactivation. *Antimicrob Agents Chemother 39*, 1007-1009.
46. Wright, G.D. (2005). Bacterial resistance to antibiotics: enzymatic degradation and modification. *Adv Drug Deliv Rev 57*, 1451-1470.
47. Ueda, K., and Hayaishi, O. (1985). ADP-ribosylation. *Annu Rev Biochem 54*, 73-100.

48. Corda, D., and Di Girolamo, M. (2003). Functional aspects of protein mono-ADP-ribosylation. *Embo J 22*, 1953-1958.
49. Ame, J.C., Spenlehauer, C., and de Murcia, G. (2004). The PARP superfamily. *Bioessays 26*, 882-893.
50. Yates, S.P., Jorgensen, R., Andersen, G.R., and Merrill, A.R. (2006). Stealth and mimicry by deadly bacterial toxins. *Trends Biochem Sci 31*, 123-133.
51. Krueger, K.M., and Barbieri, J.T. (1995). The family of bacterial ADP-ribosylating exotoxins. *Clin Microbiol Rev 8*, 34-47.
52. Smith, S. (2001). The world according to PARP. *Trends Biochem Sci 26*, 174-179.
53. Leatherbarrow, R.J. (2000). Grafit, Erithacus Software: Staines, U.K.
54. Delaglio, F., Torchia, D.A., and Bax, A. (1991). Measurement of 15N-13C J couplings in staphylococcal nuclease. *J Biomol NMR 1*, 439-446.
55. Parikh, S.L., and Schramm, V.L. (2004). Transition state structure for ADP-ribosylation of eukaryotic elongation factor 2 catalyzed by diphtheria toxin. *Biochemistry 43*, 1204-1212.
56. Armstrong, S., and Merrill, A.R. (2004). Toward the elucidation of the catalytic mechanism of the mono-ADP-ribosyltransferase activity of Pseudomonas aeruginosa exotoxin A. *Biochemistry 43*, 183-194.
57. McPherson, A., Malkin, A.J., and Kuznetsov, Y.G. (1995). The science of macromolecular crystallization. *Structure 3*, 759-768.
58. Blow, D.M., Chayen, N.E., Lloyd, L.F., and Saridakis, E. (1994). Control of nucleation of protein crystals. *Protein Sci 3*, 1638-1643.
59. Ruf, A., Rolli, V., de Murcia, G., and Schulz, G.E. (1998). The mechanism of the elongation and branching reaction of poly(ADP-ribose) polymerase as derived from crystal structures and mutagenesis. *J Mol Biol 278*, 57-65.
60. Li, M., Dyda, F., Benhar, I., Pastan, I., and Davies, D.R. (1995). The crystal structure of Pseudomonas aeruginosa exotoxin domain III with nicotinamide and AMP: conformational differences with the intact exotoxin. *Proc Natl Acad Sci U S A 92*, 9308-9312.
61. Bell, C.E., and Eisenberg, D. (1996). Crystal structure of diphtheria toxin bound to nicotinamide adenine dinucleotide. *Biochemistry 35*, 1137-1149.
62. Tsuge, H., Nagahama, M., Nishimura, H., Hisatsune, J., Sakaguchi, Y., Itogawa, Y., Katunuma, N., and Sakurai, J. (2003). Crystal structure and site-directed mutagenesis of enzymatic components from Clostridium perfringens iota-toxin. *J Mol Biol 325*, 471-483.
63. Han, S., Arvai, A.S., Clancy, S.B., and Tainer, J.A. (2001). Crystal structure and novel recognition motif of rho ADP-ribosylating C3 exoenzyme from Clostridium botulinum: structural insights for recognition specificity and catalysis. *J Mol Biol 305*, 95-107.
64. Li, M., Dyda, F., Benhar, I., Pastan, I., and Davies, D.R. (1996). Crystal structure of the catalytic domain of Pseudomonas exotoxin A complexed with a nicotinamide adenine dinucleotide analog: implications for the activation process and for ADP ribosylation. *Proc Natl Acad Sci U S A 93*, 6902-6906.
65. Allured, V.S., Collier, R.J., Carroll, S.F., and McKay, D.B. (1986). Structure of exotoxin A of Pseudomonas aeruginosa at 3.0-Angstrom resolution. *Proc Natl Acad Sci U S A 83*, 1320-1324.
66. Han, X.Y., and Galloway, D.R. (1995). Active site mutations of Pseudomonas aeruginosa exotoxin A. Analysis of the His440 residue. *J Biol Chem 270*, 679-684.

67. Lukac, M., and Collier, R.J. (1988). Pseudomonas aeruginosa exotoxin A: effects of mutating tyrosine-470 and tyrosine-481 to phenylalanine. *Biochemistry 27*, 7629-7632.
68. Marsischky, G.T., Wilson, B.A., and Collier, R.J. (1995). Role of glutamic acid 988 of human poly-ADP-ribose polymerase in polymer formation. Evidence for active site similarities to the ADP-ribosylating toxins. *J Biol Chem 270*, 3247-3254.